Jets in Photoproduction at HERA

Von der Fakultät für Mathematik, Informatik und Naturwissenschaften
der Rheinisch-Westfälischen Technischen Hochschule Aachen
zur Erlangung des akademischen Grades eines Doktors
der Naturwissenschaften genehmigte Dissertation

vorgelegt von

Diplom-Physiker
Sascha Caron

aus Heinsberg

Berichter: Universitätsprofessor Dr. Ch. Berger
Universitätsprofessor Dr. G. Flügge

Tag der mündlichen Prüfung: 11.7.2002

Abstract

Dijet and three-jet cross sections as functions of various jet observables are measured in photoproduction using the H1 detector at HERA. The data sample comprises e^+p data collected from 1995-97 with an integrated luminosity of 34.9 pb^{-1}. Jets are found using the inclusive $k_\perp$ algorithm with a minimum transverse momentum of the highest transverse momentum jet of 25 GeV. The phase space covers high longitudinal proton momentum fractions $0.05 < x_P < 0.6$ and high photon longitudinal momentum fractions $0.1 < x_\gamma < 1$. The results are compared to the predictions of leading order and next-to-leading order perturbative QCD including current photon and proton parton densities. The dijet cross sections are found to be compatible in a wide kinematical range. At low x_γ the 3-jet cross sections show deviations from the predictions of leading-order QCD.

Zusammenfassung

In dieser Arbeit wurden Zwei- und Drei-Jet Wirkungsquerschnitte als Funktion verschiedenster Jet-Observablen gemessen. Die Daten wurden zwischen 1995 und 1997 genommen und entsprechen einer integrierten Luminosität von 34.9 pb^{-1}. Jets sind mittels des inklusiven $k_\perp$ Algorithmus definiert und es ist ein Transversalimpuls von mindestens 25 GeV gefordert. Der Phasenraum beinhaltet longitudinale Proton Impulsanteile $0.05 < x_P < 0.6$ und longitudinale Photon Impulsanteile $0.1 < x_\gamma < 1$. Die Daten sind mit den Vorhersagen der führenden und nächst-zu-führenden Ordnung pertubativer QCD verglichen und in einem weiten kinematischen Bereich wurde eine Übereinstimmung gefunden. Die Drei-Jet Wirkungsquerschnitte zeigen bei kleinem x_γ Abweichungen von den Vorhersagen der führenden Ordnung pertubativer QCD.

Contents

1
Introduction

The Standard Model of particle physics contains the strong force and describes it with a theory known as Quantum Chromo Dynamics (QCD). QCD successfully predicts a wide range of measurements. At high energies (or scales) the QCD calculations are performed by expanding predictions in powers of the strong coupling constant. The use of perturbation theory is based on asymptotic freedom, the feature that the strong coupling constant vanishes at large energies.
In this work an analysis of jet photoproduction up to the highest possible transverse energies is presented[1]. Cross sections of various dijet and three-jet observables are determined and compared to perturbative QCD calculations.
In QCD the photoproduction of jets with high transverse energy is described by the hard interaction of real photons with quarks and gluons inside the proton. These interactions are due to direct processes, in which the photon scatters directly off a parton in the proton and resolved processes where the photon first splits into partons and one of the resulting partons subsequently scatters off a parton in the proton. The calculation of the latter processes can be approximated by ascribing parton densities to the photon, which also include the inherently non-perturbative aspects of the photon structure.
At the electron-proton collider HERA these photoproduction reactions can be investigated in inelastic electron (positron) proton reactions at very small squared four-momentum transfers Q^2. Starting from the first investigation of this kind at HERA [6] the comparison of the predictions of QCD with the results has been a central topic of interest [7, 8, 9]. These investigations are particularly interesting, because previous measurements of high transverse energy jet production in ep and $p\bar{p}$ scattering were not fully described by QCD calculations [10, 11, 12, 13]. Exemplary dijet cross sections in photoproduction were found to be hardly compatible with QCD calculations in phase space regions dominated by resolved events.

[1]Preliminary results of this analysis have been reported in [1, 2, 3]. The final dijet cross sections are published in [4]. A similar analysis has recently been made available in [5].

High transverse energy jets provide a natural hard scale for perturbative QCD calculations. Such calculations have been performed for direct and resolved dijet processes in leading (LO) and next-to-leading (NLO) order and three-jet processes in leading order.
The measurement of dijet cross sections at high transverse energy can therefore be used to test the current predictions of NLO perturbative QCD and the parameterizations of photon and proton parton densities at large scales with a high precision.
Photon quark densities have been determined in experiments at e^+e^--colliders[37] which investigate the photon structure function F_2^γ, where x_γ between 0.01 and $0.8-1$ and scales between 0.2 to 780 GeV^2 have been reached [38]. In comparison the analysis presented here extends the x_γ range up to 1 at scales between 600 and 6000 GeV^2, where the quark density parameterizations of the photon are presently not well constrained by measurements. In contrast to the F_2^γ measurements, the photoproduction of jets is directly sensitive to the gluon density of the photon, which is poorly known to date. It is therefore one goal of the analysis presented in this work to test the photon structure at high x_γ values and high scales.
Furthermore our data are sensitive to the parton densities of the proton at fractional momentum values x_p up to 0.6. In this kinematical regime, the quark densities are well known from deeply inelastic scattering data, while the gluon density has uncertainties of the order 10 to 50%[40]. Photoproduction data can thus be used to constrain the parton density functions in regions where only few measurements are presently available. However, detailed parton densities can not be extracted from these data alone.
Final states containing three jets provide an additional testing ground of perturbative QCD. These events are also important as a possible background to various new physics signals. The measurement of three-jet cross sections can be used to test LO perturbative QCD. Similar studies of three-jet (or four-jet) final states can be found in [14, 15, 16, 17, 18, 19, 20].
This work is outlined as follows. In chapter 2 the theoretical foundations of the photoproduction of jets and the perturbative QCD calculations are discussed. Chapter 3 contains a short description of HERA and the H1 experiment, the event selection, the reconstruction and the measurement procedure of jet cross sections. The final cross sections are presented in chapter 4. A summary and outlook is finally given in chapter 5. In the appendix data tables for dijet cross sections and hadronization effects are presented. Furthermore the sensitivity on the particular choice of the jet cuts and a check of the Monte Carlo description of the jet resolution are discussed.

2

Photoproduction of Jets at HERA

The chapter starts with a discussion of basic theoretical ideas of electron-proton scattering and the photoproduction of jets. Emphasis is placed on the proton structure, the photon structure and fixed order perturbative QCD calculations. Almost all arguments are taken from textbooks, e.g. [28, 29, 30, 31, 32].

2.1 Foundations of Photon-Proton scattering

2.1.1 Basics of Electron-Proton scattering

The scattering of electrons[1] and protons occur in lowest order perturbation theory either by the exchange of a photon (γ), Z^0 or W boson. Photon or Z^0 exchange are *neutral currents* (NC), whereas the exchange of a W boson refers to *charged current* (CC).

A diagram of the process $ep \to eX$ is displayed in Figure 2.1. An incoming electron with the 4-momentum k scatters off a proton with 4-momentum P. The 4-momentum of the outgoing lepton (electron for NC, neutrino for CC interactions) is k'.

The abbreviation X stands for a not specified system of the reaction products. The squared centre-of-mass energy of the reaction is

$$s = (P + k)^2 \ . \tag{2.1}$$

The negative squared 4-momentum transfer Q^2 of the electron to the proton is given by

$$Q^2 = -q^2 = -(k - k')^2 \ . \tag{2.2}$$

If Q^2 is not vanishing and the invariant mass of the system X is much larger than the proton mass the scattering process is called deep-inelastic scattering (DIS).

[1] The term electron refers in the following to the electron and the positron. All following arguments hold for both particles.

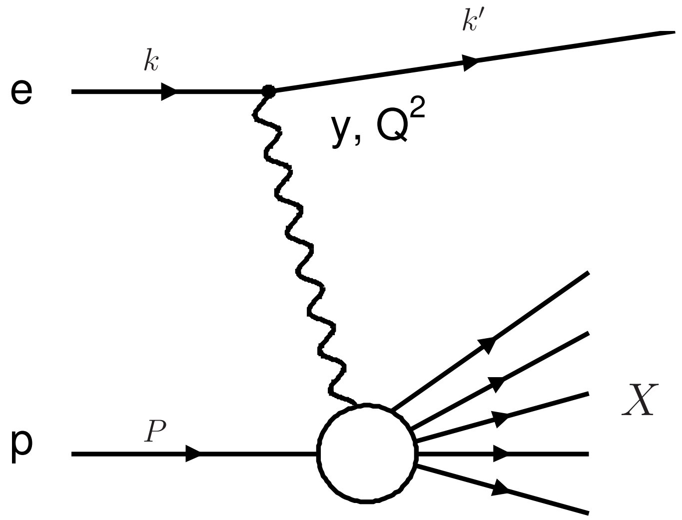

Figure 2.1: *Electron-Proton scattering.*

To describe the kinematics of the reaction $eP \rightarrow eX$ in DIS for a fixed centre-of-mass energy $\sqrt{s}$ only two variables are needed. One possible choice is Q^2 and the Bjorken scaling variable x_{BJ}, another choice is Q^2 and the inelasticity y. The Bjorken scaling variable is given by

$$x_{Bj} = \frac{Q^2}{2P \cdot q} \tag{2.3}$$

and the inelasticity y is

$$y = \frac{P \cdot q}{P \cdot k} \; . \tag{2.4}$$

In the proton rest frame the variable y can be interpreted as the fraction of energy transfered from the electron to the proton. For a process describable by the diagram of Fig. 2.2 alone the Bjorken scaling variable x_{Bj} is the fraction of the longitudinal 4-momentum of the proton (in the infinite momentum frame) which participates in the hard scattering.
In the infinite momentum frame ($P \rightarrow \infty$) the parton model envisages the proton as being made of partons i (the constituents of the proton) which carry only a fraction $\xi_{p,i}$ of the longitudinal proton momentum (such that $\Sigma_i \xi_{p,i} = 1$)[33]. It interprets the scattering of hadrons as a superposition of the scattering of partons.
Individual partons in the proton are , due to the increasing strong force with increasing distances, not directly observable. Therefore the way the parton content of the proton is described are universal probabilistic parton densities. The partons in the

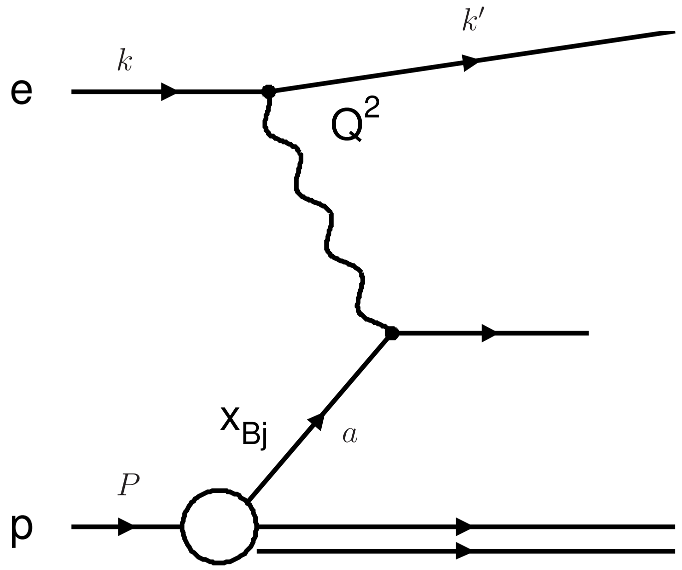

Figure 2.2: *Electron-Proton scattering in lowest order perturbation theory $O(\alpha\alpha_s^0)$ using the parton model.*

proton have been identified as quarks and gluons. So the parton density functions (pdfs), one for each quark flavour and one for the gluon, give in the parton model the number density of finding a parton i with a momentum fraction ξ_p. This longitudinal momentum fraction ξ_p of the proton taken by the interacting parton with 4-momentum a out of the proton is

$$\xi_p = \frac{q \cdot a}{q \cdot P} \ . \tag{2.5}$$

2.1.2 The Photon Flux

For small Q^2 values the electron-proton scattering can be simplified by the radiation of a photon from the electron and the subsequent scattering of the photon with the proton. This kinematic domain of electron-proton scattering is usually referred to as photoproduction, i.e. the production of hadrons by the inelastic scattering of real photons on a nucleon target.

Most cross sections in electron proton collisions are dominated by photoproduction, where the electron radiates quasi-real ($Q^2 < 1$ GeV^2) photons with energy fractions y according to the Weizsäcker-Williams approximation. Here the usual variable y of deep inelastic scattering is interpreted as the longitudinal momentum fraction of the incoming electron taken by the photon. It is directly related to the photon-proton

centre-of-mass energy $W_{\gamma p} = \sqrt{sy}$. The proton and electron mass is here and in the following expressions neglected.
The hadronic[2] cross section for the photoproduction of jets in electron-proton collisions, σ_{ep}, can be calculated from the photon-proton scattering result, $\sigma_{\gamma p}$, using this factorization ansatz

$$\sigma_{ep\to eX} = \int \mathrm{d}y f_{\gamma,e}(y)\sigma_{\gamma p}(y) \ . \tag{2.6}$$

The photon flux, $f_{\gamma,e}$, out of the electron is calculated in the Weizsäcker-Williams approximation[41, 42, 43] and can be written as:

$$f_{\gamma,e}(y) = \frac{\alpha}{2\pi}\left(\frac{1+(1-y)^2}{y}\log\frac{Q^2_{\mathrm{max}}(1-y)}{m_e^2 y^2} + 2m_e^2 y(\frac{1}{Q^2_{\mathrm{max}}} - \frac{1-y}{m_e^2 y^2})\right) \tag{2.7}$$

The result that the electron-proton cross section can be simplified by a convolution of the photon flux and the cross section for the scattering of a real ($Q^2 = 0$ GeV^2) photon with a proton has been derived using current conservation and the condition that Q^2 is very small. The boundary conditions for the integral are the experimental kinematic cuts.
The maximum photon virtuality Q^2_{max} is given by the experimental conditions and is via

$$Q^2 = -(k-k')^2 = 2E_e E_{el}(1+\cos\theta_e) \tag{2.8}$$

related to the (maximum) energy E_{el} and angle θ_e of the scattered electron. Here the energy of the incoming electron beam is E_e.

2.1.3 Photoproduction in the Parton Model

A fundament of QCD is the use of factorization, the theorem that a cross section can be written as convolution of different factors. Completely calculable short distance parts of the cross section are separated from partly non-calculable long distance parts. Factorization is fundamental for the calculation of the cross sections measured in this work.
Figure 2.3 illustrates electron proton scattering in the photoproduction regime producing jets. The photoproduction of jets with high transverse energy is in QCD described by the hard interaction of real photons with the partons inside the proton. Of interest are the processes with at least two final state partons with large transverse momenta.

[2] The term *hadronic* cross section refers to the scattering with hadrons (e.g. eP or γP scattering), whereas the *partonic* cross section refers to the scattering with partons.

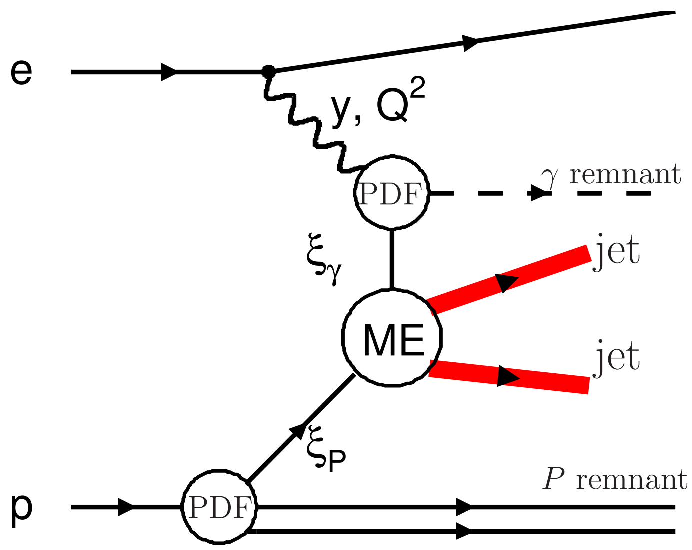

Figure 2.3: *Schematic diagram for the production of jets in electron-proton scattering.*

Two interaction classes have to be considered. If the real photon couples as a pointlike particle with a parton of the proton, then it is called *direct* interaction. But, the photon may fluctuate into an unbound quark pair (*anomalous*) or into a vector meson which carries the quantum numbers of the photon (*Vector-Meson-Dominance*) and it then interacts like a hadron with the proton. These are termed *resolved* photon-proton interactions.

Interactions with two outgoing partons of large transverse momentum are due to direct processes, such as $\gamma q \rightarrow gq$ (QCD-Compton scattering) and $\gamma g \rightarrow q\overline{q}$ (photon-gluon fusion) and due to resolved processes where the photon first splits into a quark pair (or higher multiplicity fluctuation) and one of the resulting partons subsequently scatters off a parton in the proton. The calculation of the latter processes can be approximated by ascribing parton densities to the photon depending on the longitudinal momentum fraction of the photon taken by the interacting parton with 4-momentum b out of the photon

$$\xi_\gamma = \frac{P \cdot b}{P \cdot q} \; . \tag{2.9}$$

In summary the photoproduction of jets in electron-proton scattering is derived using a factorization into photon-proton scattering, ascribing parton momentum distributions to the proton (and photon) and calculating — in the direct case — $\hat{\sigma}_{i,\gamma}$, the scattering of a real photon on a parton i and — in the resolved case — $\hat{\sigma}_{i,j}$ the scattering of a parton i with a parton j.

2.1.4 Renormalization and Factorization

The Strong Coupling Constant

Exemplary for a QCD scattering process the scattering of two quarks is not only defined by the one gluon exchange diagram, but also by diagrams including quark and gluon loops. The latter diagrams are divergent for infinite momentum of the particles in the loop. These ultraviolet (UV) divergencies are absorbed into a redefinition of the strong coupling constant α_s. The energy scale at which the subtraction of the divergent terms into α_s is performed is μ_r. Then, however, is α_s a function of the renormalization scale μ_r.
The renormalization scale dependence of $\alpha_s = g^2/4\pi$ is given by the renormalization group equation

$$\mu_r \frac{\mathrm{d}g(\mu_r)}{\mathrm{d}\mu_r} = \beta(g(\mu_r)) \tag{2.10}$$

and the beta function β is an expansion in α_s:

$$\beta(g) = -g\left((\frac{\alpha_s}{4\pi})^1 \beta_1 + (\frac{\alpha_s}{4\pi})^2 \beta_2 + \ldots \right) \quad . \tag{2.11}$$

The coefficients β_i can be calculated using loop diagrams, e.g. $\beta_1 = (11N_c - 2n_f)/3$, where n_f is the number of flavours and N_c is the number of colours, i.e. 3 for QCD. The scale dependence of α_s is known as the running coupling.
The solution of eq. 2.10 up to the leading term β_1 leads to the 1-loop expression of α_s

$$\alpha_s(\mu_r) = \frac{4\pi}{\beta_1 \ln(\frac{\mu_r^2}{\Lambda^2})} \quad . \tag{2.12}$$

Unfortunately QCD does not predict the absolute value of α_s at a given scale. This has to be derived from experimental data. Usually α_s is given at the scale $\mu_r = M_Z$. Instead of $\alpha_s(M_Z)$ a dimensional parameter Λ is often used, which specifies the scale μ_r at which $\alpha_s(\mu_r)$ diverges (in eq.2.12).The value of the Λ parameter depends on the number of active flavours.
Asymptotic freedom, the observation that in QCD the coupling constant is becoming smaller at high energies, explains why perturbative QCD is useful at high energies. At high energies a quantity like $\hat{\sigma}_{\gamma,i}$ or $\hat{\sigma}_{i,j}$ can be computed in perturbation theory as

$$\hat{\sigma}_{\gamma,i} = \sum_{n=a}^{\infty} \alpha_s^n(\mu_r, \Lambda) C_n(\mu_r) \quad . \tag{2.13}$$

For photoproduction dijet cross sections the leading power a is 1 and for 3-jet cross sections it is 2. The coefficient C_a does not depend on μ_r.

The coefficients C_n are calculated using Feynman diagrams of order α_s^n. Since μ_r defines when to calculate a piece of the cross section in α_s and when in the coefficients, also these depend on μ_r. In a not truncated expansion the choice of μ_r should be abritary.

When performing these calculation several divergencies arise. They have to be regulated in a well defined way, a specific *renormalisation scheme*. The scheme most often used is the *modified minimal subtraction* ($\overline{MS}$) scheme. In the $\overline{MS}$ scheme divergences are regulated by integrating not over 4 space-time dimensions, but over $4 - \epsilon$ dimensions, which leads to poles like $1/\epsilon$ and these poles may be subtracted. Then the coefficients explicitly depend on the used renormalisation scheme.

Parton Densities

Similar arguments hold for the introduction of the factorization scale μ_f. The short distance cross sections, e.g. $\hat{\sigma}_{\gamma,i}$, are derived by factoring long distance parts of the hadronic cross sections into new renormalized parton momentum densities. Divergencies from initial state gluon radiation (collinear singularities) are absorbed into a redefinition of the parton momentum densities into *renormalized* parton momentum densities. Again the factorization scale is an arbitrary parameter, which is the scale at which the short distance parts are separated from the long distance parts. For instance gluon radiation at large transverse momenta is calculated in the partonic cross section and gluon radiation at small transverse momenta is part of the parton densities.

The parton momentum densities $f_{a,b}(\xi, \mu_f)$ can be interpreted as the number density to find a parton a with the longitudinal energy fraction ξ in a particle b and taking into account collinear gluon emission up to $\mu_f < P_T$ where P_T is the transverse momentum of the radiated gluons.

The ξ dependence of the proton parton densities has to be measured by experiments at a certain interaction energy. Only the scale dependence can be calculated according to the DGLAP equations [34, 35, 36]. As already stated above the photon is a complicated object due to the possible fluctuations into partons. Contrary to the proton case also the ξ dependence of the photon can be partly calculated in QCD. The photon structure will be further discussed in section 2.4.

For both parton density functions ($f_{j/\gamma}$ and $f_{i/p}$) their factorization scale dependence is calculated using integro-differential matrix (DGLAP) equations. The DGLAP equations for the proton pdfs can be written as[3].

[3]Following the usual convention that neglects the denominator in the ln.

$$\frac{\mathrm{d}f_q(\xi,\mu_f)}{\mathrm{d}\ln\mu_f^2} = \frac{\alpha_s(\mu_f)}{2\pi}\int_\xi^1 \frac{\mathrm{d}z}{z}\left(P_{qg}(z)f_g(\frac{\xi}{z},\mu_f) + P_{qq}(z)f_q(\frac{\xi}{z},\mu_f)\right) \quad (2.14)$$

$$\frac{\mathrm{d}f_g(\xi,\mu_f)}{\mathrm{d}\ln\mu_f^2} = \frac{\alpha_s(\mu_f)}{2\pi}\int_\xi^1 \frac{\mathrm{d}z}{z}\left(P_{gg}(z)f_g(\frac{\xi}{z},\mu_f) + \sum_q P_{gq}(z)f_q(\frac{\xi}{z},\mu_f)\right) . \quad (2.15)$$

Here $P_{ij}(z)$ are probability densities to obtain a parton i from a parton j with a momentum fraction z from the momentum of parton j. These splitting functions P_{ij} are calculated as perturbative expansions in α_s (again in a certain factorization scheme, e.g. $\overline{MS}$). Here the gluon density of the proton is f_g, and the f_q are the quark densities.

2.1.5 Structure of the hadronic Cross Section in QCD

In perturbative QCD the hadronic photon-proton jet cross section is obtained using the factorization theorem as the convolution of the partonic cross sections with the renormalized parton momentum densities of the proton $f_{i/p}$ and the photon $f_{j/\gamma}$.
The hadronic cross section is usually divided into a sum of two components, the direct part $\sigma_{\gamma p}^{\mathrm{direct}}$ and the resolved part $\sigma_{\gamma p}^{\mathrm{resolved}}$. This distinction is unambiguously defined only in leading order and depends on a photon factorization scale μ_γ. The two components can be expressed as:

$$\sigma_{\gamma p}^{direct} = \sum_i \int d\xi_p f_{i/p}(\xi_p,\mu_p)\hat{\sigma}_{i\gamma}(\hat{s},\mu_\gamma,\mu_p,\alpha_s(\mu_r),\mu_r) \quad (2.16)$$

$$\sigma_{\gamma p}^{resolved} = \sum_{j,i} \int d\xi_\gamma f_{j/\gamma}(\xi_\gamma,\mu_\gamma) d\xi_p f_{i/p}(\xi_p,\mu_p)\hat{\sigma}_{ij}(\hat{s},\mu_\gamma,\mu_p,\alpha_s(\mu_r),\mu_r) . \quad (2.17)$$

The squared centre-of-mass energy of the hard subprocess is $\hat{s} = \xi_p\xi_\gamma ys$, where $\sqrt{s}$ is the total centre-of-mass energy in the *ep*-system, i.e. 300 GeV at HERA. The proton factorization scale is μ_p. The total cross sections on the left hand side of equation 2.6 are obtained by integrating over y, ξ_p and ξ_γ. The partonic cross sections $\hat{\sigma}_{i\gamma}$ and $\hat{\sigma}_{ij}$ contain a further integration over an internal degree of freedom, e.g. $\cos\theta^*$, the scattering angle in the centre-of-mass system of the partonic two body reaction, or the transverse energy.

2.1.6 Perturbative QCD

The partonic cross sections $\hat{\sigma}$ can be expanded as a perturbative series in powers of α_s as expressed in equation 2.13.

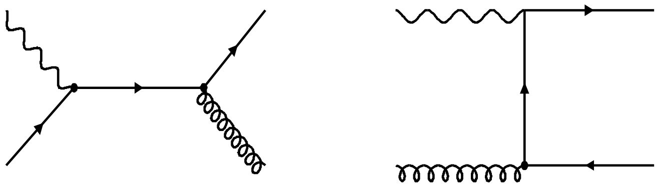

Figure 2.4: *Born diagrams for direct photoproduction (Final state QCD compton scattering and boson-gluon fusion diagram.)*

In leading order the direct photoproduction is of $\mathcal{O}(\alpha\alpha_s)$ and the resolved photoproduction is of $\mathcal{O}(\alpha\alpha_s^2)$. Often the argument is used that the resolved partonic cross section convoluted with the photon parton densities results in the same order for the direct and resolved parts of the hadronic cross section $\sigma_{\gamma P}$. The reason is that the photon pdfs look like $\mathcal{O}(1/\alpha_s)$.

The leading order (Born) cross sections of the direct photoproduction of two jets are QCD-Compton scattering $\gamma q \rightarrow gq$ and photon-gluon fusion $\gamma g \rightarrow q\overline{q}$, both displayed in Figure 2.4. Their matrix elements are connected by crossing relations.

Examples of leading order resolved diagrams are displayed in Fig. 2.5. Resolved parton subprocesses are e.g. $qq \rightarrow qq$, $q\overline{q} \rightarrow q\overline{q}$, $qg \rightarrow qg$, $q\overline{q} \rightarrow gg$, $gg \rightarrow q\overline{q}$ and $gg \rightarrow gg$.

Most of the matrix elements diverge for $\cos\theta^* \rightarrow 1$. In order to avoid mass singularities in the partonic cross sections a minimum cut in θ^* or in the transverse energy of the outgoing partons has to be applied. Note that the resolved matrix elements are predicted to rise steeper as a function of $\cos\theta^*$.

Next-to-leading order corrections to the partonic dijet cross section are due to direct processes of $\mathrm{O}(\alpha_s^2)$ and resolved processes of $\mathrm{O}(\alpha_s^3)$. These are virtual one loop ($2 \rightarrow 2$ processes) and real corrections ($2 \rightarrow 3$ processes). Examples are shown in Figure 2.6. The real corrections for the partonic dijet cross sections give the leading order predictions for the partonic 3-jet cross sections.

Direct and resolved dijet cross sections have been calculated up to the next-to-leading order in QCD[44, 49, 51, 52].

NLO predictions show the advantages that the dependence on the choice of scale is significantly reduced and that it is the first order perturbation theory which is sensitive to the jet definitions.

A further discussion of the method and program used in this work to calculate LO and NLO predictions is presented in section 2.7.

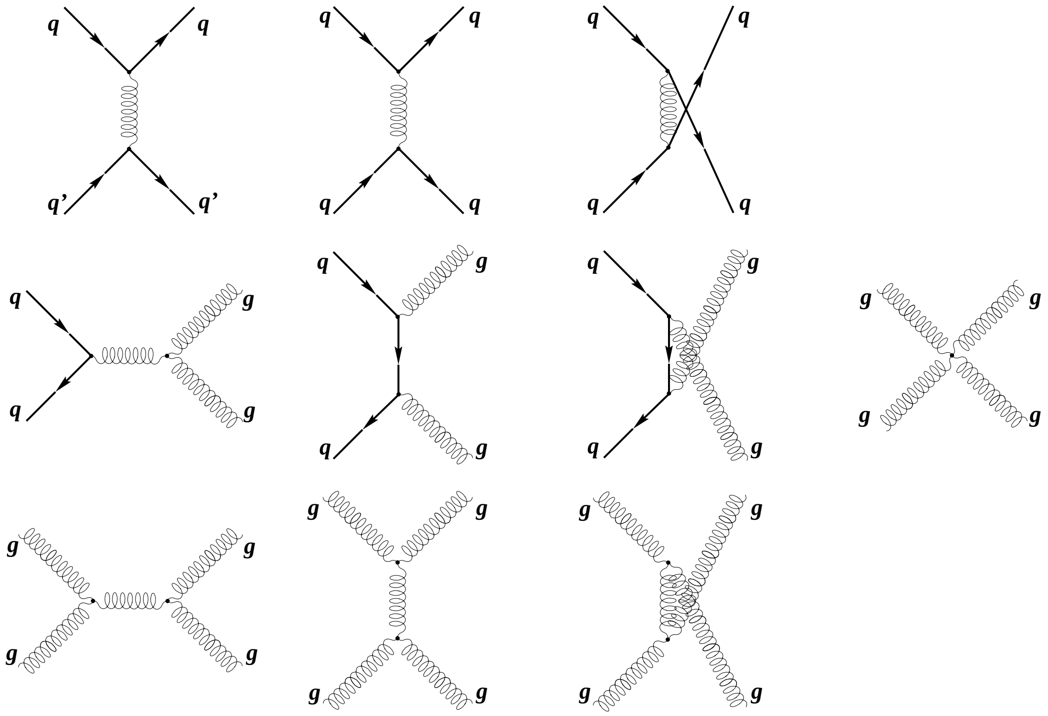

Figure 2.5: *Born diagrams for resolved photoproduction.*

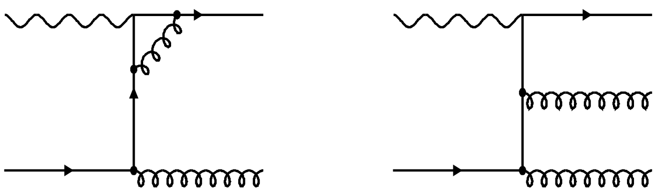

Figure 2.6: *Example of a virtual and real correction diagram for next-to-leading order direct photoproduction.*

2.2 Jetalgorithms

In order to be able to compare a measured cross section as a function of an observable to theory the observable must be infrared (IR) save. This means that two collinear partons may be replaced by one, that partons collinear with the beam momenta don't effect the measurement and that the measurement is insensitive to the emission of soft particles. These conditions can be fulfilled by a suitable application of a jet algorithm and a careful definition of the jet observables.
However there is no unique association of a jet of hadrons observed in experiments with a single parton, due to the fact that the partons carry colour and must therefore combine to colourless hadrons. Nevertheless the jet algorithm should minimise the effect of the long distance hadronization.
It has been found by comparisons of jet algorithms in DIS (e.g. [46, 47]) that the inclusive $k_\perp$ algorithm is one of the algorithms best suited to minimise hadronization effects. The inclusive $k_\perp$ has many other advantages like the fact that no longer the cone algorithm problem with overlapping jets occurs (see e.g. ref. [48]).
Because of the latter reasons in the present analysis jets are always defined using the inclusive $k_\perp$ algorithm as proposed in [54, 55]. The application of this algorithm has become standard in jet analyses at HERA [56]. It utilises a definition of jets in which not all particles are assigned to hard jets. Here it is applied in the laboratory frame with the separation parameter set to 1 and using an E_T weighted recombination scheme in which the jets are treated as massless.
The algorithm starts with a list of objects, which can be partons, hadrons or detector objects.
A recursive procedure follows:

- For each object a separation to the beam axis is defined

$$d_i = E_{T,i}^2 \tag{2.18}$$

  and for each pair of objects a separation to each other is defined

$$d_{i,j} = \min(\mathrm{E}_{\mathrm{T,i}}^2, \mathrm{E}_{\mathrm{T,j}}^2)\mathrm{R}_{\mathrm{i,j}}^2/\mathrm{R} \ . \tag{2.19}$$

  $R_{i,j}$ is the distance of the two objects in the $\eta - \phi$ plane

$$R_{i,j} = \sqrt{(\eta_i - \eta_j)^2 + (\phi_i - \phi_j)^2} \tag{2.20}$$

  and R is a separation parameter (similar to cone algorithms) of order 1.

The pseudorapidity is $\eta = -\ln(\tan\theta/2))$ and ϕ is the azimuthal angle[4].

- The smallest distance of a single object d_i or pair $d_{i,j}$ is labelled d_{min}.
- If d_{min} is a pair distance $d_{i,j}$ then the two objects i and j are merged to a new object k with:

$$E_{T,k} = E_{T,i} + E_{T,j} \tag{2.21}$$

  and

$$\begin{aligned} \eta_k &= (E_{T,i}\eta_i + E_{T,j}\eta_j)/E_{T,k} &(2.22)\\ \phi_k &= (E_{T,i}\phi_i + E_{T,j}\phi_j)/E_{T,k} &(2.23)\end{aligned}$$

- If d_{min} is a d_i then the object is not merged, removed from the list of objects and added to a list of jets.

This procedure is continued until the list of objects is empty and the output is a list of jets with increasing values of d_i ($E^2_{T,i}$).
At the end there are many jets on the list of jets. Surely the most interesting candidates are the ones with the highest E_T giving access to the hard subprocess. Therefore inclusive jet cross sections are defined, which means that one considers always events as n-jet events if they have at least n jets above some E_T treshhold.
It should be noticed that in NLO 3 parton final states it is possible that 2 partons may lie within one jet.

2.3 Observables

At the beginning of this paragraph the two longitudinal parton momenta ξ_γ and ξ_P are discussed. In dijet events the two highest E_T jets are considered and used to reconstruct ξ_p and ξ_γ. Thus the two scaled parton momenta are calculated from the jets produced in the hard subprocess, via

$$\begin{aligned} x_\gamma &= \frac{1}{2E_e y}(E_{T,1}e^{-\eta_1} + E_{T,2}e^{-\eta_2}) &(2.24)\\ x_p &= \frac{1}{2E_p}(E_{T,1}e^{\eta_1} + E_{T,2}e^{\eta_2}) &(2.25)\end{aligned}$$

[4] As in all HERA analyses the coordinate system is centred at the nominal interaction point with the positive z direction along the incident proton beam. The polar angle θ is defined with respect to the positive z axis and the azimuthal angle ϕ such that $\phi = 0$ points to the positive x axis (see section 3.1).

These are definitions of observables, x_γ and x_p, which are equal to ξ_p and ξ_γ for $2 \to 2$ processes. Here $E_{T,1}$ and $E_{T,2}$ are the transverse energies of the two jets of the hard subprocess, η_1 and η_2 are their pseudorapidities in the laboratory frame and E_e and E_p are the energies of the electron and proton beams. These relations can be easily derived from the equations 2.5 and 2.9 for leading order processes. Although the transverse energies of the jets are equal for leading order processes, eq. 2.24 and 2.25 are used in this work as definitions of observables in all orders.

In principle one could measure the dependence of the fourfold differential cross section $d\sigma_{\gamma p}/dydx_\gamma dx_p d\cos\theta^*$ on all four variables. This, however, would require a much larger data set than presently available. Therefore in this paper more inclusive quantities are presented.

Of great importance in jet physics in photoproduction (and at hadron colliders) is the measurement of the jet cross section as a function of the jet transverse energies $E_T = |\vec{p_T}|$, the jet pseudorapidities η_{jet} and the jet azimuthal angles ϕ. These observables are sensitive to the centre-of-mass frame of the hard subprocess, which is moving along the beam axis. They are also invariant under longitudinal boosts. In dijet events one has the choice to measure cross sections as a function of E_T of the highest E_T jet, $E_{T,max}$, of the second jet, $E_{T,second}$, or linear combinations of both. The cross section as a function of $E_{T,second}$ becomes IR sensitive when $E_{T,second} = E_{T,max}$ [44]. In this work cross sections as a function of $E_{T,max}$ and the mean E_T of two jets $E_{T,mean}$ are measured. In addition the transverse energy distribution of the third jet is measured for 3-jet events.

Differential cross sections in x_γ and x_p are measured for dijet events in different scale regions ($E_{T,max}$ regions) and for different x_γ or x_p cut-off values.

The cross section as a function of x_γ is also exploited for 3-jet events. Here x_γ is defined according to eq. 2.9 using

$$x_\gamma^{(3)} = \frac{1}{2E_e y}(E_{T,1}e^{-\eta_1} + E_{T,2}e^{-\eta_2} + E_{T,3}e^{-\eta_3}) \tag{2.26}$$

The momentum fraction $x_\gamma^{(3)}$ is equal to ξ_γ for leading order 3-jet production.

For comparison also the definition of eq. 2.24 is used and termed $x_\gamma^{(2)}$ to be able to distinguish this 3-jet observable from the dijet observable x_γ. If a third hard jet is present in an inclusive dijet event, then $x_\gamma < \xi_\gamma$. The 3-jet cross section as a function of $x_\gamma^{(2)}$ tests how many of the low x_γ dijet events have a third high E_T jet.

The pseudorapitities of the leading or second jet are both not IR save observables. To understand this one can consider a leading order dijet event. Then $E_{T,second} = E_{T,max}$ and let us assume that $\eta_{jet1} = 2.5$ and $\eta_{jet2} = -0.5$. A gluon radiated with infinite small E_T can give under this condition a finite change in η_{jet1} of 3 units in pseudorapidity.

IR save observables are the mean pseudorapidity $\overline{\eta} = (\eta_1 + \eta_2)/2$ for a dijet event and the absolute value of the difference in pseudorapidity of the two jets $|\eta_1 - \eta_2|$. This gives also access to θ^* via

$$\cos\theta^* = |\tanh((\eta_1 - \eta_2)/2)| \ . \tag{2.27}$$

The cross section differential in the average value of the pseudorapidities $\overline{\eta}$ is particularly sensitive to parton density functions. It is thus presented for different photon-proton centre-of-mass energies (y regions) and different scales ($E_{T,max}$ regions), cf. equations 2.24 and 2.25. Cross sections differential in $\overline{\eta} = (\eta_1 + \eta_2 + \eta_3)/3$ are also measured for 3-jet events.
The angle θ^* is sensitive to the dynamics of jet production (the matrix elements) and the corresponding differential dijet cross section is therefore evaluated for different x_γ regions for all invariant dijet masses M_{JJ} and in addition with a cut in M_{JJ}.
The different x_γ regions enhance the fraction of direct or resolved events and the cut in M_{JJ} may reduce phase space effects due to the cuts made in E_T (large values of E_T reduce events at high $\cos\theta^*$ and large values of M_{JJ} reduce events at low $\cos\theta^*$).
It is of course also interesting to measure the cross section as a function of the centre-of-mass energy of the hard subprocess $\hat{s}$. This variable is not accessible, because again only the two highest E_T jets are considered. But the invariant mass of the n-jet system M can be reconstructed. These cross sections are also important as a possible background to various new physics signals, e.g. the anomalous production of top quarks [25, 26, 27].
The understanding of n-jet invariant mass distributions is essential for the study of the hadronic decay of new particles.

2.4 Structure of the Photon

Due to the Heisenberg uncertainty principle the photon may fluctuate into quark pairs and subsequently into higher multiplicities due to gluon radiation. For sufficiently high transverse momenta of the quark pair the process $\gamma \rightarrow q\overline{q}$ can be calculated in QED. The calculation is very similar to the calculation performed in the Weizsäcker-Williams approximation. Describable are these fluctuations again with parton densities $f_{q/\gamma}$ describing the number density to find a quark in the photon carrying a momentum fraction ξ_γ of the initial photon momentum.
The QED result is:

$$f_{q/\gamma}(\xi_\gamma, \mu_\gamma) = q_f^2 \frac{\alpha}{2\pi}(\xi_\gamma^2 + (1 - \xi_\gamma)^2) \ln(\frac{\mu_\gamma^2(\xi_\gamma - 1)}{m_q^2 \xi_\gamma})$$

The electric charge of the quark q is q_f and m_q is the effective mass of a *free* quark. Unlike the proton structure the photon structure depends already without QCD corrections on a scale μ_γ, which can be interpreted in this case as the virtuality of the particle probing the photon fluctuations. Interesting is also that $f_{q/\gamma}$ increases for increasing ξ_γ.

QCD corrections to the QED result have been calculated [39]. The QCD corrections preserve the $\ln\mu_\gamma^2$ dependence and give in the LO approximation the so called *asymptotic* solution:

$$f_{q/\gamma}(\xi_\gamma,\mu_\gamma) \approx \alpha F(\xi_\gamma)\ln(\frac{\mu_\gamma^2}{\Lambda^2})$$

Since $\alpha_s \approx \ln(\mu^2/\Lambda^2)^{-1}$ this shows why the photon structure looks like $O(1/\alpha_s)$. This part of the photon structure is called *anomalous.*

The calculation is only valid for $\mu_\gamma \to \infty$, because it neglects non-asymptotic parts of the photon structure which are connected to the hadron like (VDM) part of the photon (see below).

Nevertheless the asymptotic solution diverges for small ξ values and an approach to deal with these divergencies is the construction of parton density functions of the photon at an input scale and to use the photon evolution equations to get results at higher scales, thus giving up the parameter free predictive power of QCD.

Evolution equations for the photon pdfs can be written as:

$$\begin{aligned}\frac{\mathrm{d}f_{q/\gamma}(\xi_\gamma,\mu_\gamma)}{\mathrm{d}\ln\mu_f^2} &= \frac{\alpha}{2\pi}q_f^2 P_{q\gamma}(\xi_\gamma) + \frac{\alpha_s(\mu_\gamma)}{2\pi}\int_{\xi_\gamma}^1 \frac{\mathrm{d}z}{z}\Bigg(P_{qg}(z)f_{g/\gamma}(\frac{\xi_\gamma}{z},\mu_\gamma)+ \\ &\quad P_{qq}(z)f_{q/\gamma}(\frac{\xi_\gamma}{z},\mu_\gamma)\Bigg) \qquad (2.28)\\ \frac{\mathrm{d}f_{g/\gamma}(\xi_\gamma,\mu_\gamma)}{\mathrm{d}\ln\mu_\gamma^2} &= \frac{\alpha_s(\mu_\gamma)}{2\pi}\int_{\xi_\gamma}^1 \frac{\mathrm{d}z}{z}\Bigg(P_{gg}(z)f_{g/\gamma}(\frac{\xi_\gamma}{z},\mu_\gamma)+ \\ &\quad \sum_q P_{gq}(z)f_{q/\gamma}(\frac{\xi_\gamma}{z},\mu_\gamma)\Bigg) \qquad (2.29)\end{aligned}$$

The photon may also couple to bound $q\overline{q}$ states which carry the same quantum numbers as the photon, such as the ρ, ω or the ϕ meson. These fluctuations are due to a missing hard scale not calculable in perturbation theory, but they can reasonably be described by the *Vector Meson Dominance* model (VDM). The VDM model interprets the photon as a superposition of vector meson states.

A good knowledge of the struture of the photon is of utmost importance as a test of the predictive power of perturbative QCD.

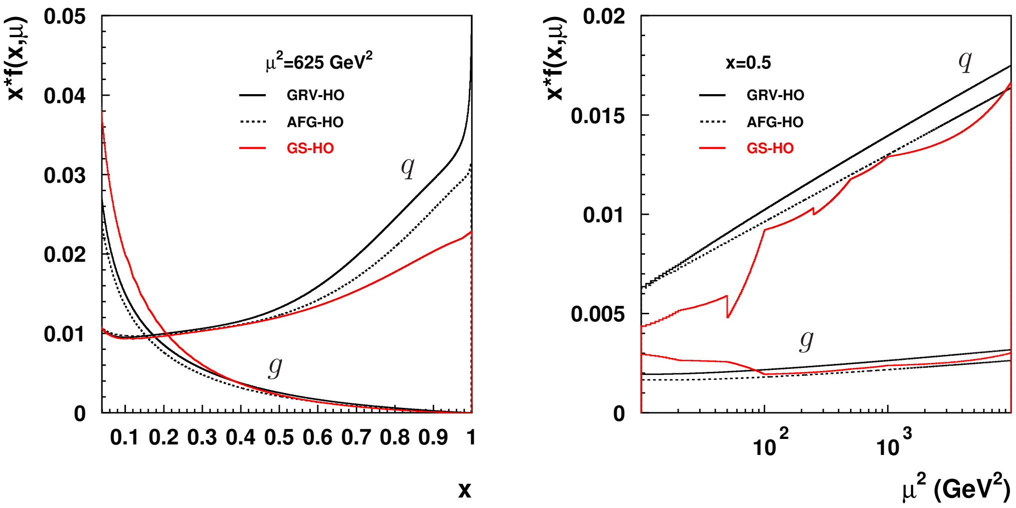

Figure 2.7: *Different next-to-leading order parameterization of photon pdfs as a function of x (equal to ξ_γ) for a fixed scale μ (left) and as a function of the squared of the scale for a fixed x (right). The upper lines in the Figures correspond to different parameterizations of the summed quark pdf and the lower lines correspond to the gluon pdfs.*

Photon quark densities have been determined in experiments at e^+e^--colliders[37] which investigate the photon structure function F_2^γ, where x_γ between 0.01 and $0.8-1$ and scales between 0.2 to $780\,\mathrm{GeV}^2$ have been reached [38]. At high x_γ values and high scales the uncertainties of these experiments are large.
The gluon density of the photon is only poorly known to date. From F_2^γ measurements the gluon density can only be calculated via the evolution model. The photoproduction of jets is directly sensitive to the gluon density of the photon. But up to now these results suffer from large uncertainties.
One reason is that gluon reactions are only dominating the cross section at low ξ_γ, corresponding to low E_T. Unfortunately at low E_T the interpretation of the measured cross section is difficult due to large non-perturbative effects. The analysis presented in this work tests the gluon density in the photon directly at relatively high ξ_γ.
Today leading and next-to-leading order parameterizations of photon parton densities are obtained by several groups.
Since this work is attributed to a comparison of the data to NLO calculations only NLO parametrizations of the photon structure are considered.
There are pdfs from three different groups available.

- **Glück, Reya and Vogt**
  GRV [62] constructed the photon parameterization at a low input scale of $0.3\,\mathrm{GeV}^2$, where the valence quarks distributions have the same shape as the

pion structure function. This means that the anomalous component of the photon structure is assumed to vanish at the input scale. The anomalous component should be automatically generated by the photon evolution equations. NLO evolution equations for massless quarks with $\Lambda = 200$ MeV are used in the so called DIS_γ factorization scheme.

They allowed for one free parameter fixing the normalization of the input distributions. This parameter was fitted to a large set of F_2^γ data. The NLO pdf is termed GRV-HO.

- **Aurenche, Fontannaz and Guillet**
  The AFG [67] strategy is very similar. The starting scale is $0.5\,\mathrm{GeV}^2$ and again the input at this scale is purely hadron-like, a coherent sum of vector mesons. The used factorization scheme is the $\overline{MS}$ scheme and the NLO evolution is performed using 4 flavours and $\Lambda = 200$ MeV. A scale factor is provided to adjust the VDM contribution, the default value is 1. The NLO pdf is termed AFG-HO.

- **Gordon and Storrow**
  The GS [68] parton densities are not used in this work, because no reliable data grid is available. Figure 2.7 shows that the pdfs do not follow the $\log \mu^2$ prediction. Problems of the x behaviour of this parametrization were also reported in [69]. The NLO pdf is termed GS-HO.

Figure 2.7 shows a comparison of the parton densities for a fixed ξ_γ of 0.5 as a function of the scale and for a fixed scale of $625\mathrm{GeV}^2$ as a function of ξ_γ. The GRV and AFG pdfs show only very small differences, which are much smaller than the current uncertainties of photon structure.

2.5 Structure of the Proton

Photoproduction jet data is sensitive to the parton densities of the proton. Because this analysis investigates events with jets at high transverse energies the accessible x_p range is rather high ($x_p > 0.05$).
In this kinematical regime, the quark densities are well known from deeply inelastic scattering data, while the gluon density has uncertainties of the order 10 to 50%[40]. The discussion will therefore concentrate on the gluon density of the proton.
Many signal and background processes at HERA, the Tevatron and the LHC have a gluon in the initial state, e.g. the Higgs boson production via $gg \to h$. It is thus

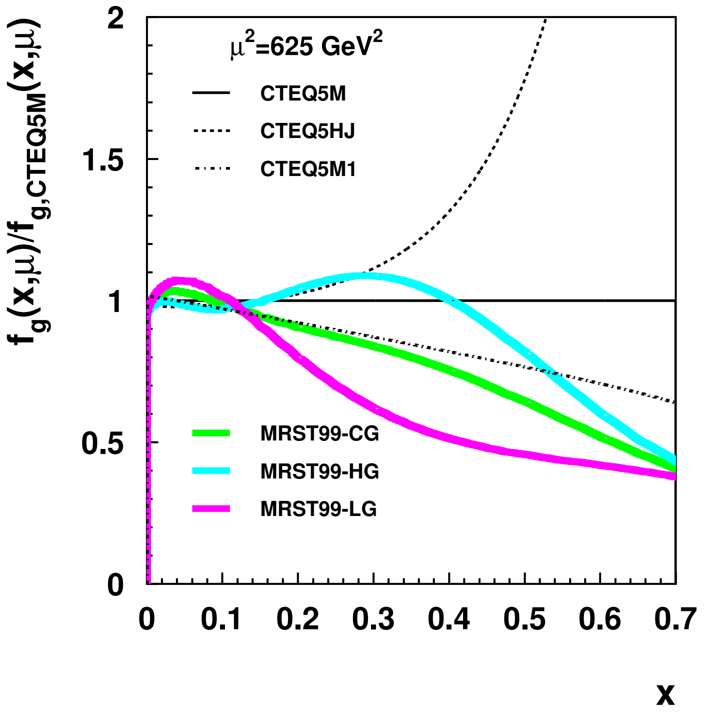

Figure 2.8: *The ratio of different next-to-leading order parametrizations of the gluon densities to the CTEQ5M gluon density. The ratios are shown as a function of x (equal to ξ_P) for a squared scale $\mu^2 = 625$ GeV^2.*

important to reduce the uncertainty of the gluon parton distribution, especially at high ξ. Likewise jet photoproduction tests the universality of the proton pdfs.

There are a lot of different proton pdfs sets available. In this work two of the most popular sets are used for the NLO calculations. Both CTEQ5 [64] and the MRST99 [65] pdfs are obtained from global fits (primary to DIS data). They use NLO evolution equations in the $\overline{MS}$ scheme and Λ_{QCD} was set to 0.226 GeV ($\alpha_s(M_Z) = 0.118$) in the CTEQ5M fit and 0.220 GeV ($\alpha_s(M_Z) = 0.117.5$) in the MRST99 fit. A 2-loop α_s with 5 flavours was used.

The MRST group provides 3 different pdf sets, MRST99 1-3, representing the uncertainty of the gluon distribution in their fit. The CTEQ group provides pdfs with the gluon enhanced at large ξ (CTEQ5HJ) and an update of CTEQ5M with an improved evolution code (CTEQ5M1).

These gluon densities are compared as a function of ξ_p for $\mu_P^2 = 625\,\mathrm{GeV}^2$ in Figure 2.8 showing increasing differences with increasing ξ_p values.

2.6 Definition of the Phase Space

In this section the phase space of the measured cross section is introduced. Most cuts are due to experimental reasons as discussed in the next chapter.
This work considers jets at high transverse momentum. The theoretical reason is that first high E_T provides a natural hard scale for perturbative QCD calculations.
Second at lower E_T such as ≈ 5 GeV the cross section may be dominated by soft physics, e.g. the difference of the cross sections with and without the so called *soft underlying event* at low x_γ is approximately 100% [91]. The aim of this work is to address hard processes exclusively.
Asymmetric cuts on the E_T of the two jets with the highest transverse energies must be applied to avoid regions of phase space affected by uncertainties in the NLO dijet calculation [44]. On the other hand a highly asymmetric cut causes large NLO corrections and a pronounced dependence on the choice of scale (see Appendix C).
The jet selection criteria therefore required an E_T of the highest transverse energy jet $E_{T,max} > 25$ GeV, and the transverse energy of the second highest transverse energy jet $E_{T,second} > 15$ GeV.
The pseudorapidity of each jet η_{jet} was restricted to $-0.5 < \eta_{jet} < 2.5$. The measured kinematic region was restricted to $0.1 < y < 0.9$ and $Q^2 < 1\,\mathrm{GeV}^2$.
The kinematic range of the measured jet cross sections is summarized in Table 2.1.

$Q^2 < 1$ GeV^2
$0.1 < y < 0.9$
$E_{T,max} > 25$ GeV
$E_{T,second} > 15$ GeV
3-jet production: $E_{T,third} > 15$ GeV
$-0.5 < \eta_{jet} < 2.5$

Table 2.1: *The definition of the phase space of the measured jet cross sections.*

2.7 Fixed Order QCD Calculations

The goal of this analysis is the comparison of the measured cross sections to perturbative QCD calculations at the parton level. The LO and NLO dijet cross sections were computed using a program based on the subtraction method [44, 63] for the analytic cancellation of infrared (soft and collinear) singularities.
Roughly the idea in the subtraction method [45] is to add and subtract an additional term to the cross section such that one can perform an analytic integration.

The calculation of the dijet cross sections was performed by deriving the γP result for the resolved part at 8 fixed photon-proton centre-of-mass energies ($W_{\gamma,P}$ bins) and a subsequent multiplication with the corresponding integrated photon flux. The uncertainty of this method was found to be $< 1\%$ by increasing the number of $W_{\gamma,P}$ bins. For the direct part *ep* scattering was calculated.

In calculating LO and NLO cross sections a 2-loop α_s was taken with 5 active flavours. Λ_{QCD} was set to 0.226 GeV ($\alpha_s(M_Z) = 0.118$), which is the value used in the proton parton density functions. CTEQ5M [64] parton density functions were chosen for the proton whereas MRST99 [65] parton density functions were selected to test the dependence of the NLO cross sections on the proton pdfs at the same value of Λ_{QCD}. For the photon GRV-HO [66] is used as a main setting and the parameterization of AFG-HO [67] to study the dependence of the results on the choice of the photon pdfs. The renormalization scale μ_r and the factorization scales μ_p and μ_γ were, event by event, set to the sum of the transverse energies of the outgoing partons divided by two.

The QCD program allows the variation of this common scale. It was varied from 0.5 to 2 times the default scale to estimate the scale uncertainty in the NLO calculation. This uncertainty turned out to vary between ± 10 and $\pm 20\%$ in the measured kinematic range.

NLO pdfs and α_s have been used in the LO and NLO calculation to compare the LO and NLO hard scattering cross sections. In the dijet analysis the difference between the NLO and LO prediction gives information of higher order effects. In a 3-jet analysis the comparison of the LO prediction to the data may predict the size of higher order corrections.

It was tried to compare the results of the NLO calculation with a program [50] which uses the phase space slicing method to deal with the cancellation of infrared singularities. The results are found to be compatible within 20% for a slicing parameter of 0.001. In this phase space slicing method, the singular phase space regions are seperated by introducing an invariant mass cut-off, the slicing parameter. The calculated cross sections should be independent on the choice of this parameter, at least in a sensible range.

Unfortunately is was found that the result of this program crucially depends on the choice of the slicing parameter. Differences up to 100 % occurred. The data are only compared to the theoretically favoured subtraction method program.

In addition the data are compared to the predictions of NLO QCD corrected for hadronization effects, which are defined as the ratio of the cross sections with jets reconstructed from hadrons and from partons before hadronization. The hadronization effects are calculated with PYTHIA and HERWIG and the mean value of the two

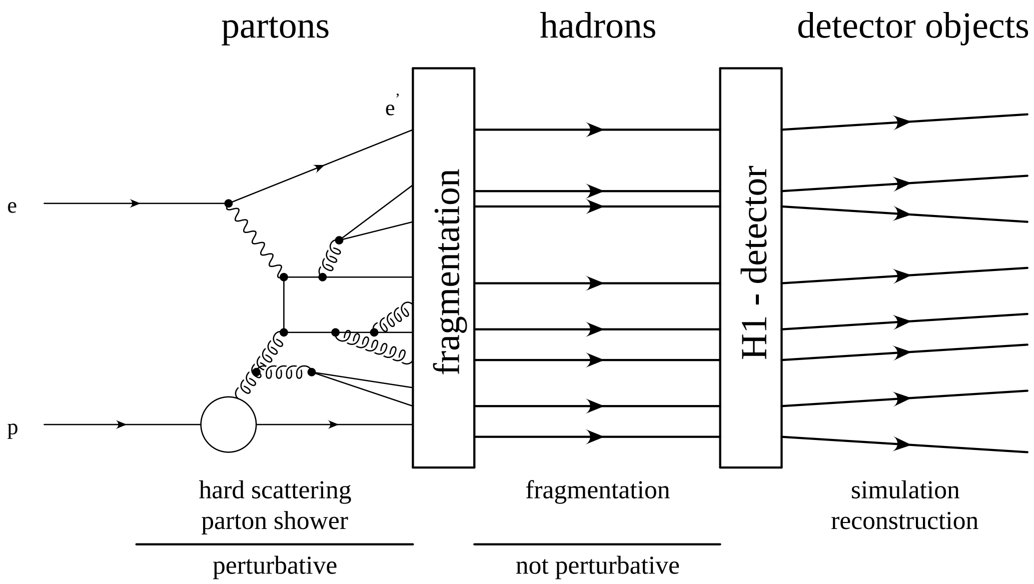

Figure 2.9: *Schematic view of an event generator and the detector simulation.*

predictions is used for corrections. Here the difference between the two Monte Carlo models is in general small and at maximum ≈ 10%. The jets built out of partons are found to be well correlated with the jets built out of hadrons.

2.8 Monte Carlo Event Generators

Detector effects like limited acceptance or resolution have to be considered for a comparison of the data with theory. Furthermore the impact of non perturbative physics, e.g. hadronization, need to be estimated. This is done using QCD Monte Carlo event generators, which allow the creation of artificial events. The generators consider the leading order direct and resolved processes, additional QCD radiation, a simulation of the beam remnants and hadronization. Moreover the created events can also be passed through a detailed detector simulation performed by GEANT [60]. Figure 2.9 shows a schematic view of this procedure.

2.8.1 Pythia and Herwig

Both Monte Carlo event generators, PYTHIA and HERWIG, are able to generate various processes.
To simulate the direct and resolved photoproduction of jets, the PYTHIA 5.7 [57] and

HERWIG 5.9 [59] event generators were used followed by a full detector simulation [60] of all Monte Carlo events. Both programs contain the Born level QCD hard scattering matrix elements, regulated by a minimum cut-off in transverse momentum. GRV-LO [61, 62] parton density functions (pdfs) for the proton and photon were chosen. The phase space of the generated events covers $Q^2 < 4$ GeV^2 and $y < 0.98$. For the PYTHIA generation a 1-loop α_s is taken with $\Lambda = 200$ MeV, while for HERWIG a 2-loop α_s is taken with $\Lambda = 291$ MeV [85, 3].
HERWIG uses the equivalent photon approximation to simulate the photon spectrum, while PYTHIA has been run in the photon-proton mode and has been interfaced with IJRAY [58] to simulate the photon spectrum.
Leading logarithmic parton showers are used to represent higher order QCD radiation. In the parton shower ansatz a multiple number of branchings of partons characterized by a virtuality scale Q_0 are considered (using splitting functions). The minimum Q_0 is typically 1 GeV, the maximum Q_0 is matched to the leading order $2 \rightarrow 2$ matrix elements .
Perturbation theory is not valid at large distances, because of the increasing strong force. Here the coloured partons are transformed to colourless hadrons.
To perform this transformation, the Lund String model is applied in PYTHIA to hadronize the outgoing partons, while in HERWIG the cluster hadronization approach is used.
In the Lund String model a colour field with constant energy per unit length (a string) is stretched between the partons. Gluons are supposed to produce kinks on the strings. At the end of the procedure the strings break up into hadrons.
In the cluster model colour-singlet clusters of neighbouring partons are formed, which decay into hadrons. Details of the two models can be found in [57, 59].
Multiple interactions between the proton and the resolved photon are dealt with in PYTHIA by adding additional interactions between spectator partons within the same event. These processes are calculated by extending the perturbative parton-parton scattering to a low E_T cut-off.
In HERWIG multiple interactions are included by producing in a fraction P' of the resolved events so called *soft underlying events*. These interactions are parameterized using experimental results of soft hadron-hadron scattering. It is found in section 3.4 that P' has to be set to $\sim$30-35%.
Both HERWIG and PYTHIA contain only the leading order $2 \rightarrow 2$ photoproduction processes. As a consequence they are not able to describe the absolute dijet and 3-jet cross sections. To get a estimate of the jet cross sections the PYTHIA dijet cross section was scaled by a factor of 1.2 and the HERWIG dijet cross section was scaled by a factor of 2. These scaling factors are derived by comparing the measured total

dijet cross section to the unscaled PYTHIA and HERWIG prediction. In this work all PYTHIA and HERWIG dijet cross sections shown are scaled by these factors. Especially HERWIG needs a different (compared to the dijet case) scale factor to describe the 3-jet cross section. This is explained in section 3.3.2.

2.8.2 Other Generators

DIS

Neutral current (NC) and charged current (CC) event generators are used to estimate the expected background from the processes. The ARIADNE [83] Monte Carlo interfaced with DJANGO [84] was used to generate NC events with $Q^2 > 300$ GeV^2 and high Q^2 CC events. Neutral current high Q^2 events were found to be the main source of background. RAPGAP was used to determine the low Q^2 NC DIS background for $1 < Q^2 < 300$ GeV^2.

W production

Jets with high transverse momentum also result from the hadronic decay of W or Z^0 bosons. For the analysis presented in this work the contribution of W bosons is estimated with the EPVEC Monte Carlo generator [53] to be 5-6 events. The Z^0 contribution is expected to be even smaller such that the background from both processes is safely neglected in the following. A search for W bosons in the jet channel needs a special search strategy and is still under investigation [24].
The H1 experiment has reported [23] an excess of events with an isolated lepton (e and μ), missing transverse momentum and a high E_T hadronic system. A ZEUS analysis [22] could not corroborate this excess. The kinematics of these events are mostly compatible with a leptonic W decay and a high E_T jet. New physics could enhance the cross section of W+jet events such that it is already observable in the 3-jet cross sections.

3
The Experiment

This chapter explains the measurement of photoproduction dijet and 3-jet cross sections. It starts with an outline of HERA and the H1 detector. Furthermore the selection of photoproduction jet events and an exploration of the event properties is discussed. Finally the unfolding procedure and the systematic uncertainties of the measurement are presented.

3.1 The H1 Detector at HERA

The electron-proton storage ring HERA (Hadron Elektron Ring Anlage) at DESY (Deutsches Electronen Synchrotron) is a unique machinery to study the scattering of electrons and protons and the photoproduction of hard jets. This machinery is a continuation of famous electron nucleon scattering experiments, such as the Hofstadter and SLAC-MIT experiments.

Unlike these previous experiments the HERA accelerator does not collide the electrons on a fixed nucleon target. HERA accelerates unbound protons and is thus the only facility in the world in which accelerated electrons and protons collide.

In HERA (see Figure 3.1) 27.6 GeV positrons collided with 820 GeV protons in the years 1994-1997, resulting in a centre-of-mass energy of about 300 GeV. In 1998 the proton beam energy was increased to 920 GeV and electrons were accelerated. In 1999 HERA was switched back to the acceleration of positrons.

The HERA tunnel is 6.3 km in circumference and 10 m - 25 m under ground. The magnets of the electron storage ring contain normal conductors and operate at room temperature. The magnets of the proton storage ring produce a magnetic field of 4.7 Tesla for bending the high momentum proton beam through the ring. To accomplish this, superconducting magnets which operate at a temperature of 4.4° K (−269° C) have been constructed. The protons and electrons are stored in up to 220 bunches.

The physics program of HERA led to the construction of two detectors, H1 and ZEUS,

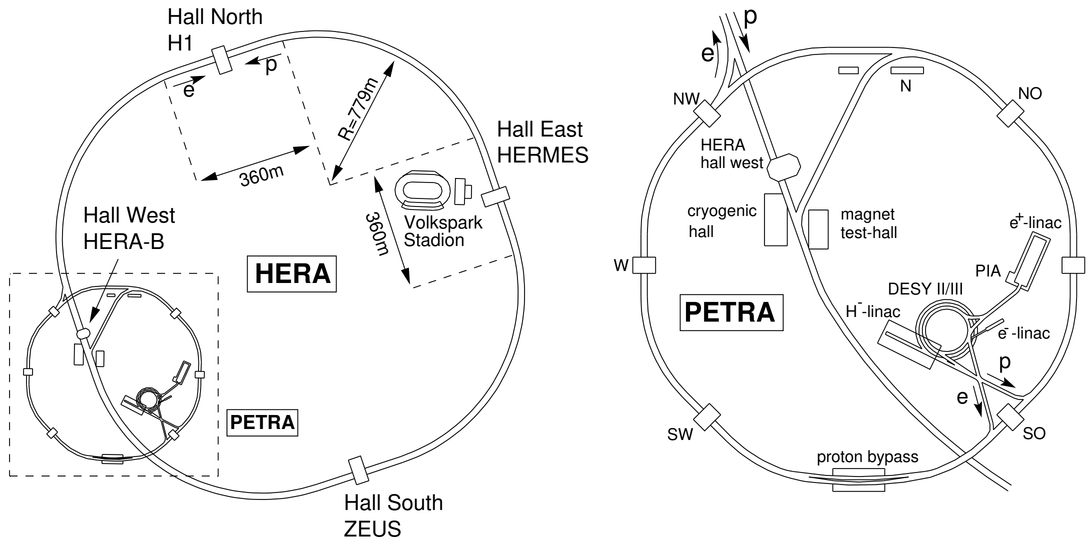

Figure 3.1: *The electron-proton collider HERA and preaccelerators.*

dedicated to the measurement of electron proton collisions. H1 and ZEUS are found on the interaction zones, where each 96 ns proton and electron bunches may collide. In addition there are two beam-target experiments, HERMES and HERA-B.

The experimental work described in the following is based on a data sample collected with the H1 detector from 1995 – 1997. Thus a brief description of the main components of the H1 detector is necessary to understand the analysis procedure. The detector [1] is described in detail in [70].

The identification and energy measurement of the scattered electron, high resolution and granularity for the hadronic system and a good hermiticity to recognize missing transverse energy were from importance in designing the detector. In addition the unequal beam energies had to be considered in a asymmetric detector configuration as can be seen from Figure 3.2 . The right-handed coordinate system is centred at the nominal interaction point ($z = 0$) with the positive z direction along the incident proton beam. The positive x-axis points to the ring centre, the positive y-axis points upwards. The polar angle θ is defined with respect to the positive z axis and the azimuthal angle ϕ such that $\phi = 0$ points to the positive x axis.

In the middle and forward region of the H1 detector emphasis is placed on measuring high momentum jets with a fine granulated Liquid Argon calorimeter (LAr) [72, 71].

[1] With the luminosity upgrade (in 2001) there have been changes and additions to the H1 detector. The detector is described at the time the data was taken (HERAI) and important changes after the luminosity upgrade are briefly added.

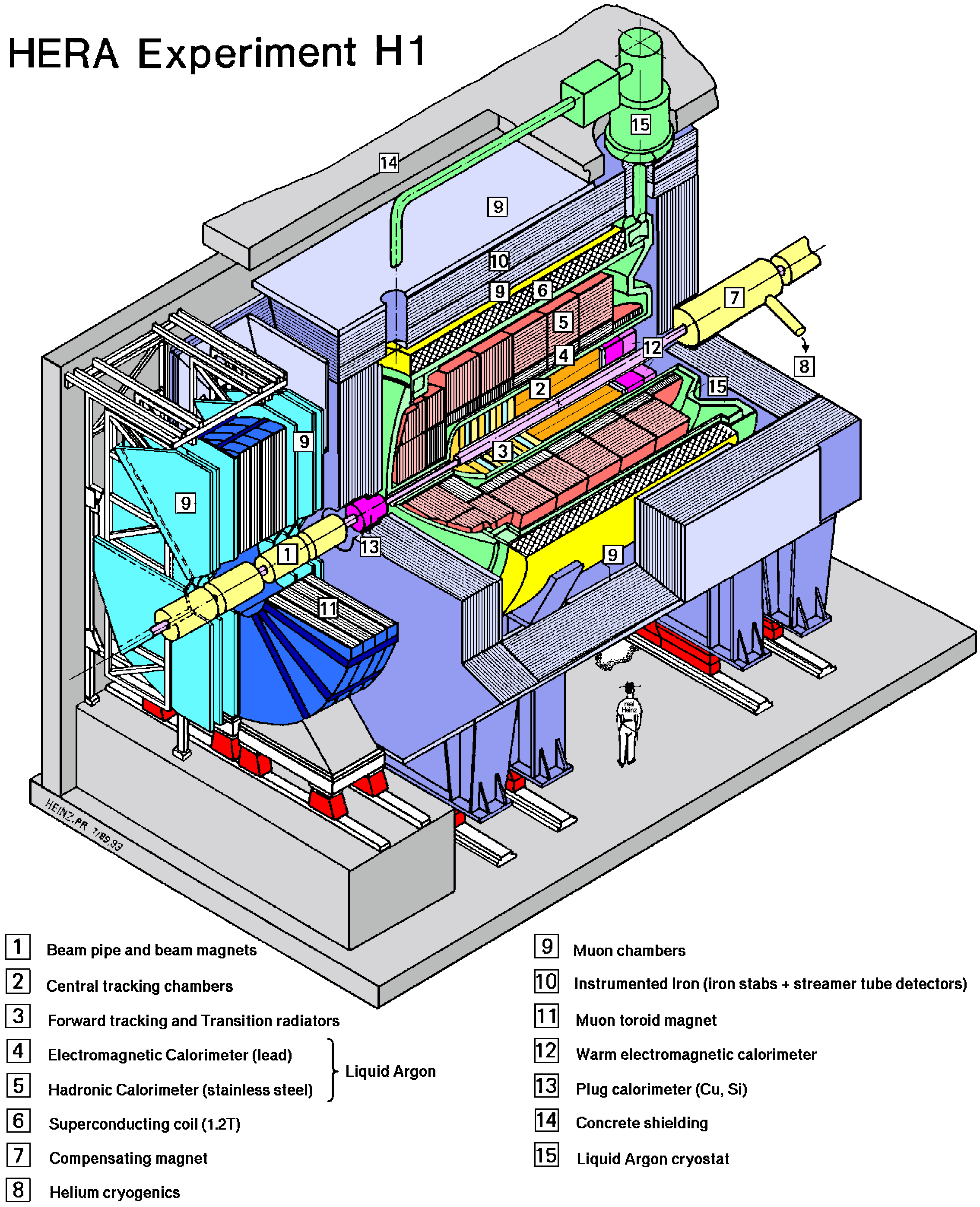

Figure 3.2: *An isometric view of the H1 detector.*

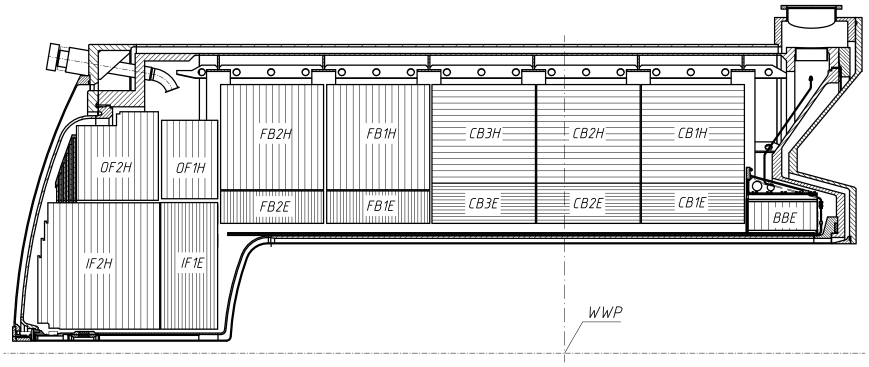

Figure 3.3: *Side view of the liquid argon calorimeter.*

Since the electron most likely scatters in backward direction the SpaCal [73] calorimeter has been build there in order to support the electron and hadronic final state identification. Both main calorimeters, LAr and SpaCal are used in this analysis to trigger events, reconstruct the hadronic energy of the final state and selecting photoproduction events by eliminating events with an identified scattered electron. The use of tracking detectors improves the measurement of the momenta of charged particles. Particles of very low momenta may not reach the main calorimeters and therefore tracks of the central tracking detector (CJC) are used to supplement the measurement of hadronic energy flow. This detector is in addition used to reconstruct the interaction vertex.

3.1.1 Calorimetry

The H1 detector comprises four distinct calorimeters: the liquid argon (LAr) calorimeter, the spaghetti calorimeter (SpaCal), the tail catcher and the plug calorimeter.

The Liquid Argon Calorimeter

The LAr covers the polar angle range $4° < \theta < 154°$, corresponding to a laboratory pseudorapidity range of $-1.47 < \eta < 3.35$, with full azimuthal acceptance. It is situated inside the magnetic coil in order to minimise the passive material and improving the electron recognition and the hadronic energy measurement. It is segmented along the beam axis in eight *wheels* and each wheel is constructed from identical *octants*. Particles deposit their energies via different mechanisms,

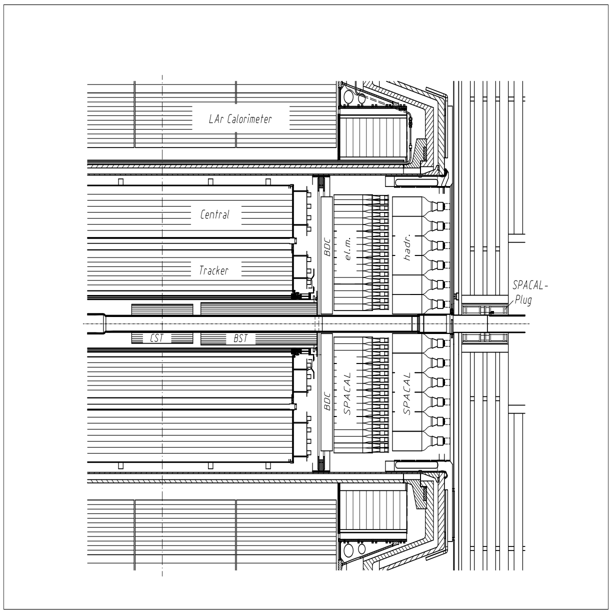

Figure 3.4: *Side view of the backward region of the H1 detector showing the position of the SpaCal.*

which requires the LAr to be divided in an inner electromagnetic section (EMC) and an outer hadronic section (HAC). The electromagnetic and hadronic sections use lead and stainless steel absorber plates, respectively. Liquid Argon is in both cases used as the active medium because of its good stability, ease of calibration, possibility of fine granularity and homogeneity. The energy resolution measured in test beams is $\sigma_{e.m.}(E)/E \approx 0.12/\sqrt{E(GeV)}$ for an electromagnetic shower and $\sigma_{had.}(E)/E \approx 0.5/\sqrt{E(GeV)}$ for a hadronic shower. The total depth of both section varies between 5 and 8 interaction lengths. The electromagnetic energy scale uncertainty is about 1%. For high transverse momentum jets the hadronic energy scale uncertainty is determined to be 2% (see chapter 2.2.5). The LAr is non-compensating, i.e. the response to hadrons is about 30% lower than the response to electrons of the same energy. An energy dependent reweighting is used to equalize the response.

The SpaCal Calorimeter

The angular region $153^\circ < \theta < 177.8^\circ$ is covered by the *spaghetti calorimeter*, SpaCal, a scintillating-fibre calorimeter with lead absorbers. The main design goals of the calorimeter are a good coverage of the region close to the beam pipe, high angular and energy resolution for electrons and a capability of providing hadronic energy measurement. The SpaCal has also an electromagnetic and hadronic section. The electromagnetic energy resolution is $\sigma_{e.m.}(E)/E \approx 7.1\%/\sqrt{E(GeV)}$ [73]. In the hadronic section, energies are measured with a resolution of $\sigma_{had.}(E)/E \approx 30\%/\sqrt{E(GeV)}$. The hadronic energy scale of the SpaCal calorimeter is known to 7%. A scattered electron with an energy of ≈ 5 GeV at about $175° - 177°$ results in a measured Q^2 of $0.5 - 1\,\mathrm{GeV}^2$. This gives the upper Q^2 range of this analysis.

Tail Catcher, Plug and Electron Tagger

The instrumented iron is equipped with so called strips and pads. While the strips are used for muon identification the rectangular electrodes (pads) are used to measure the energy of hadrons penetrating the LAr calorimeter (tail catcher).
The plug calorimeter closes the gap between the LAr and the beam pipe in the forward direction. Both tail catcher and plug are not used in this analysis.
The electron tagger is located in the HERA tunnel at $z = -33$m. It has an angular coverage of $\theta > 179.7°$. The electron tagger marks the energy of the electron inducing a photoproduction event and is used in coincidence with the photon tagger to monitor the luminosity.
The luminosity determination is based on the measurement of the $ep \rightarrow ep\gamma$ Bethe-Heitler process, where the positron and photon are detected in crystal Cherenkov calorimeters located downstream of the interaction point. This process has a large and good known cross section.

3.1.2 Tracking

The H1 tracking system consists (HERA1 status) of the two central jet chambers (CJC1 and CJC2), central inner and outer trackers for measuring the z coordinate (CIZ and COZ), central multiwire proportional chambers (CIP and COP), forward (FTD) and backward (BDC) tracking detectors and central and backward silicon microvertex detectors (CST,BST). During the luminosity upgrade the CIZ and the BDC have been removed and a forward silicon microvertex detector FST has been added. The tracking detectors are immersed in the 1.15 Tesla magnetic field. The CJC consists of two concentric cylindrical drift chambers, coaxial with the beam-line, with a polar angle coverage of $15° < \theta < 165°$. The spatial resolution is 170μm in the $r - \phi$ plane, the z coordinate is measured with a resolution of $\sigma_z = 22\,\mathrm{cm}$. From these detectors the transverse momentum of charged tracks can be determined to $\sigma p_T/p_T < 0.01\,p_T(GeV)$. Two thin drift chambers (CIZ and COZ) improve the measurement of the z coordinate with an accuracy of $\sigma_z \approx 350\,\mu$m with wires perpendicular to the beam axis. Each of the z chambers is supported by the proportional chambers, CIP and COP, which deliver a fast trigger signal.

3.1.3 Muon System

Muon identification was used in this analysis to remove non collision background events, e.g. events overlaid by cosmic muons. Muons are usually identified by looking for tracks of the inner trackers which point to tracks of the Muon System. Two parts of the H1 detector are specially designed to identify muons, the Central Muon System (part of the iron yoke) and the Forward Muon spectrometer. All major components of the detector are surrounded by the iron yoke of the main solenoid. This iron yoke is interleaved with slits and these slits are equipped with limited streamer tubes (LSTs). The LSTs are used for the measurement of penetrating tracks.

3.1.4 H1 Trigger System

A trigger system should be able to give a fast decision for the acquisition of *interesting* events and the separation of background events. Background sources are e.g. interaction of protons with gas in the beam pipe (beam-gas) and with material of the beam tube (beam-wall), beam halo muons and muons of cosmic radiation. The interesting physic processes cover a wide range of rates (or cross sections), from tagged photoproduction with a rate of 20-30 Hz to rare processes at high transverse energies which occur only a few times per day or week. The background rates are in the order of 1 kHz. In the H1 interaction region electron and proton bunches collide with a rate of 10.4 MHz.

The H1 Trigger System is divided into four levels in order to filter the interesting events. The first and second level systems (L1 and L2) are phase locked to the HERA accelerator clock of 10.4 MHz. The L1 system provides a trigger decision for each bunch crossing after 2 μs without causing dead time. Information of several subdetectors (trigger elements) are used to provide a decision. The LAr calorimeter provides signals to the central trigger which are used to trigger NC, CC and photoproduction jet events. These signals are derived from the summed energies in parts (Big-Towers) of the LAr or from the total energy of the LAr. A detailed description of the LAr trigger can be found in [75].

The trigger elements are combined by the central trigger logic to 128 subtriggers. Some subdetectors need several bunch crossings (BC) time to provide the information, which is meanwhile stored into pipelines.

The L2 system decision is presently derived within 20 μs from a combination of two independent hardware systems, a topological correlation and a neural network. The L3 system is not yet implemented.

The L4 trigger is based on a full (but simplified) reconstruction of the event and decides in approximately 100 ms. The events accepted by L4 are written on tape.

The data is then fully reconstructed and written in a compressed format to data summary tapes (DST).

3.2 Data Selection

The data sample was collected with the H1 detector from 1995-97, when protons of 820 GeV energy collided with positrons of 27.6 GeV energy, in HERA, resulting in a centre-of-mass energy of 300 GeV. Candidate events are selected by the H1 trigger system and are written on tape. In the following the selection of a clean jet photoproduction sample out of the enormous amount of events passing the trigger criteria is described. The first step was the selection of so called *good* and *medium* "runs". The term "run" defines a data taking period of at least 2 hours in which the detector conditions are rather stable and for which the integrated luminosity is determined.
To require good and medium runs means that all detector components relevant for the presented analysis are in operation. These are both CJC1 and CJC2, the LAr, the SpaCal and the Luminosity system. In addition it is required, on an event by event basis, that the high voltage and other status informations of CJC1 and CJC2, the LAr and the SpaCal are at the nominal settings.
To reduce the background it was demanded that an event vertex was reconstructed within 35 cm of the nominal z position of the vertex.
The next important step in selecting jet photoproduction is the reconstruction of the hadronic final state.

3.2.1 Photoproduction Event Selection

Reconstruction of the hadronic final state

The hadronic final state may be reconstructed in many different ways. Mostly the information of the calorimeters is used. Neighbouring calorimeter cells are combined with an algorithm to *clusters*.
Since the majority of the energy of high transverse energy jets is measured in the calorimeters, often calorimeter clusters are used alone to reconstruct the hadronic final state. Then, however the measured energy is typically to low, because particles originating from the event vertex lose some of their energies due to dead material on their way to the calorimeters. Also the momentum resolution for particles with low momentum is much better for tracks than for the calorimeters.
In this analysis both, energy deposits in the calorimeters and low momentum tracks in the CJC are combined to reconstruct the hadronic energy of the events. The

method [74, 76] avoids double counting and the constructed objects are called *HFS* objects. Tracks with transverse momentum $p_{T,Track} < 2$ GeV and which have been constrained to the event vertex, are extrapolated to the calorimeters. The cut in the tracks transverse momentum takes into account that the track momentum resolution worsens with increasing track momentum (2 GeV is the default choice). Energy in electromagnetic (hadronic) clusters within a cylinder of radius 25 cm (50 cm) around the extrapolated track, is assigned to the track. If the track energy is smaller than the energy within the cylinder, those cluster with the smallest distance of closest approach to the track are discarded until the total energy of the discarded clusters is approximately equal to the track energy. Otherwise the track momentum is taken and all clusters within the cylinder are discarded. If the track does not point to the calorimeter also the track momentum is taken.
The HFS objects are therefore formed out of clusters and tracks and give an improved reconstruction of the hadronic final state. These HFS objects have been calibrated with the so called *high Q^2 calibration*. This calibration is based on a fitting procedure of the transverse energy balance between the electron and the hadronic final state of high Q^2 data.
The H1 electron finding algorithm QESCAT [77] has been used to identify the electron. Electrons are identified using criteria for the isolation to hadronic energies and estimators for the shower profile. All isolation parameters of the algorithm are set to the default values and no linking between the electron cluster and track is required. The algorithm searches for electrons in the LAr, SpaCal and the electron tagger. QESCAT uses the QECFWD [78] finder for the search for electrons in the LAr.
The electron does not belong to the HFS objects, if it has been identified.

Selection of high transverse energy jets

Once the hadronic final state objects are defined, events with high transverse hadronic energy can be selected by simply adding up the transverse energy $E_{T,i}$ of all HFS objects i. A preselection was done by demanding the total transverse energy to exceed 30 GeV and one jet with a transverse momentum to exceed 15 GeV besides the latter requirement. Out of the preselection a dijet sample has been selected. The jet selection criteria required an E_T of the highest transverse energy jet $E_{T,max} > 25$ GeV, and the transverse energy of the second highest transverse energy jet $E_{T,second} > 15$ GeV. Note that the dijet sample has already a total transverse energy greater than 40 GeV. Until otherwise stated the observables will be presented using the *final* calibration, which will be presented in section 3.2.5.
Further cuts have to be made to sort out the photoproduction jet events from the background events. These cuts are explained in the following.

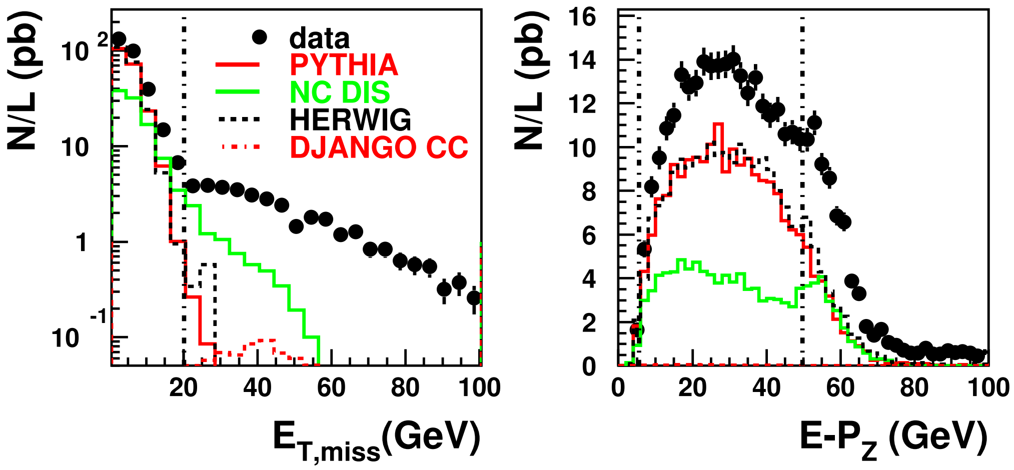

Figure 3.5: *Luminosity normalized distributions of the variable $E_{T,miss}$ and $E - P_Z$. Only the jet selection criteria are required. The vertical dash dotted line refers to the cuts discussed in the text. Here, as well as in the following figures unless explicitly stated otherwise the error bars denote the statistical error.*

3.2.2 Background Estimate

General background reduction

Non-ep background events are easy to detect by the missing transverse hadronic [2] energy $E_{T,miss}$ and their longitudinal hadronic energy $E - P_Z$.
$E_{T,miss}$ and $E - P_Z$ are defined as:

$$E_{T,miss} = \sqrt{P_X^2 + P_Y^2} \tag{3.1}$$

$$E - P_Z = \sum_i E_i - P_{Z,i} \ . \tag{3.2}$$

The 4-vector of the hadronic final state is $P_X = \sum_i p_{x,i}$, $P_Y = \sum_i p_{y,i}$, $P_Z = \sum_i p_{z,i}$ and $E = \sum_i E_i$. The components are summed over all HFS objects i. The distributions are pictured in Figure 3.5. The data are shown as points and the error bars denote the statistical errors. The data are compared to the PYTHIA and HERWIG photoproduction , the DJANGO/ARIADNE and RAPGAP neutral current DIS (NC DIS) and to a charged current DJANGO prediction (DJANGO CC). As can be seen

[2] Here $E_{T,miss}$ and $E - P_Z$ are calculated with the hadronic energy and not with the total energy of the event. Since in untagged photoproduction the scattered electron is usually undetected, it is not used for the definition of these observables.

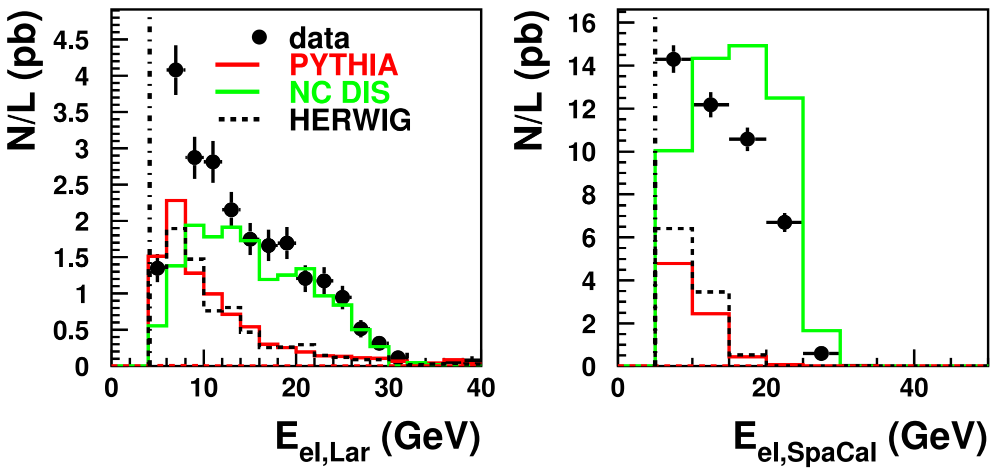

Figure 3.6: *Luminosity normalized distributions of the energy of electrons found in the LAr calorimeter, E_{LAr}, (lefthand figure) and (righthand figure), E_{SpaCal}. The jet selection criteria and the cuts in y_{JB} and $E_{T,miss}$ are required. The vertical dash dotted line refers to the cuts discussed in the text.*

from the left figure the data is not described by the models for $E_{T,miss} > 20$ GeV. At these high values of $E_{T,miss}$ the data are dominated by non-*ep* scattering events, such as beam halo events and muons of cosmic radiation. About 80 % of the data events with $E_{T,miss} > 20$ GeV are identified as background by the QBGFMAR background finders[80]. The QBGFMAR background finders are described later in this section.

The righthand figure shows the $E-P_Z$ distribution. Whereas photoproduction events have mainly values of small $E-P_Z$, NC events arise in this Figure from two sources. The first source are NC events where an electron has been found by the QESCAT electron finder. In these events the electron does not belong to the hadronic final state and $E-P_Z$ is thus smaller than 55.2 GeV. The second source are NC events where no electron has been identified by the QESCAT electron finder. These events are forced to have values of $E-P_Z$ close to 55.2 GeV, which is twice the beam energy. A cut in $E-P_Z$ removes the main fraction of these events. Since $y_{JB} = (E-P_Z)/(2E_e)$ the cuts in $E-P_Z$ at $0.1 * 2E_e$ and $0.9 * 2E_e$ define in addition the phase space of the measured cross sections [79]. The electron beam energy is E_e. The y_{JB} range is thus restricted to the phase space range $0.1 < y_{JB} < 0.9$ already discussed in chapter 1.

Neutral current DIS background

To study the contributions from NC DIS events there was no veto for electrons in the preselection.

Figure 3.6 shows the energy of the electrons found by QESCAT in the LAr calorimeter or in the SpaCal. In events with high Q^2 the electron scatters in the LAr calorimeter. The electron energy spectrum is modelled for these events by the sum of the NC DIS Monte Carlo and the photoproduction models. Electron candidates found with energies $E_{el} < 10$ GeV are often due to forward pions which have been misidentified as electrons. To further remove the high Q^2 background, events with electrons found in the LAr calorimeter with $E_{el} > 5$ GeV have been removed. In addition all events with an electron found by QESCAT in the SpaCal and fulfilling $E_{el} > 5$ GeV have been removed (anti tag). The acceptance of the SpaCal and the LAr thus defines the upper Q^2 bound to $Q^2 \approx 1\mathrm{GeV}^2$.

Nevertheless the most significant background in the data arises still from DIS events. The QESCAT electron finder has a good but not 100% efficiency. Often electrons close to jets are not found as electrons. These electrons do not fulfil an isolation criteria.

If an electron is not found it may fake a high transverse momentum jet or it could be part of a high transverse momentum jet. Because the electron is then included in the hadronic system, these background is explicitly important for multi-jet events with high transverse masses. Therefore jet criteria have been developed to distinguish between photoproduction events and events caused by electrons faking jets. Events caused by electrons faking jets have been removed if at least one of the following criteria are met:

- The invariant mass of a single jet is defined as:

$$\mathsf{jet\ mass} = \sqrt{(\sum_j p_j)^2} \quad . \tag{3.3}$$

  The sum runs over all objects j which belong to the jet and p_j is the 4-momentum of the object. This is not equal to the invariant mass calculated with the jet 4-vector. Electrons faking jets often have a very low jet mass which is unusual for hadronic jets, as shown in Figure 3.7b. Events are rejected if one of the leading jets has a jet mass < 2 GeV.

- Figure 3.7a shows the fraction of the jet energy which is attributed to the electromagnetic section of the LAr calorimeter, jet EM fraction.

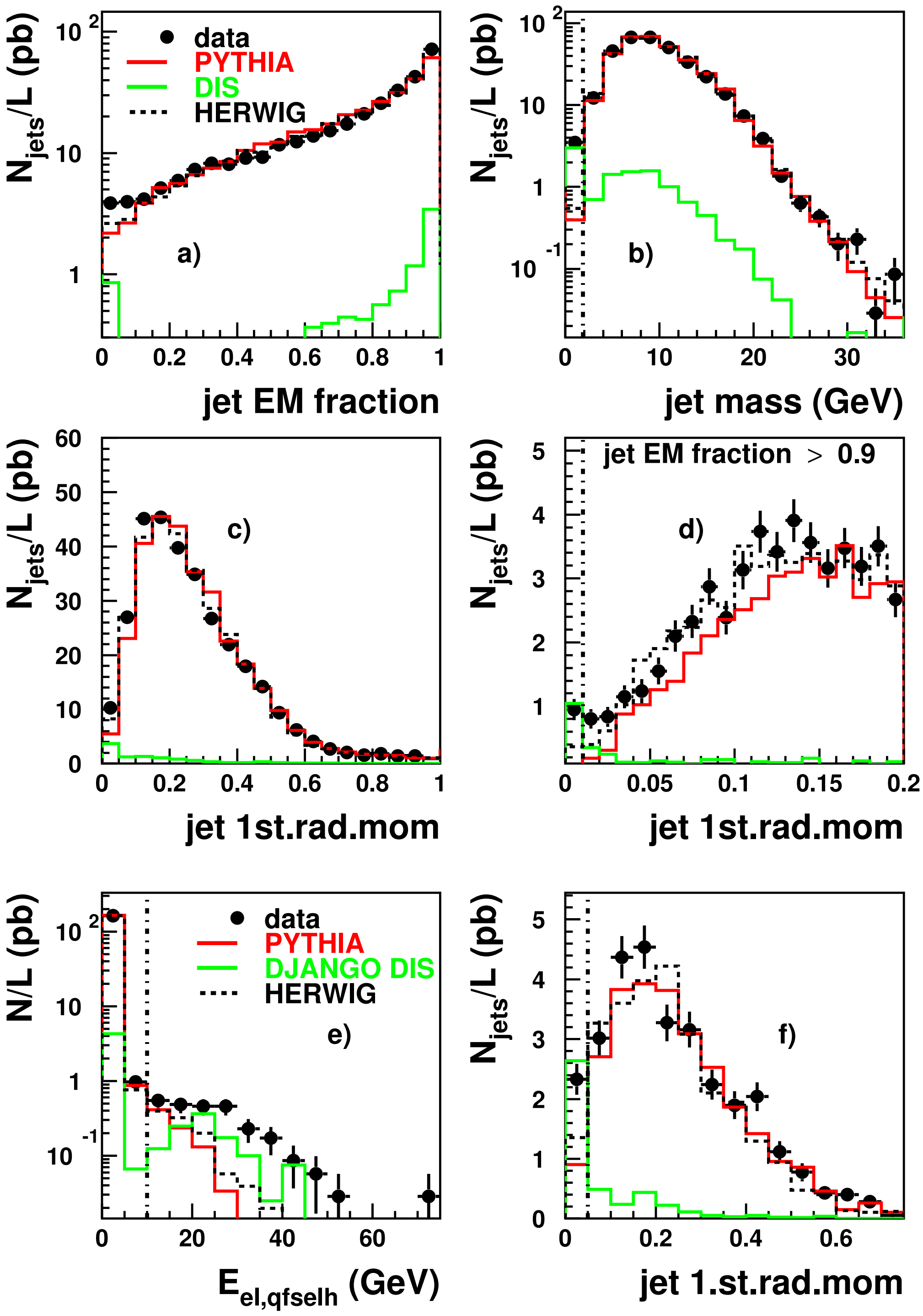

Figure 3.7: *Luminosity normalized distributions of the jet electromagnetic fraction (Figure a), the jet mass (Figure b) and the jet 1st. radial moment (Figure c). Figure d shows the jet 1st. radial moment distribution for jets with an electromagnetic fraction > 0.9. The energy distribution for electrons found with the QFSELH electron finder is shown in Figure e. Figure f shows the jet 1st. radial moment for jets pointing into a crack of the LAr calorimeter.*

The first radial moment of a jet can be used to measure the jet collimation and the radiation within a jet [81]. It is defined as:

$$\text{jet 1st.rad.mom.} = \frac{\sum_j E_{T,j} R_{j,\text{jet}}}{\sum_j E_{T,j}} \quad . \tag{3.4}$$

The distance in the $\eta\phi$-plane between the object j of the jet and the jet axis is $R_{j,\text{jet}}$. Electrons faking jets are more collimated than true hadronic jets, which can be seen in Figure 3.7c. Figure 3.7d shows the distribution of the jet 1st.rad.mom. for jets with an jet EM fraction > 0.9. Events are rejected if one of the two leading jets has a jet EM fraction > 0.9 and jet 1st.rad.mom. < 0.01.

- A second electron finding algorithm (QFSELH) has been used to identify electrons [82]. These electron candidates are not discarded from the list of HFS objects and may also be part of a jet. The electron energy is shown in Figure 3.7e. Events are rejected if the electron energy $E_{\text{el,qfselh}}$ is greater than 10 GeV.

- If the jet axis of one of the leading jets points into a ϕ-crack of the LAr calorimeter the event is rejected if the jet 1st.rad.mom. < 0.05. The cracks considered are the following regions in ϕ: $43° - 47°$, $88° - 92°$, $133° - 137°$, $178° - 182°$, $223° - 227°$, $313° - 317°$, $358° - 2°$. Electrons scattered into these regions often fake jets as can be seen in Figure 3.7f. For jet 1st.rad.mom. < 0.05 the data is described by the prediction of the NC DIS Monte Carlo generators.

These requirements reduce the DIS background to less than 1 % for the total sample and to at most 5 % for all phase space regions relevant for the dijet analysis and to at most 10 % for the 3-jet analysis.

Non *ep*-background finders

In Figure 3.8 the luminosity normalized number of events which have been identified as background by the QBGFMAR finder as a function of the bit-number corresponding to the finder is pictured. All the latter selection criteria are required. The QBGFMAR package is designed to tag non-collision background using a set of background finders. The finders shown in Figure 3.8 are designed to work with most physics channels. All finders identify PYTHIA and HERWIG events as background, except finder 6. This finder searches for two opposite muon tracks. All events found by this finder have been viewed by eye and have been found to be overlaid by cosmic muons. After rejecting all events found by this finder, also the number of events identified as background by the finders 5 and 7 are almost compatible with the PYTHIA and HERWIG predictions. There may be still non *ep*-background in the data sample. However the remaining

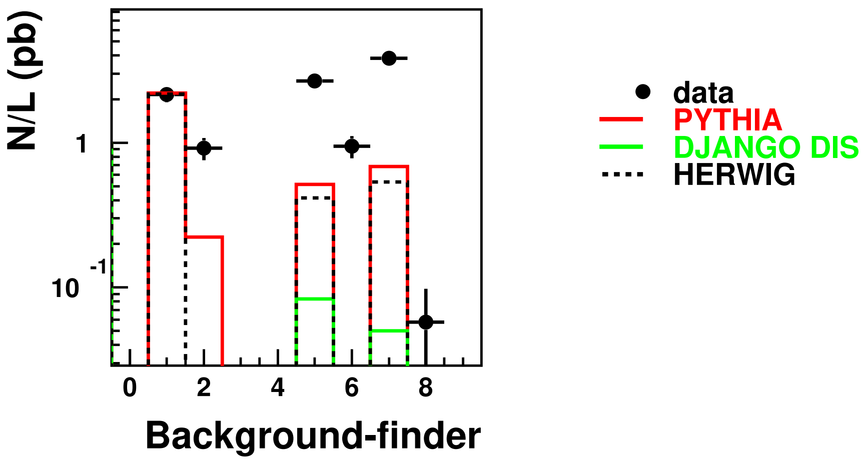

Figure 3.8: *QBGFMAR background finders: Shown are the luminosity normalized number of events which have been identified as background by a QBGFMAR finder as a function of the bit-number of the finder.*

difference of the number of events identified as background in the data and in the PYTHIA or HERWIG event sample is about 0.5 percent of the total number of selected events.
Phase space regions with small event numbers, such as high invariant masses, high x_P, etc. have been scanned by eye. Only three background events are found and removed from the event sample.

3.2.3 Final Cut Definition

In this section the final selection criteria are presented. In addition to the criteria already provided in the last sections, the pseudorapidity of each jet η_{jet} is restricted to $-0.5 < \eta_{jet} < 2.5$. Figure 3.9 shows the luminosity normalized number of jets as a function of η_{jet} without this restriction. Even for very high and very low values of η_{jet} the data is described by the PYTHIA and HERWIG predictions. However there are various experimental reasons to restrict the pseudorapidity range. First the jets have to be well contained in the LAr calorimeter, which has a pseudorapidity range of $-1.47 < \eta < 3.35$. Second the jet energy calibration is not well described by the Monte Carlo predictions for $\eta_{jet} > 2.5$. A third reason is the still high NC DIS background at very low η_{jet} values.
The full set of selection criteria is summarised in table 3.1. The measured Q^2 region is $Q^2 < 1\,\mathrm{GeV}^2$, as given by the acceptance for electrons in the LAr and Spacal. The

Good, medium runs, LAr, full CJC and SPACAL HV on.
Subtrigger: S64, S67, S75 and S77
$-36 < z_{vtx} < 34$ cm $E_{T,miss} < 20$ GeV QBGFMAR background finder bit number 6 not fired.
QESCAT electrons must have $E_{el} < 5$ GeV. QFSELH electrons must have $E_{\mathrm{el,qfselh}} < 10$ GeV.
jet mass > 2 GeV. Not (jet EM fraction > 0.9 and jet1st.rad.mom. < 0.01). Not (jet in phi crack and jet 1st.rad.mom. < 0.05). $E_{T,max} > 25$ GeV $E_{T,second} > 15$ GeV
3-jet sample: $E_{T,third} > 10$ GeV
$-0.5 < \eta_{jet} < 2.5$
$0.1 < y_{JB} < 0.9$

Table 3.1: *The final selection criteria. The subtriggers are discussed in section 3.2.4.*

kinematic range of the measured jet cross sections was already presented in section 2.6 in Table 2.1. Applying these cuts and using the final hadronic calibration (presented in section 3.2.5) the total number of events selected was 5265.

3.2.4 Trigger Selection and Efficiency

In order to determine the fraction of events which has been rejected by the H1 trigger system, *analysis subtriggers* have to be found which have fired for most of the selected events. Then the efficiency of these subtriggers has to be determined. The inefficiencies can be accounted for by a properly reweighting of the data. Most of the events are triggered on the basis of high transverse energy deposits in a trigger tower of the LAr calorimeter.

The efficiencies of the *analysis subtriggers* are calculated with events triggered by an independent subtrigger, the so called *monitor trigger*. Note that none of these *analysis subtriggers* are allowed to consist out of trigger elements which are also used in the *monitor trigger*. This means the *monitor trigger* has to be *independent* from the *analysis subtriggers*.

The fraction of events which are triggered by both the *analysis subtrigger*, S, and the *monitor trigger*, M, to the events triggered by the *monitor trigger* gives the efficiency.

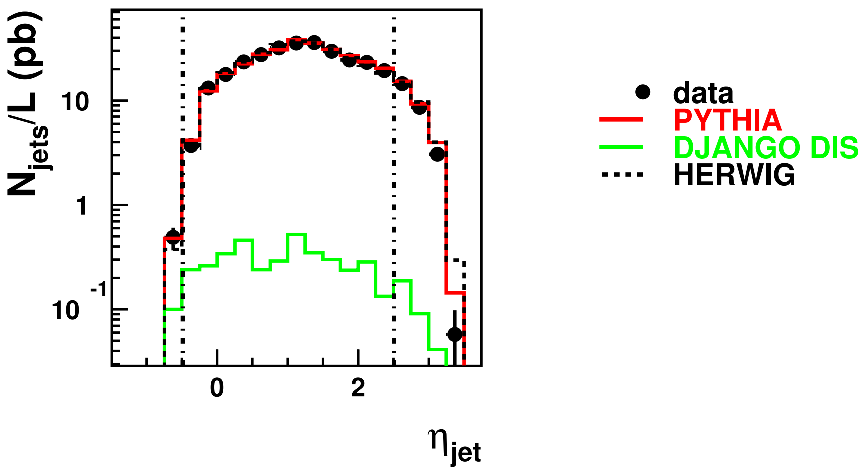

Figure 3.9: *Shown is the luminosity normalized number of jets as a function of η_{jet} for the two leading jets.*

The trigger efficiency of a subtrigger S is thus defined as:

$$\text{Efficiency S} = \frac{\text{number of events triggered by S and M}}{\text{number of events triggered by M}} \quad . \tag{3.5}$$

The chosen analysis subtriggers are S64, S67, S75 and S77. S67 and S75 are based on energy treshholds in electromagnetic and hadronic parts of the LAr calorimeters. Although these triggers are optimised for electrons, they also react on high energetic jets. S64 is based on transverse energy deposits in the LAr calorimeter and S77 on missing energy in the LAr calorimeter. All these triggers also require vertex and timing information.
No monitor trigger is available for high E_T photoproduction, since the monitor trigger has to be independent. Therefore a similar test event sample has to be defined to check the trigger efficiencies. Subtrigger S3 requires only energy in the electromagnetic SpaCal. Events with electrons found in the SpaCal are not rejected for the test event sample used to determine the trigger efficiency. Thus the test sample mainly contains events with an electron identified in the SpaCal and two high E_T jets.
S3 can only be used as monitor trigger under the assumption that the kinematics of the jets in that event sample is similar to the pure photoproduction sample. This is not devious and has been proven in [85].
The efficiency of the various subtriggers and the combined efficiency as a function of the transverse energy of the leading jet is shown in Figure 3.10. The efficiency is calculated with the L1 and L4 trigger elements. Due to conditions on L2 or L4 a

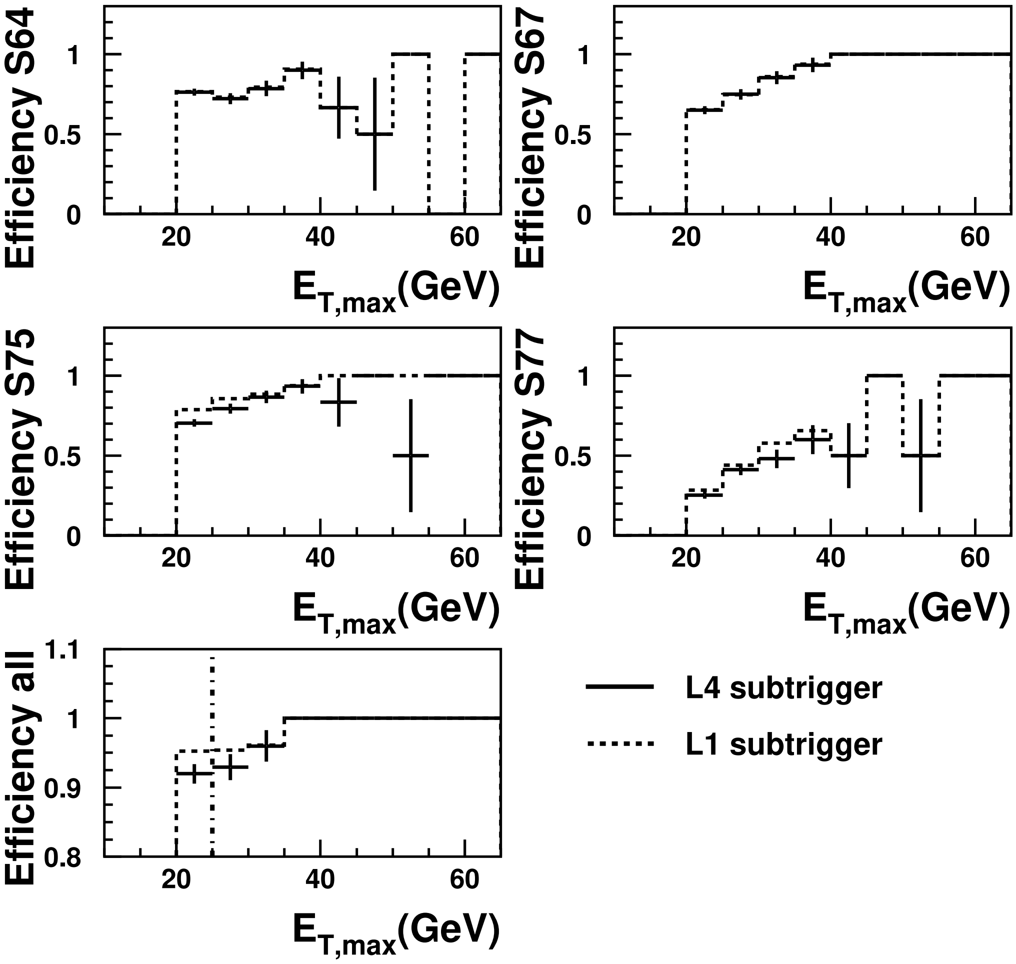

Figure 3.10: *The subtrigger efficiency for the used subtriggers and the combined efficiency as a function of $E_{T,max}$. The errors bars denote the efficiency error. The bins at very high E_T contain only a few events. The vertical dash dotted line refers to the final cut in $E_{T,max}$.*

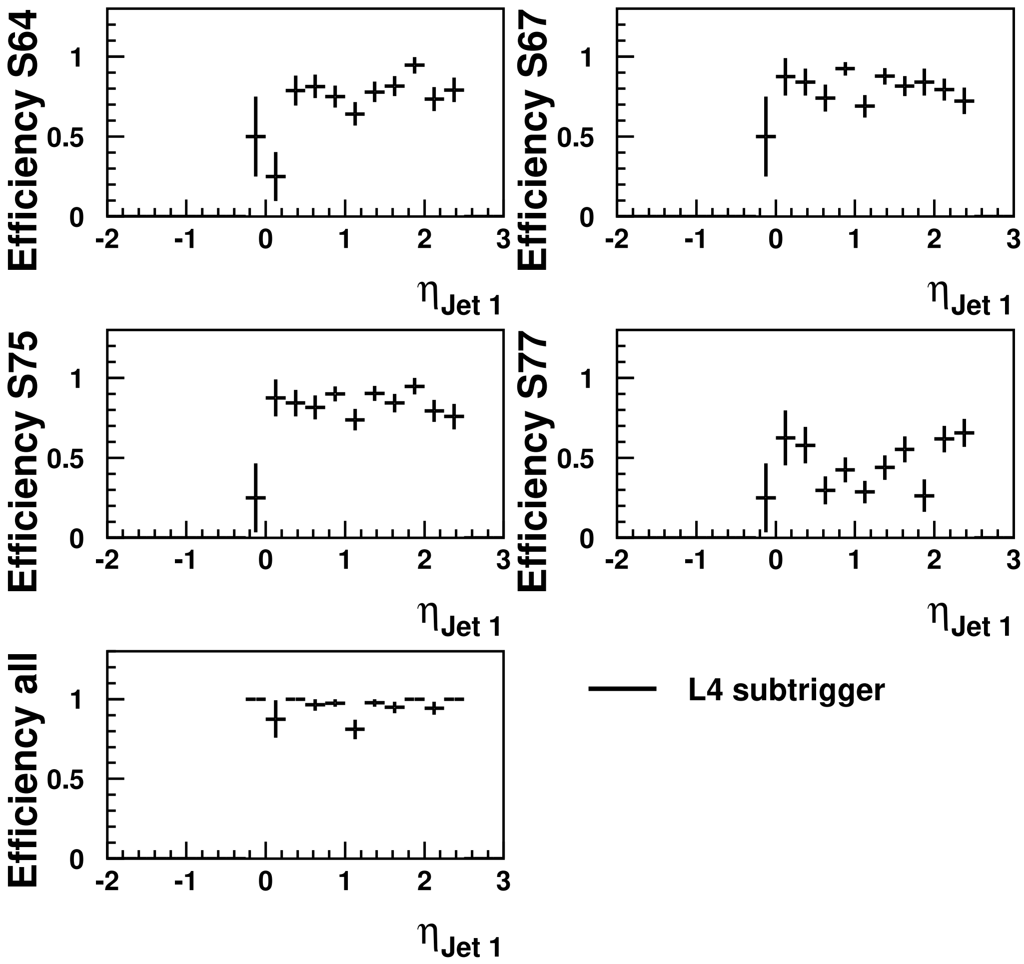

Figure 3.11: *The subtrigger efficiency for the used subtriggers and the combined efficiency as a function of η_{jet1}. The error bars denote the efficiency error.*

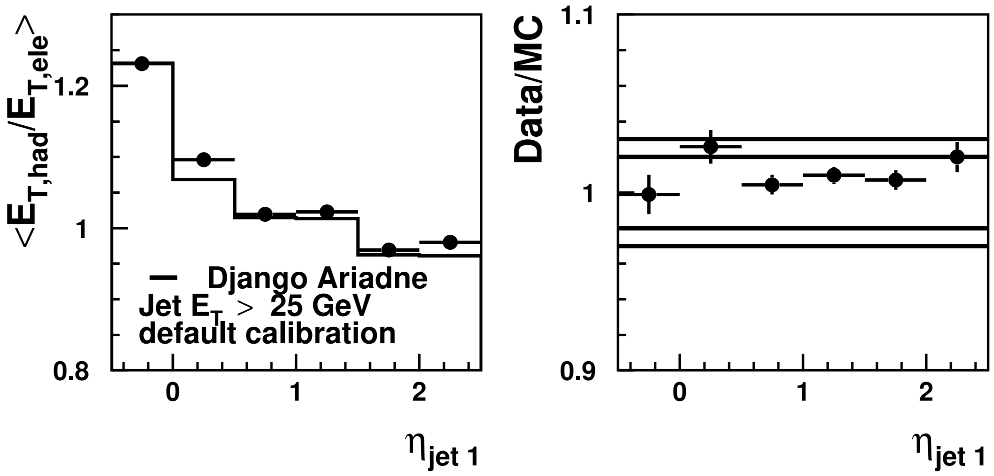

Figure 3.12: *Mean E_T jet-electron balance $< E_{T,had}/E_{T,ele} >$ distribution for the NC data test sample and DJANGO ARIADNE as a function of η_{jet1} for $E_{T,max} > 25$ GeV (lefthand Figure). The righthand Figure shows the ratio of the E_T jet-electron balance of the data to that for the Monte Carlo generator prediction (MC) as a function of η_{jet1}. The default calibration is used. The lines correspond to a ± 2 % and ± 3 % uncertainty. The error bars denote the error of the mean values.*

small fraction of events triggered by the subtriggers S75 and S77 on L1 are rejected by L2 or L4. As expected by the definition of the subtriggers the trigger efficiency increases for increasing transverse energies. All 4 subtriggers are combined to select more events. The trigger efficiency of the used combined set is always higher than 93 % for $E_{T,max} > 25$ GeV. Figure 3.11 shows the efficiency as a function of the pseudorapidity of the leading jet for $E_{T,max} > 25$ GeV. No η dependence is visible for the combined set and the data is therefore $E_{T,max}$ dependent corrected for the trigger inefficiencies.
The trigger efficiencies are above 94 % for the total event sample described in this analysis.

3.2.5 Hadronic Final State Calibration

The algorithm to define the hadronic final state was already discussed in section 3.2.1. The measurement can be further improved by a recalibration of the jet transverse energies dependent on the calorimeter wheel and the jet transverse energy. After the recalibration of the jet transverse energies kinematic quantities, such as y, are recalculated with the new hadronic final state 4-momenta.
The calibration constants are taken from [86] in order to check if the calibration

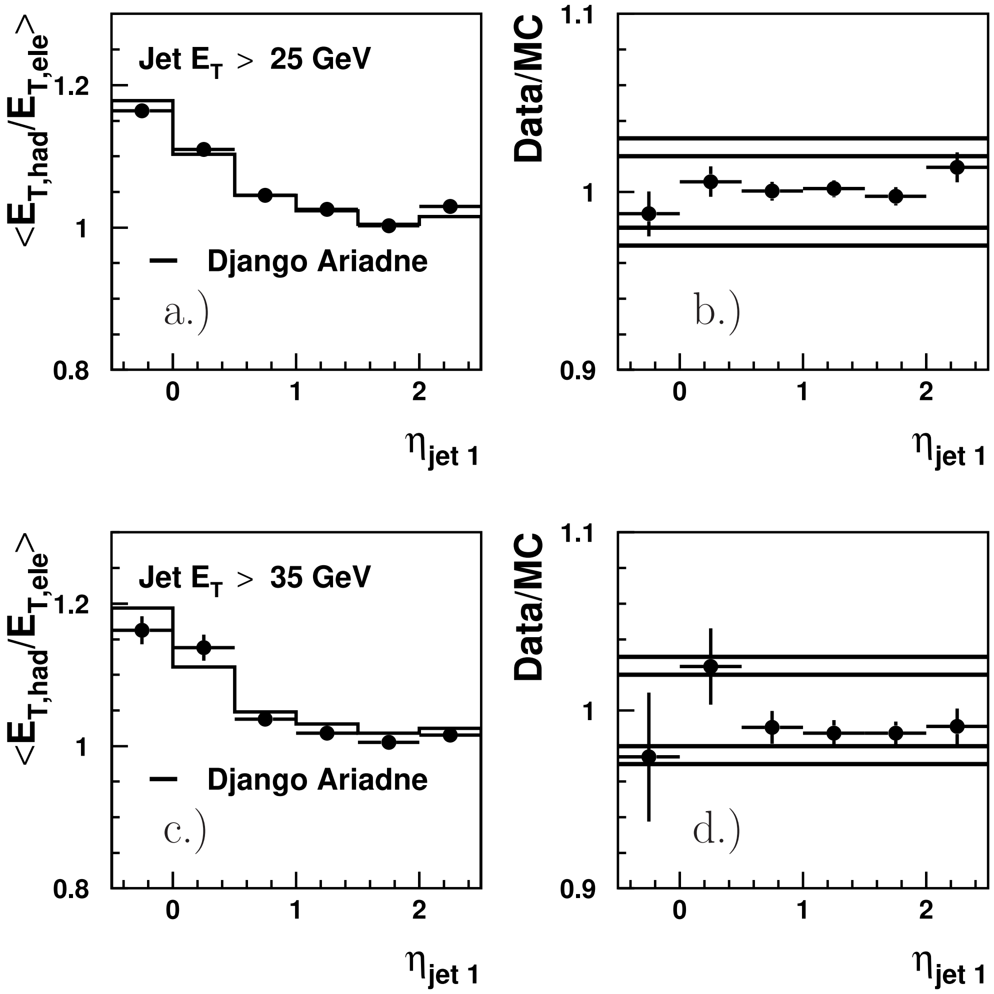

Figure 3.13: *Mean E_T jet-electron balance $< E_{T,had}/E_{T,ele} >$ distribution for the NC data test sample and DJANGO ARIADNE as a function of η_{jet1} for $E_{T,max} > 25$ GeV (a) and $E_{T,max} > 35$ GeV (c) and using the final calibration. Figure (b) shows the ratio of the E_T jet-electron balance of the data to that for the Monte Carlo generator prediction (MC) as a function of η_{jet1} for $E_{T,max} > 25$ GeV and Figure (d) for $E_{T,max} > 35$ GeV. The lines correspond to a ± 2 % and ± 3 % uncertainty. The error bars denote the error of the mean values.*

developed for the measurement of charged and neutral current cross sections can also be used for jets with high transverse energy.
The calibration is based on the comparison of the transverse energy balance between electrons and the complete hadronic system. It was found in [86] that after the recalibration of the data and Monte Carlo events, the transverse energy balance was described by the simulation within 2 %.

1997 preselection
Good, Medium runs, LAr, full CJC and SPACAL HV on
$-36 < z_{vtx} < 34$ cm
QESCAT electron found in LAr outside phi crack. $E_{el} > 11$ GeV $E_{T,el} > 15$ GeV $40^o < \theta_{el} < 145^o$
$0.1 < y_{el} < 0.9$ $Q^2_{el} > 120$ GeV^2
$E_{T,max} > 25$ GeV no second jet with $E_T > 5$ GeV

Table 3.2: *The selection criteria for the neutral current DIS event sample.*

To check how well the transverse energy balance is described by the simulation for events with high transverse momentum jets a neutral current *high* Q^2 test sample has been selected. The events are taken from the preselection of [87] and the criteria shown in table 3.2 are demanded. The transverse momentum of the electrons is precisely calibrated and described by the simulation for this sample within $\pm 1\%$, as described in [88]. Therefore the electron can be used to check the hadronic calibration.
Figure 3.12 shows the E_T jet-electron balance, $< E_{T,had}/E_{T,ele} >$, for data and DJANGO ARIADNE as a function of η_{jet1} for $E_{T,max} > 25$ GeV. The default calibration was used. The E_T balance $< E_{T,had}/E_{T,ele} >$ is defined as the mean value of the $E_{T,had}/E_{T,ele}$ distribution. Even without applying any recalibration the E_T balance is described within ± 2 %.
Figure 3.13a shows the same distribution with the final calibration applied.
It can be seen that both the description by the model is slightly improved and the $< E_{T,had}/E_{T,ele} >$ values are closer to 1.
The recalibration also shifts the measured E_T of the jets and the measured invariant masses closer to the generated values. This will be discussed in section 3.5.1.
Essential for this analysis is the description of the jet calibration by the simulation

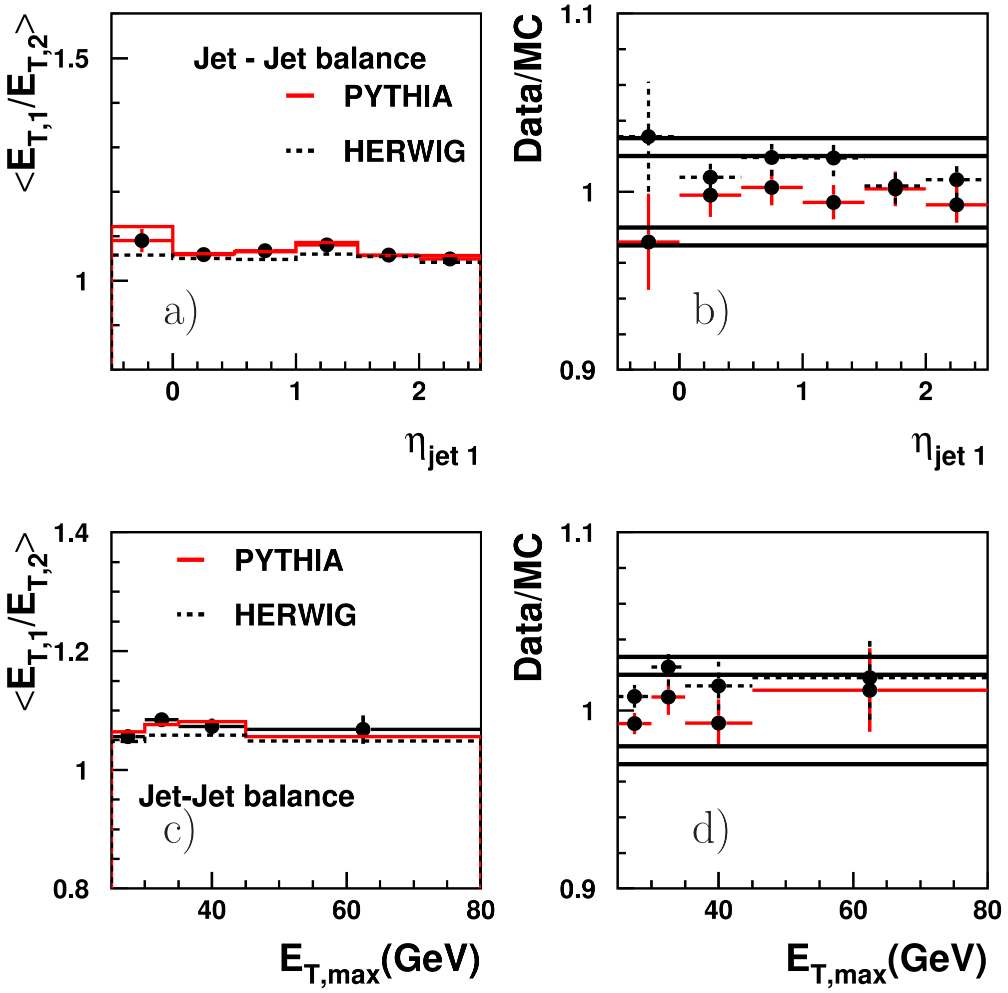

Figure 3.14: *Mean E_T jet-jet balance distribution for data, PYTHIA and HERWIG as a function of $E_{T,max}$ (a) and as a function of η_{jet1} (c). Figure (b) shows the ratio of the E_T jet-jet balance of the data to the Monte Carlo generator prediction (MC) as a function of $E_{T,max}$ and Figure (d) as a function of of η_{jet1}. The final calibration is used. The lines correspond to a ± 2 % and ± 3 % uncertainty. The error bars denote the error of the mean values.*

for jet events in photoproduction.

Figure 3.14a shows the E_T jet-jet balance $< E_{T,1}/E_{T,2} >$ for the photoproduction dijet sample as a function of the pseudorapidity of the leading jet η_{jet1}. To reduce the effect that the leading jet has a larger transverse energy than the second jet, the jets are numbered such that jet 1 is the jet with the larger ϕ value. The numbering of the jets is therefore independent on η and E_T. This Figure, Figure 3.14b and the following Figures demonstrate that the data is described by the simulation in all regions of the detector. This justifies a systematic uncertainty of the relative hadronic energy scale in the LAr calorimeter of 2 %.

Figure 3.15 shows as a further confirmation the jet-jet balance as a function of η_{jet1} for events dominated by direct processes ($x_\gamma > 0.8$) and for events dominated by resolved processes ($x_\gamma < 0.8$). Both regions are also described by the simulation within the quoted uncertainties.

The dependence of the calibration on energy not contained in the leading jet is tested in Figure 3.16 by exploiting the balance of the leading jet and the hadronic rest. The hadronic rest is defined as all hadronic energy which does not belong to the leading jet; it is thus also sensitive to energy deposits which are not part of a jet with high transverse energy. The jet-rest balance $< E_{T,max}/E_{T,Rest} >$ as a function of $E_{T,max}$ and η_{jet1} is found to be again well described within the uncertainties.

Both Monte Carlo models, representing different hadronic final states, are able to reproduce the tested features of the hadronic final state.

A further quality check of the hadronic final state reconstruction is the description of the relative difference between y once measured with the electron and once with the hadronic final state. Agreement between data and simulation was found in [88] for inclusive NC events. Figure 3.17 illustrates this for a NC dijet sample sample. This sample is similar to the one defined in table 3.2, but requiring instead, two jets with the same E_T cuts as in the photoproduction sample.

Figure 3.18 illustrates the relative difference of y reconstructed from the hadronic final state y_{JB} and y reconstructed from the electron found in the electron tagger. In addition to the photoproduction selection criteria an electron has to be found in the electron tagger with $0.3 < y_{el} < 0.7$ and $Q^2_{el} < 0.001\,\mathrm{GeV}^2$. As well no energy deposits should be found in the photon tagger. Both y measurements agree within 2 %.

In summary we observe that the hadronic energy scale uncertainty for dijet events with high transverse energy in photoproduction is ± 2 %. A variation of the hadronic energy scale of ± 2 % will be used as systematic error.

Figure 3.19 shows the jet-rest balance as a function of η_{jet1} for the 3-jet data sample. The hadronic rest consists in these events of the second and third jet and all additional hadronic deposits.

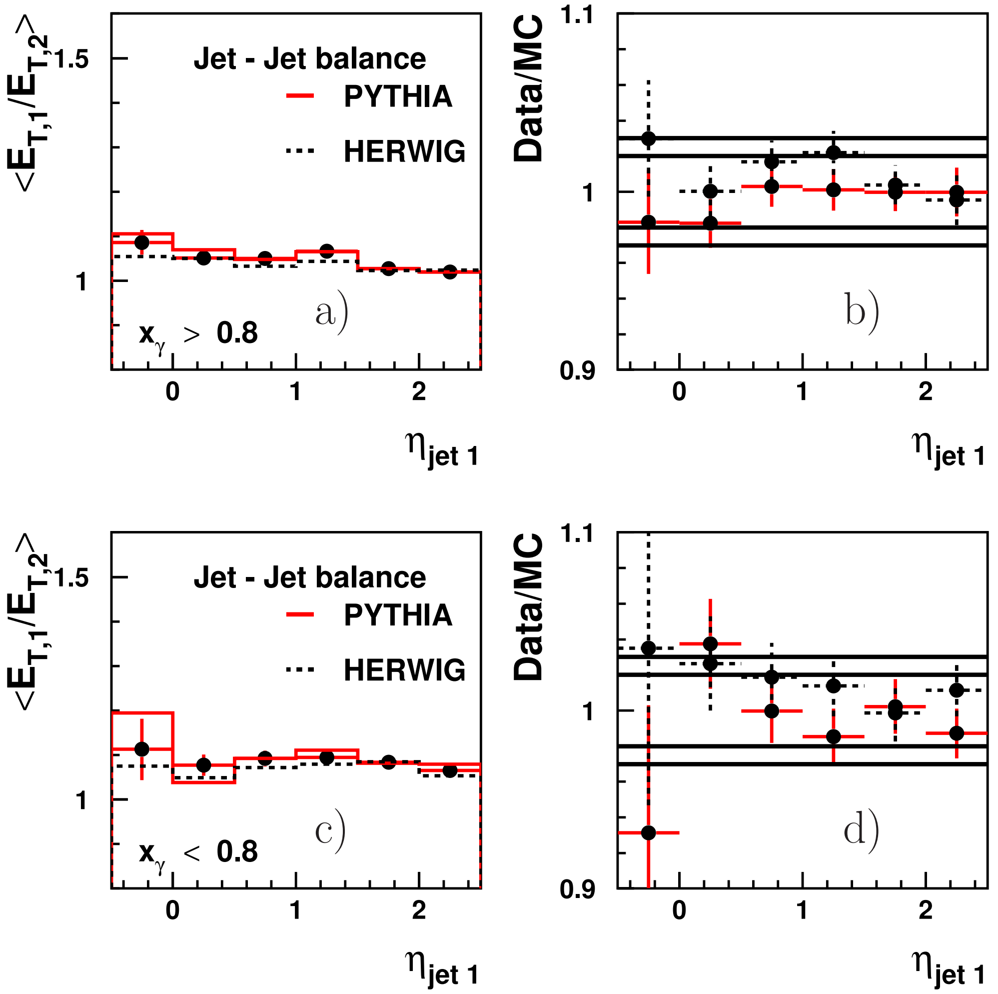

Figure 3.15: *Mean E_T jet-jet balance distribution for data, PYTHIA and HERWIG as a function of η_{jet1} for $x_\gamma > 0.8$ (a) and for $x_\gamma < 0.8$ (c). Figure (b) shows the ratio of the E_T jet-jet balance of the data to the Monte Carlo generator prediction (MC) as a function of η_{jet1} for $x_\gamma < 0.8$ and Figure (d) for $x_\gamma > 0.8$. The final calibration is used. The lines correspond to a ± 2 % and ± 3 % uncertainty. The error bars denote the error of the mean values.*

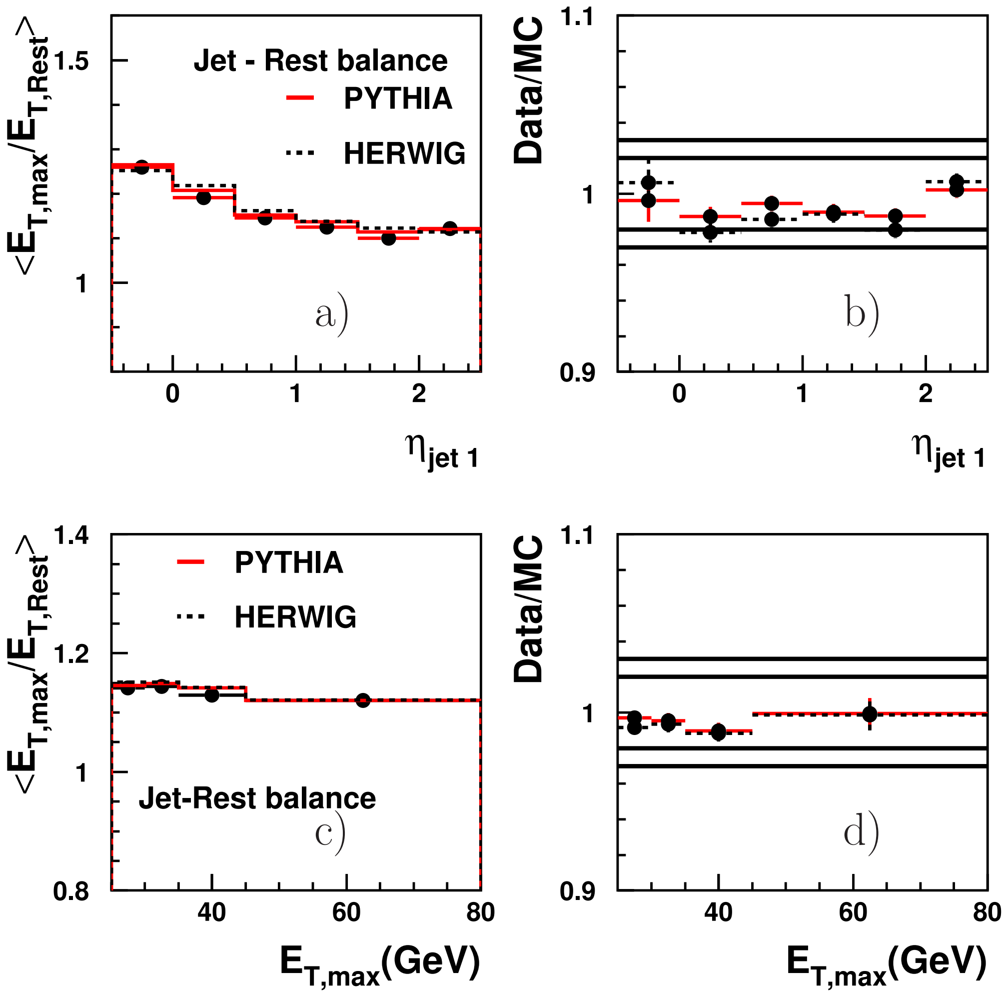

Figure 3.16: *Mean E_T jet-rest balance distribution for data, PYTHIA and HERWIG as a function of $E_{T,max}$ (a) and as a function of η_{jet1} (c). Figure (b) shows the ratio of the E_T jet-rest balance of the data to the Monte Carlo generator prediction (MC) as a function of $E_{T,max}$ and Figure (d) as a function of of η_{jet1}. The final calibration is used. The lines correspond to a ± 2 % and ± 3 % uncertainty. The error bars denote the error of the mean values.*

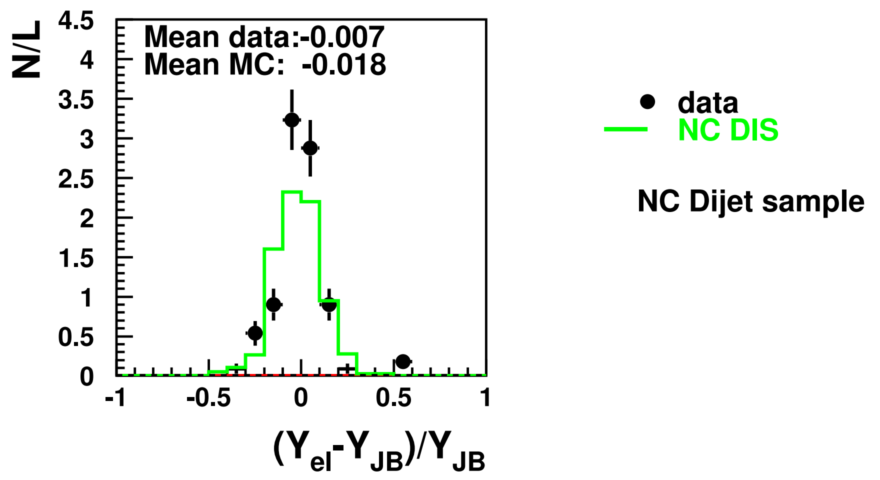

Figure 3.17: *Distribution of the relative difference of y_{JB} and y_{el} measured with the electron found in the LAr calorimeter.*

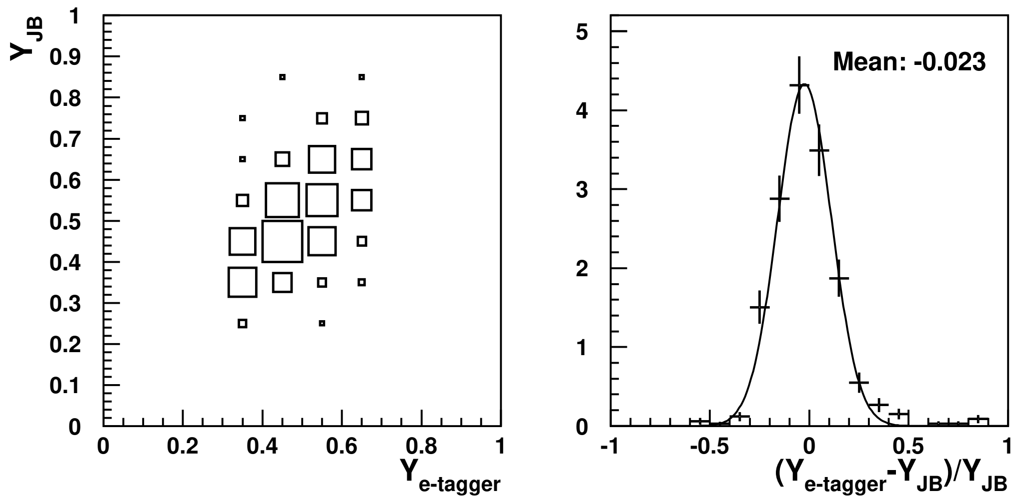

Figure 3.18: *Correlations of y_{JB} and y_{el} measured with the electron found in the electron tagger (left) and the distribution of the relative difference of y_{JB} and y_{el} (right).*

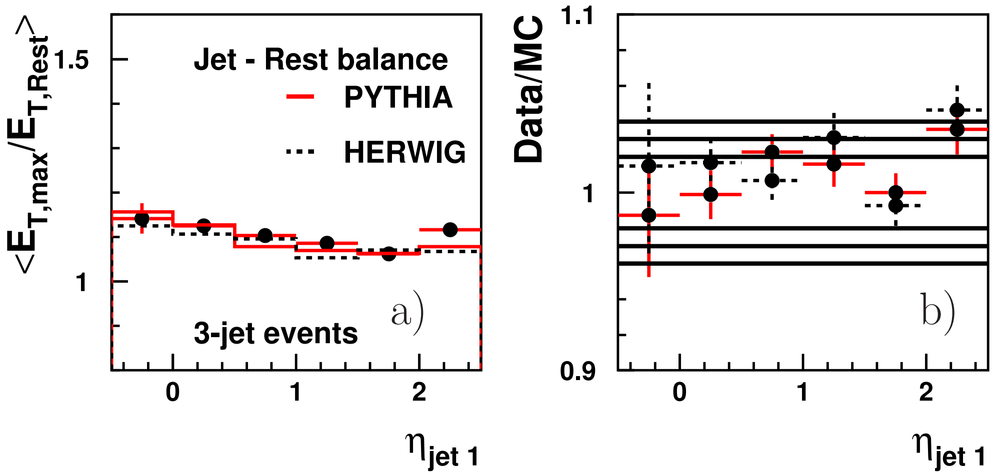

Figure 3.19: *E_T jet-rest balance distribution for data, PYTHIA and HERWIG as a function of η_{jet1} (a). Figure (b) shows the ratio of the E_T jet-rest balance of the data to the Monte Carlo generator prediction (MC). The lines correspond to a ± 2 %, ± 3 % and ± 4 % uncertainty.*

Even for the 3-jet events the PYTHIA and HERWIG description of the data is accurate within ± 2 %.

3.2.6 Event Selection Stability

Displayed in Figure 3.20 is the number of selected events per unit luminosity as a function of the accumulated luminosity. The selection is stable over the entire data taking period. This is shown separately for each year. As required for stable data taking conditions a almost identical event rate is measured.

3.3 Jet Observables and Control Measurements

In this section the properties of the selected dijet and 3-jet events are studied and compared to the HERWIG and PYTHIA predictions. Emphasis is placed on the jet variables which characterize the jet system.

3.3.1 The dijet sample

Since the distributions of most not jet related kinematic variables look similar for the dijet and 3-jet sample they are only discussed for the high statistics dijet sample. Event kinematic observables which are not calculated from jets are presented in Figure

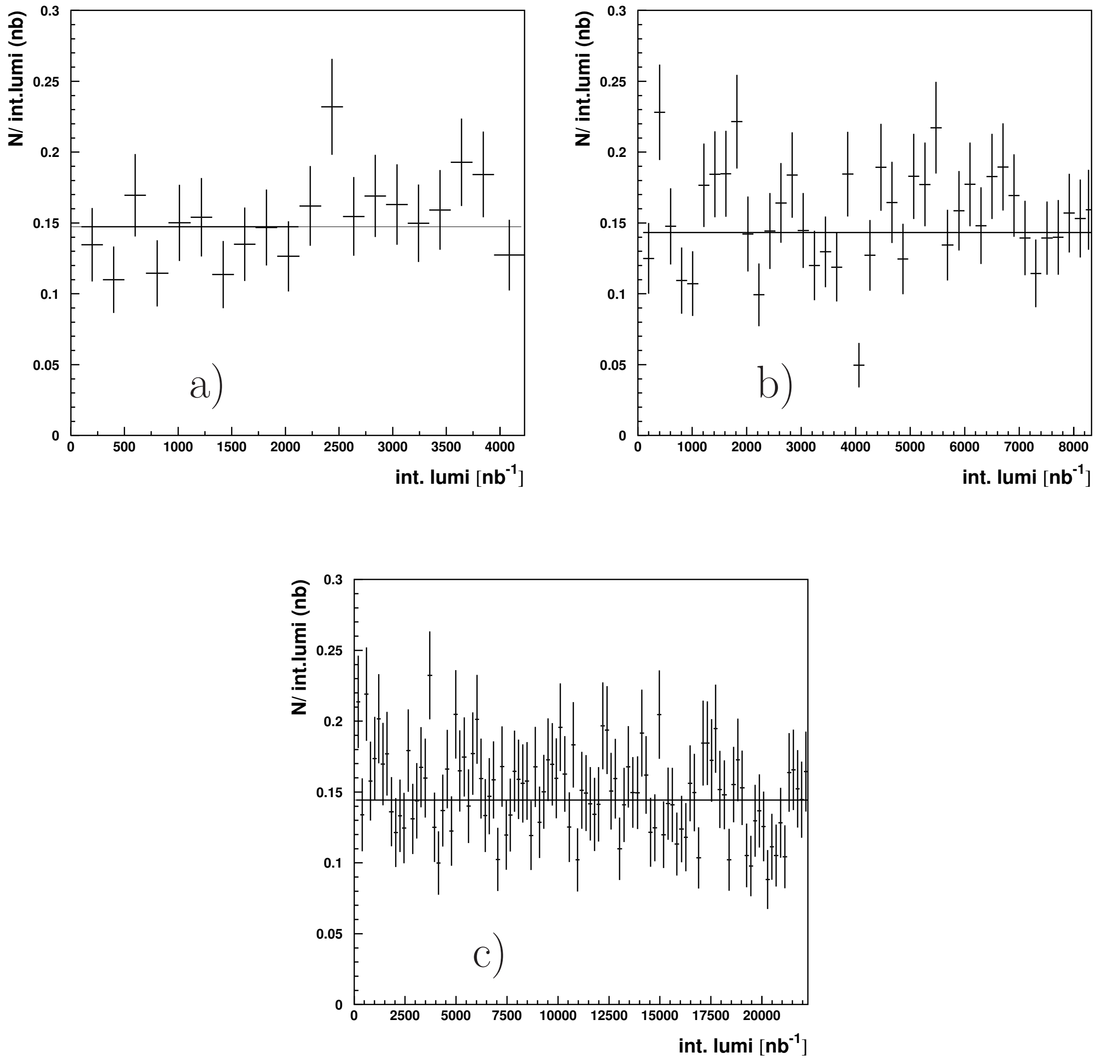

Figure 3.20: *The number of accumulated events per unit luminosity (in* 200 nb*) as a function of the accumulated luminosity for the 1995 (a), 1996 (b) and 1997 (c) data samples. The lines correspond to a linear fit.*

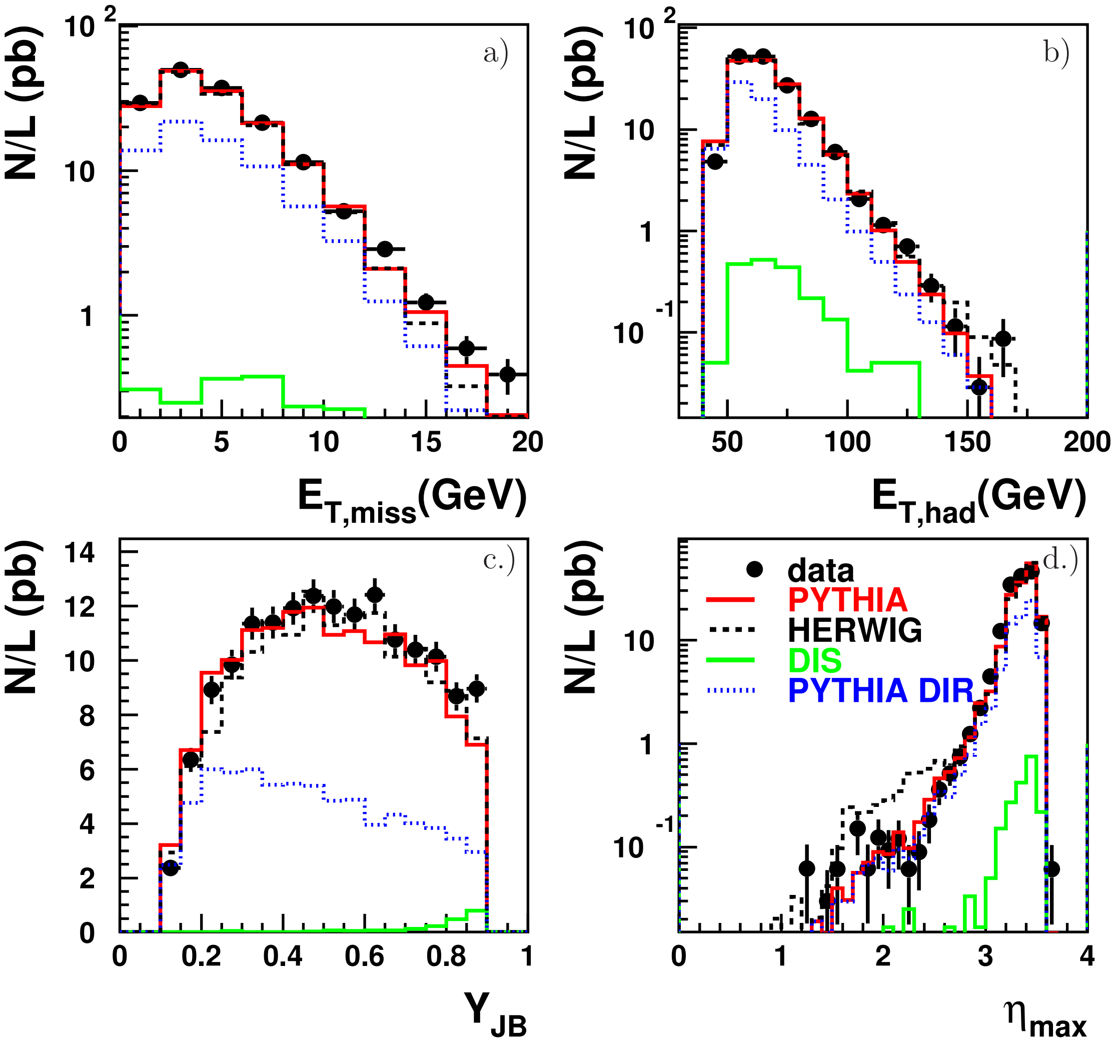

Figure 3.21: *Comparison of the dijet data with HERWIG and PYTHIA. Shown are luminosity normalized distributions of $E_{T,miss}$ a), $E_{T,had}$ b), y_{JB} c) and η_{max} d).*

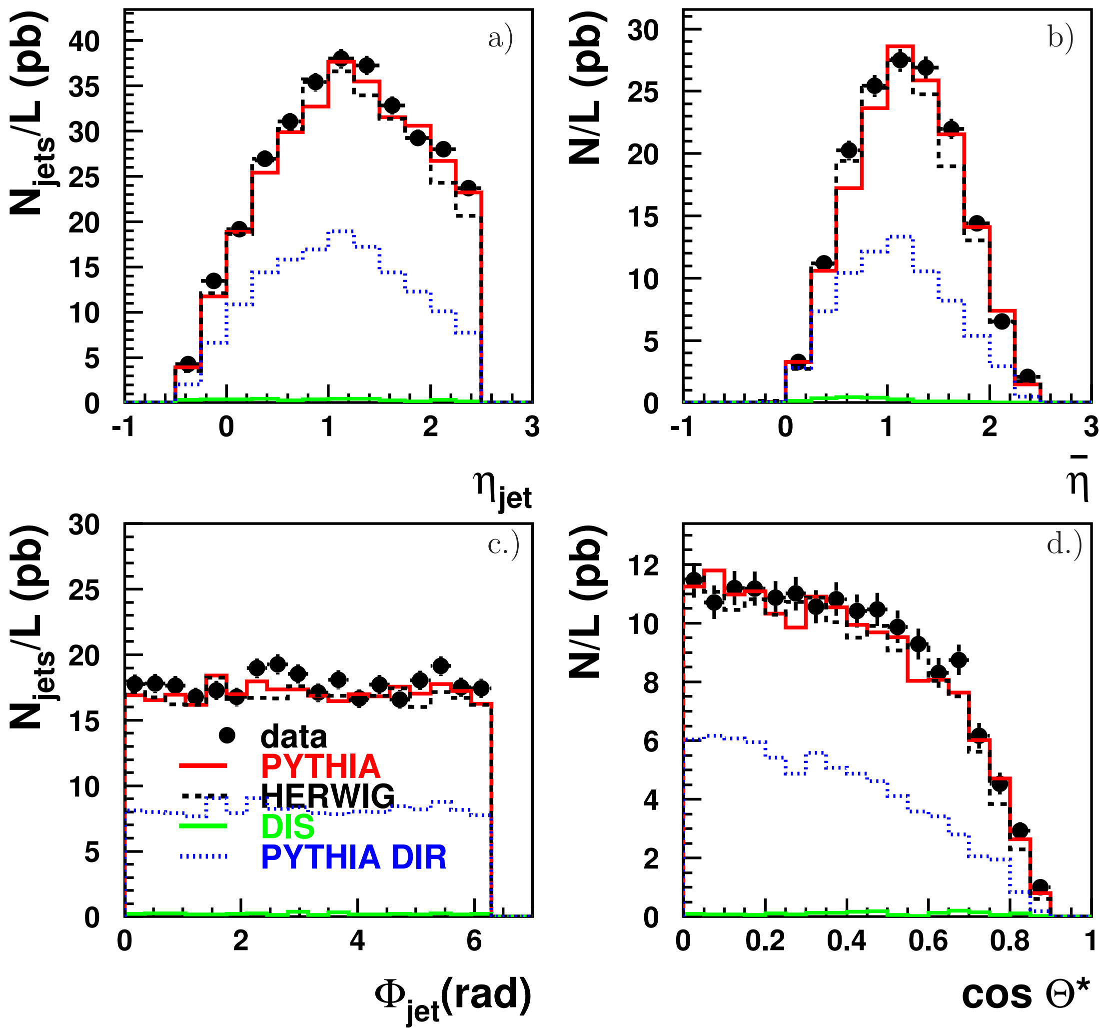

Figure 3.22: *Comparison of the dijet data with HERWIG and PYTHIA. Shown are luminosity normalized distributions of η_{jet} a), $\overline{\eta}$ b), ϕ_{jet} c) and $\cos\theta^*$ d).*

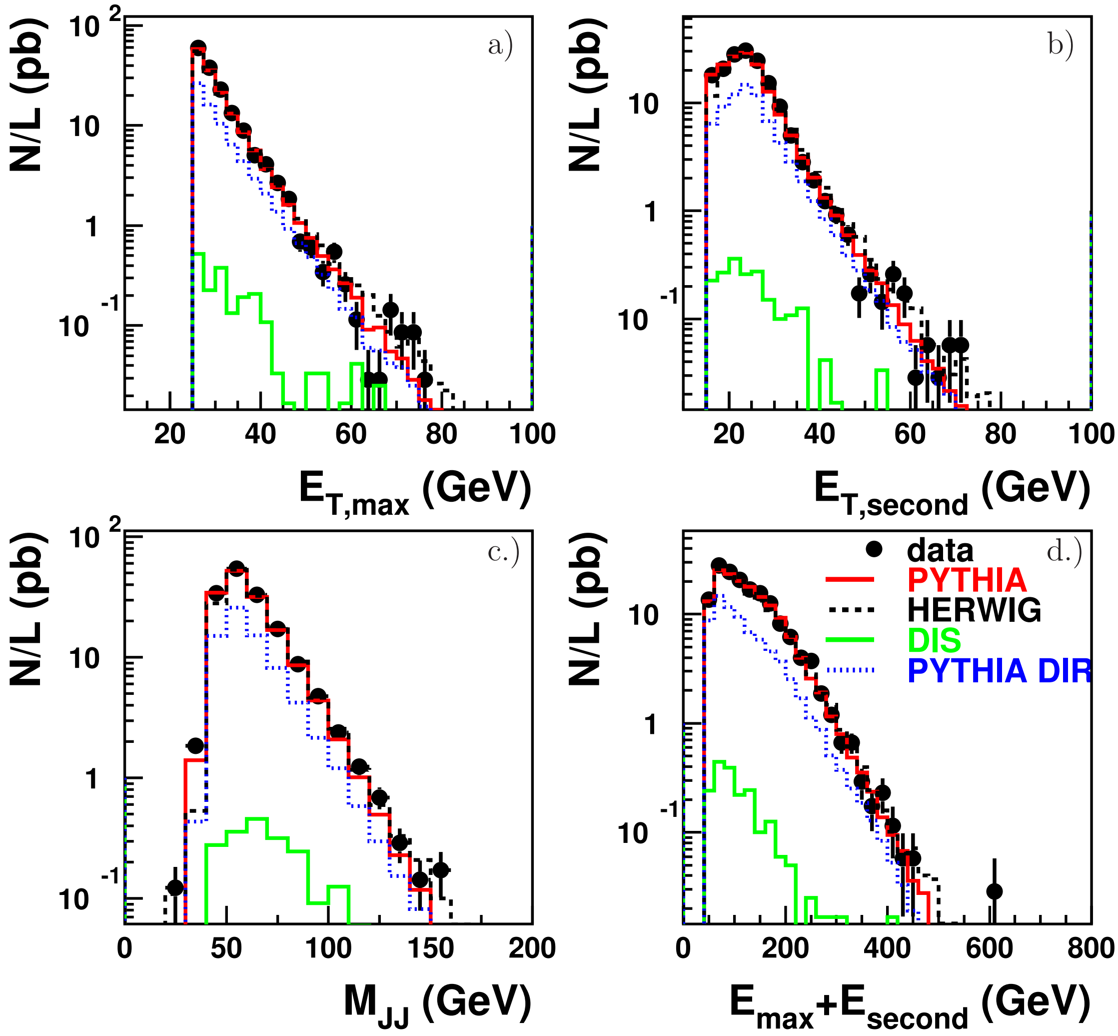

Figure 3.23: *Comparison of the dijet data with HERWIG and PYTHIA. Shown are luminosity normalized distributions of $E_{T,max}$ a), $E_{T,second}$ b), M_{JJ} c) and $E_{max} + E_{second}$ d).*

3.21. The $E_{T,miss}$ distribution shows small deviations from the predictions only at $E_{T,miss} > 12$ GeV. The distribution of $E_{T,had}$, the total hadronic transverse energy in the event, lies between 40 GeV and 170 GeV. HERWIG predicts more events at high $E_{T,had}$, but both models are able to describe the data.

Figure c) is the y_{JB} distribution. Both models give an adequate description of the data. The low y region is dominated by direct events. As can be seen in the Figure the remaining NC DIS background is visible only at high y.

For each event the quantity η_{max} is defined as the pseudorapidity of the most forward HFS object with energy > 400 MeV. This quantity is usually used to select diffractive events, which have low values of η_{max} due to an energy gap in the forward direction. The data can be well described by the models as can be seen in Figure d). Both generators don't use a special treatment to generate diffractive events.

Distributions of several jet angular variables are presented in Figure 3.22. The pseudorapidity of the two jets is displayed in Figure a). Most of the jets are found at high η_{jet}. HERWIG slightly underestimates the number of jets at high η_{jet} and PYTHIA at medium η_{jet}. Direct events dominate at low η_{jet}. These findings are corroborated by Figure b) which shows the mean pseudorapidity of the two leading jets, $\overline{\eta}$.

The data as a function of the angle ϕ of the jets as displayed in Figure c) is approximately flat, which is predicted by both models. The absolute value of the cosine of the angle θ^* is shown in Figure d) and is also well modelled by the Monte Carlo models. The number of events decreases with increasing $\cos\theta^*$. This is not the behaviour expected from QCD matrix elements and is due to the cuts in E_T. It means in addition that most of the jets are produced with small $\Delta\eta$ and that the angle θ^* is most likely 90 degree.

Figure 3.23 illustrates the energy distributions. Both the transverse energy of the leading jet $E_{T,max}$ and of the second jet $E_{T,second}$ are equally well modeled by PYTHIA and HERWIG. Jets are found with E_T up to 80 GeV. The proportion of direct events increases with E_T.

A similar behaviour is found in the distribution of the invariant mass of the dijet system M_{JJ} in Figure c). Values of M_{JJ} are found up to 160 GeV.

Figure d) shows the sum of the jet energies $E_{max} + E_{second}$. Again the data is well described. One event is found with very high energetic jets, $E_{max} + E_{second} \approx 600$ GeV. This event is displayed in Figure 3.24. In this event two jets are found with transverse energies of 74 and 71 GeV at pseudorapidities of 2.3 and 1.8, respectively. An invariant dijet mass of 151 GeV has been reconstructed. Both PYTHIA and HERWIG predict ≈ 0.3 events with $E_{max} + E_{second} > 540$ GeV.

The longitudinal photon and proton momentum fractions x_γ and x_P are presented in Figure 3.25 on a linear and logarithmic scale. The data covers x_γ values between 0.1

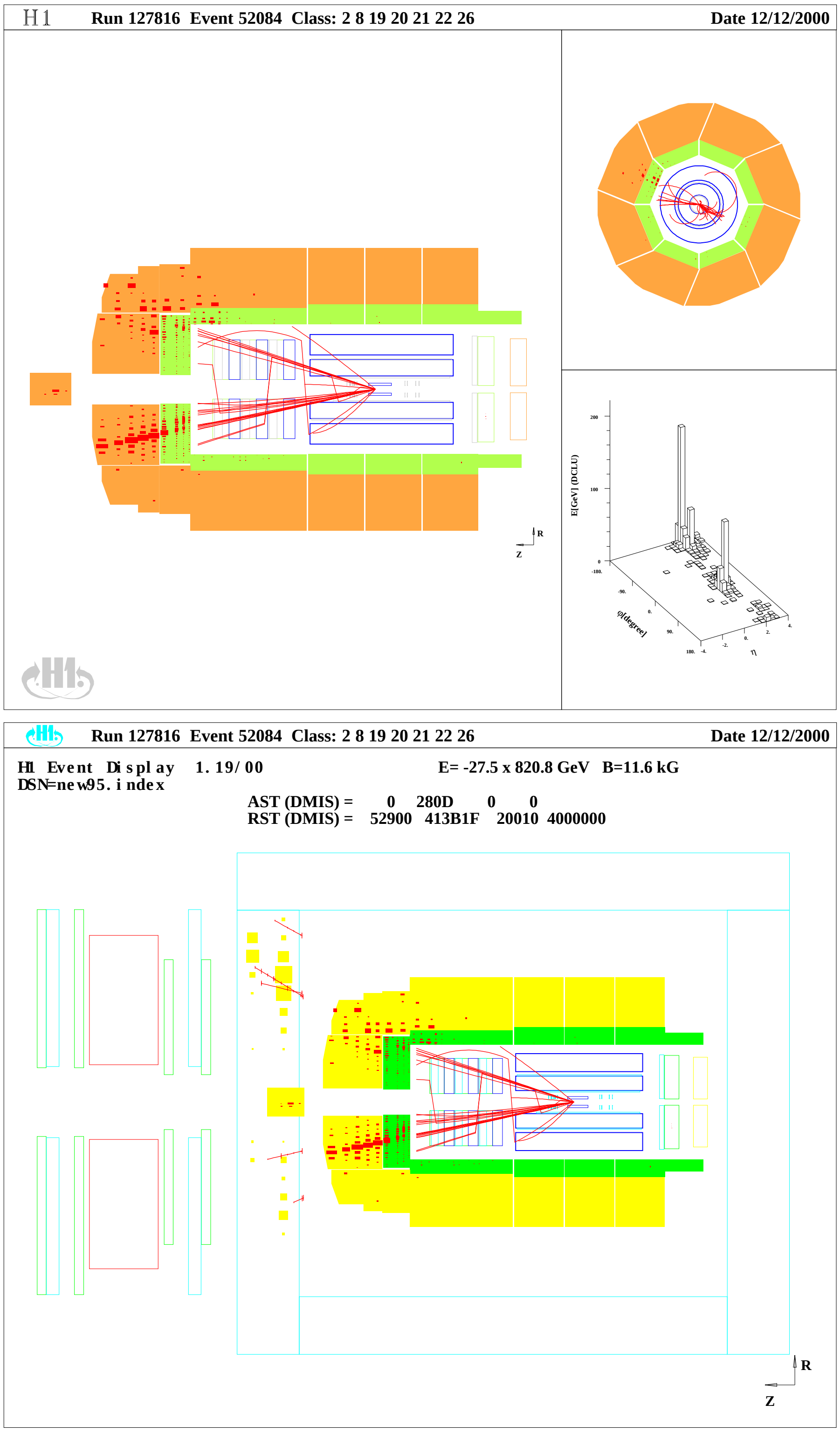

Figure 3.24: *Display of a selected event. The reconstructed tracks and energy deposits in the calorimeters are indicated. The lower figure shows in addition the energy deposits and tracks in the muon system.*

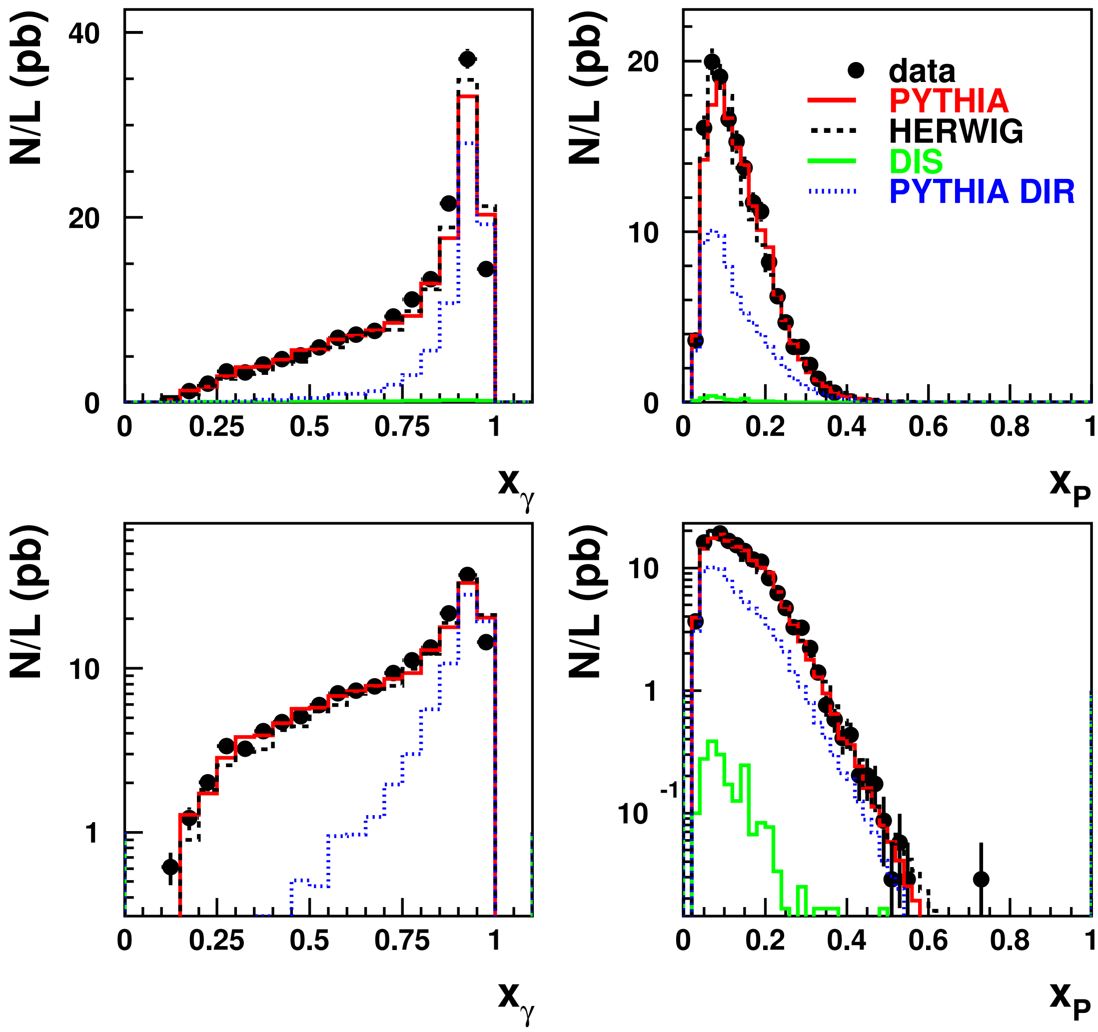

Figure 3.25: *Comparison of the dijet data with HERWIG and PYTHIA. Shown are luminosity normalized distributions of x_γ (lefthand) and x_P (righthand).*

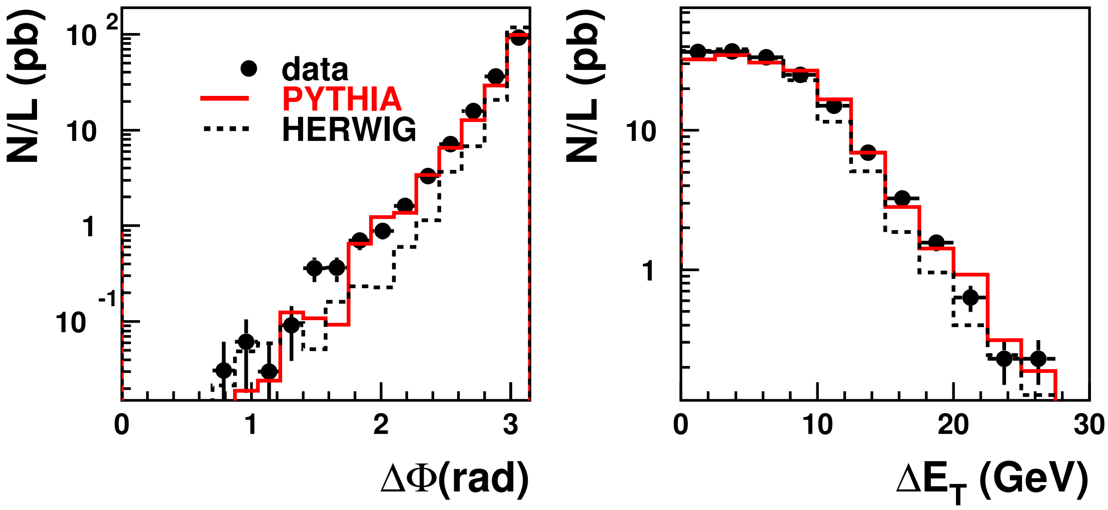

Figure 3.26: *Comparison of the dijet data with HERWIG and PYTHIA. Shown are luminosity normalized distributions of $\Delta\phi$ (lefthand) and ΔE_T (righthand).*

and 1 and x_P values between 0.03 and ≈ 0.73. The event found in the data at highest x_P is the one with the highest $E_{max} + E_{second}$. Apart from this event the data has x_P values up to 0.6. Only at high x_γ the models have slight difficulties in predicting the trend of the data.

A problem of the HERWIG model is visible in Figure 3.26 where the difference in the jet azimuthal angles $\Delta\phi$ and the difference in the jet transverse energies ΔE_T is presented. Both observables are defined as the difference of the leading jet value to the value of the second jet. Herwig underestimates the fraction of events with high $\Delta\phi$ and ΔE_T. In leading order QCD where only two jets are present in the final state, jets have no imbalance of the transverse jet energies and are produced back to back in the ϕ plane ($\Delta\phi = 180^o$). Higher order QCD radiation, resolution and mismeasurement change this picture. Since resolution and detector effects are similar for HERWIG and PYTHIA, one has to conclude that the HERWIG model gives a less good description of additional QCD radiation effects. This discussion will be continued with the 3-jet sample in the next paragraph.

In summary we found that both models give an adequate description of the dijet observables for which a cross section will be determined. A comparison of the models to the measured data in the final binning has also been made. Both models are found to give a reasonable prediction of the data for all bins. This is important for the data unfolding as will be discussed in section 3.5.

3.3.2 The 3-jet Sample

The 3-jet cross section will be measured as a function of several observables. The data is compared as a function of these observables to the HERWIG and PYTHIA predictions.

Both generators fail to describe the normalization. For PYTHIA the ratio of data to MC is 1.35. Since for PYTHIA this ratio is similar to the dijet case the same scale factor of 1.2 has been applied. HERWIG is not able to describe the rate of dijet to 3-jet events. The ratio of data to MC is 4.2, however to simplify a scale factor of 4 is applied.

Figure 3.27 shows the distributions of the invariant mass of the 3 jets M_{JJJ} and the transverse energy distributions of the three jets. The events at high M_{JJJ} (and high E_T) have been scanned and they could not be identified as background. Events with M_{JJJ} values up to ≈ 175 GeV have been found.

Both the PYTHIA and HERWIG descriptions are not perfect. While PYTHIA predicts a slightly steeper slope as the data, the slope of the HERWIG model is less steep. The difference in slope of the two models might be explained by the different α_s evolutions[85] (1-loop for PYTHIA, 2-loop for HERWIG). Although PYTHIA and HERWIG use only the leading order $2 \rightarrow 2$ matrix elements for the event generation the transverse energy of the third jet $E_{T,third}$ is modelled up to 40 GeV.

Similar is found in Figure 3.28 and Figure 3.29. Shown are the invariant masses of the first and second jet M_{12}, the first and third jet M_{13} and the second and third jet M_{23}. Furthermore the distribution of the sum of the transverse energies of the three jets, $E_{T,sum}$, is presented. These observables exploit different kinematic configurations of the 3-jet phase space. The comparison of these distributions with the predictions is also interesting to understand the QCD contribution for various new physics signals.

In Figure 3.29 the mean pseudorapidity of the three jets and two definitions of x_γ are explored. While $x_\gamma^{(3)}$ peaks at one, $x_\gamma^{(2)}$ peaks at lower values as expected from the arguments of section 2. The momentum fraction $x_\gamma^{(3)}$ should be compared with the dijet observable x_γ. For 3-jet events higher x_γ values are found due to the higher centre-of-mass energy which is needed to produce three instead of two high E_T jets.

As can be seen in these Figures the Monte Carlo description is not as good as in the dijet case. But for most regions one model overestimates the data, while the other generator underestimates the data. It is concluded that the models can be used for detector correction. Note that only the shape description is relevant for the unfolding.

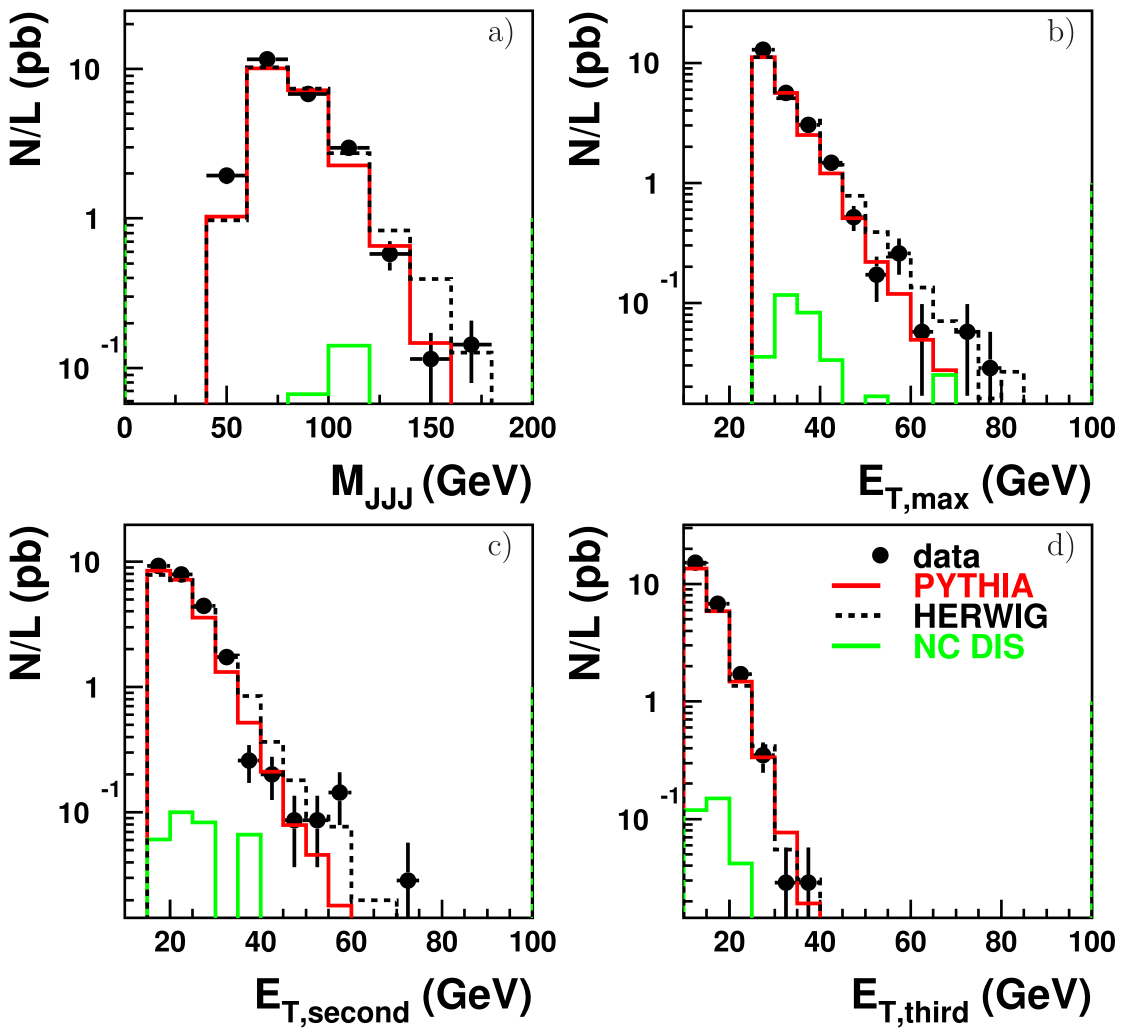

Figure 3.27: *Comparison of the 3-jet data with HERWIG and PYTHIA. Shown are luminosity normalized distributions of M_{JJJ} a), $E_{T,max}$ b), $E_{T,second}$ c) and $E_{T,third}$ d).*

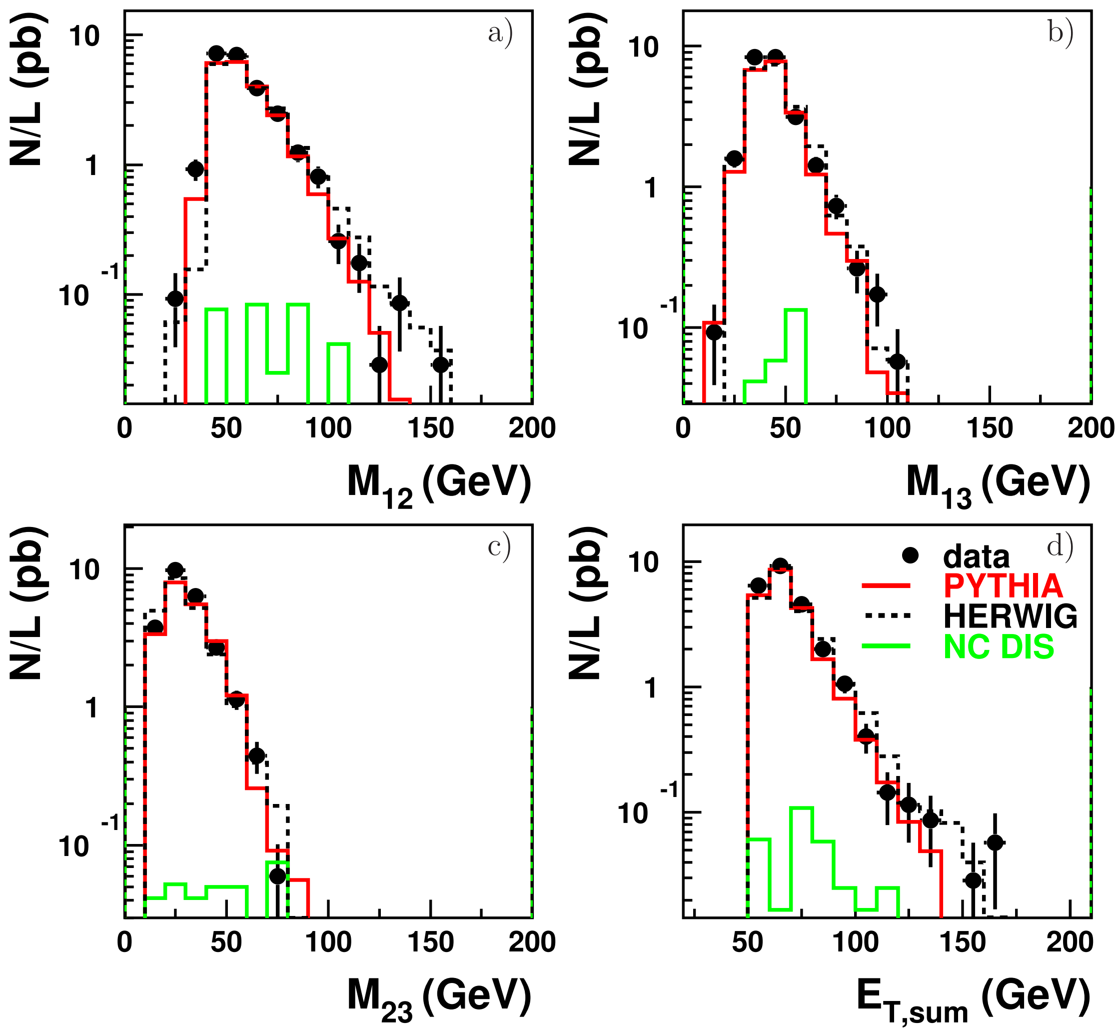

Figure 3.28: *Comparison of the 3-jet data with HERWIG and PYTHIA. Shown are luminosity normalized distributions of M_{12} a), M_{13} b), M_{23} c) and $E_{T,sum}$ d).*

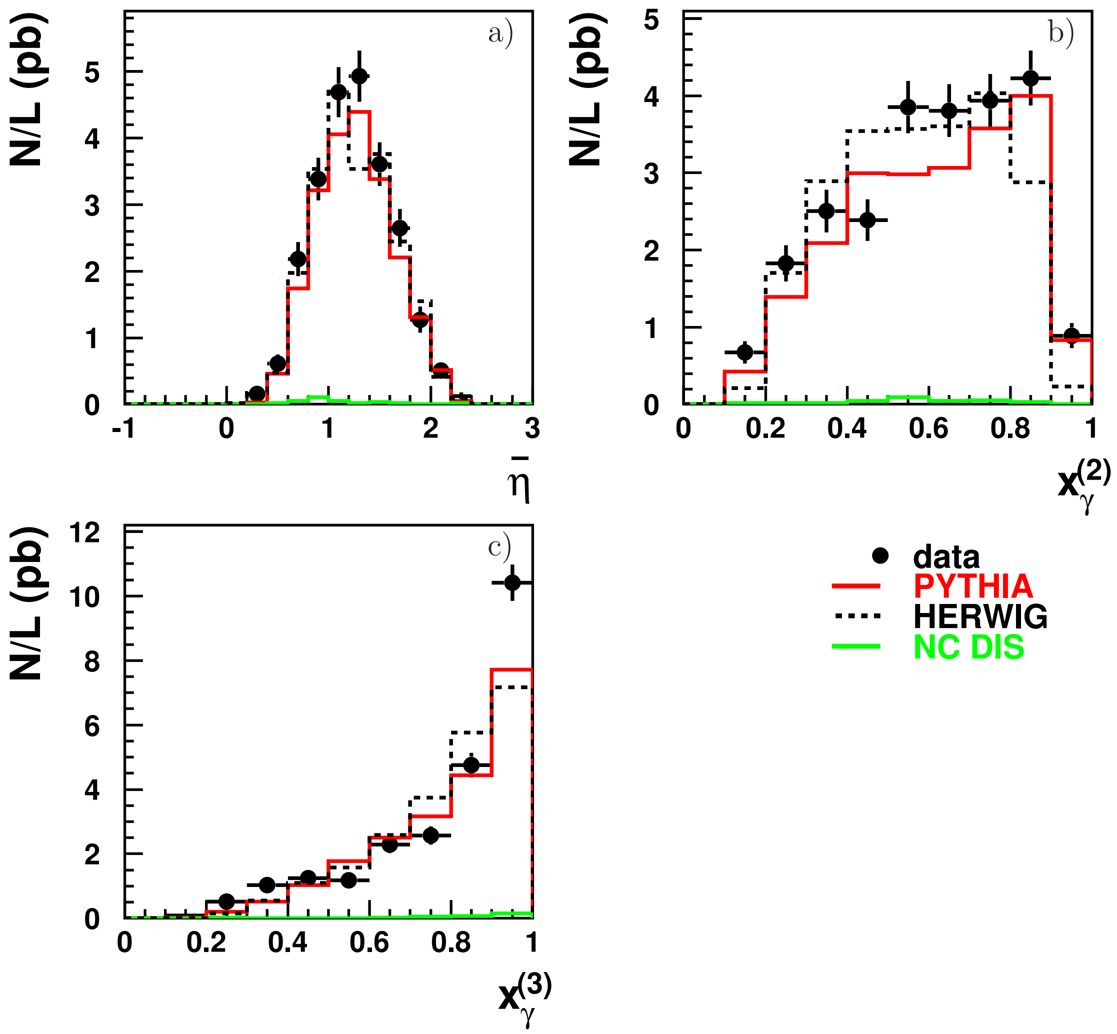

Figure 3.29: *Comparison of the 3-jet data with HERWIG and PYTHIA. Shown are luminosity normalized distributions of $\overline{\eta}$ a), $x_\gamma^{(2)}$ b) and $x_\gamma^{(3)}$ c).*

3.4 Internal jet Structure and Underlying Event

Previous comparisons [89, 90, 92] of HERA data with QCD models like PYTHIA and HERWIG showed that the energy flow adjacent to the jets was found to be above these predictions if no models are included for the so called *soft underlying event*. This *soft underlying event* is the energy at some close distance to the jet axis (often also called the *jet pedestal*).

There are different processes which may contribute to these energies. A source is higher order QCD radiation, e.g. gluons radiated at small angles from the original partons. The energy originates also from the fragmentation processes of the partons out of the hard scattering and of the beam remnants.

Often [89, 90, 92, 93] these energies are not describable by these processes alone. However the data can be described by adding energy coming from interactions of the beam remnants. This means that in hadron-hadron interactions (or in resolved photoproduction), due to the composite nature of the two hadrons, several parton pairs undergo separate scattering, so called *multiple interactions*.

As explained in section 2.8 in HERWIG multiple interactions are included by producing in a fraction P' of the resolved events so called *soft underlying events*. In PYTHIA multiple interactions between the proton and the resolved photon are dealt with by adding additional interactions between spectator partons within the same event.

The effect of multiple interactions is tested by comparing, in the data and in the HERWIG and PYTHIA calculations, the energy flow distributions around the jet axis.

Figure 3.30 and Figure 3.31 show the transverse energy flow per event around the jet axis as a function of the distance to the jet axis in pseudorapidity $\eta - \eta_{jet}$ and in azimuthal angle $\phi - \phi_{jet}$.

The data are compared to the PYTHIA predictions (including the model for multiple scattering) and to HERWIG with and without a fraction P' of events containing the soft underlying event. As expected there is no visible difference between HERWIG with and without the soft underlying event (SUE) for $x_\gamma > 0.8$. But at lower x_γ the pedestal is not fully described with HERWIG without SUE. This is particularly visible in Figure 3.31 where the energy flow as a function of the distance to the jet azimuthal angle is shown. The fraction P' has been fitted to the data. For $P' \sim 30 - 35\%$ these distributions are found to be well described for all regions of x_γ. PYTHIA is also able to describe these distributions. No tuning of this model is necessary.

These findings are confirmed by the measurement of the jet shape of the leading jet.

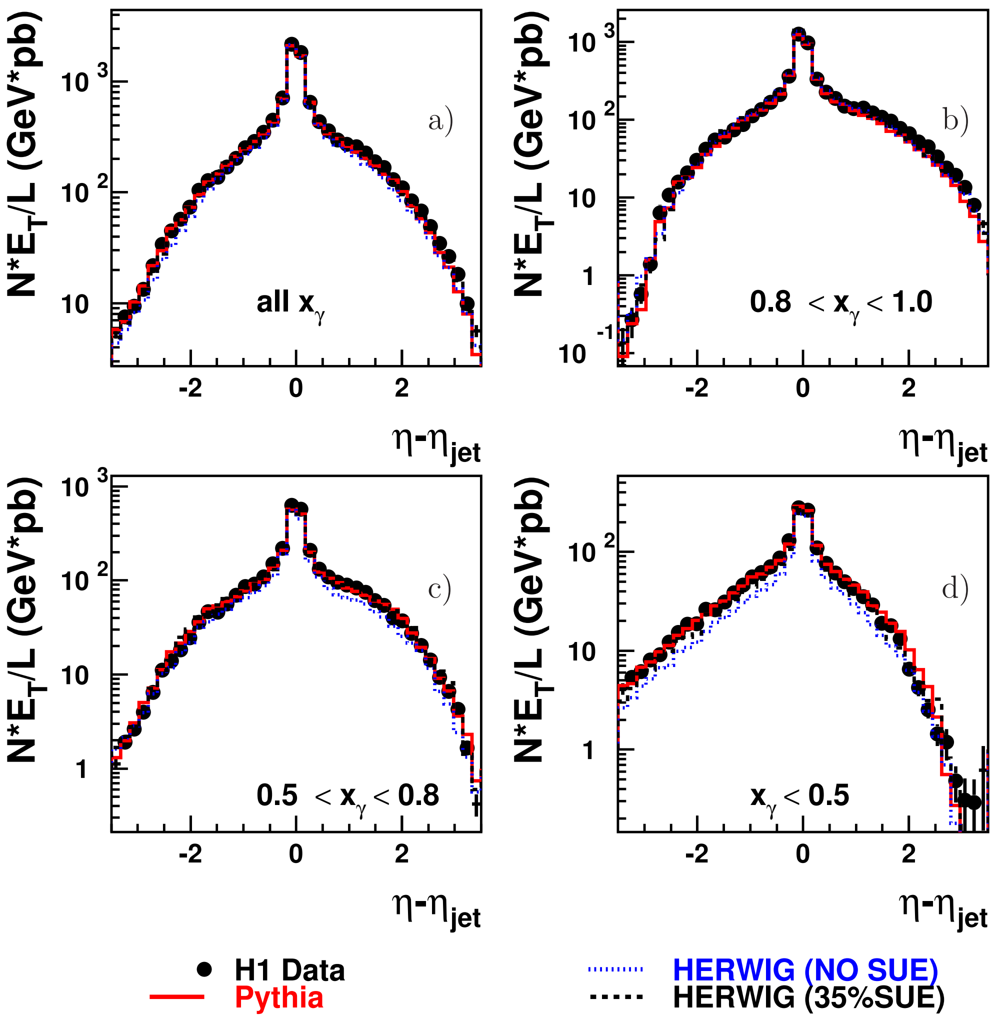

Figure 3.30: *The transverse energy flow around the jet axis normalized to the luminosity as a function of the distance to the jet axis in pseudorapidity $\eta - \eta_{jet}$ normalized to the luminosity. Figure a) shows the distribution for the full data sample, Figure b) for $0.8 < x_\gamma < 1$, Figure c) for $0.5 < x_\gamma < 0.8$ and Figure d) for $x_\gamma < 0.5$. The dijet data are compared to PYTHIA, HERWIG and HERWIG without soft underlying events.*

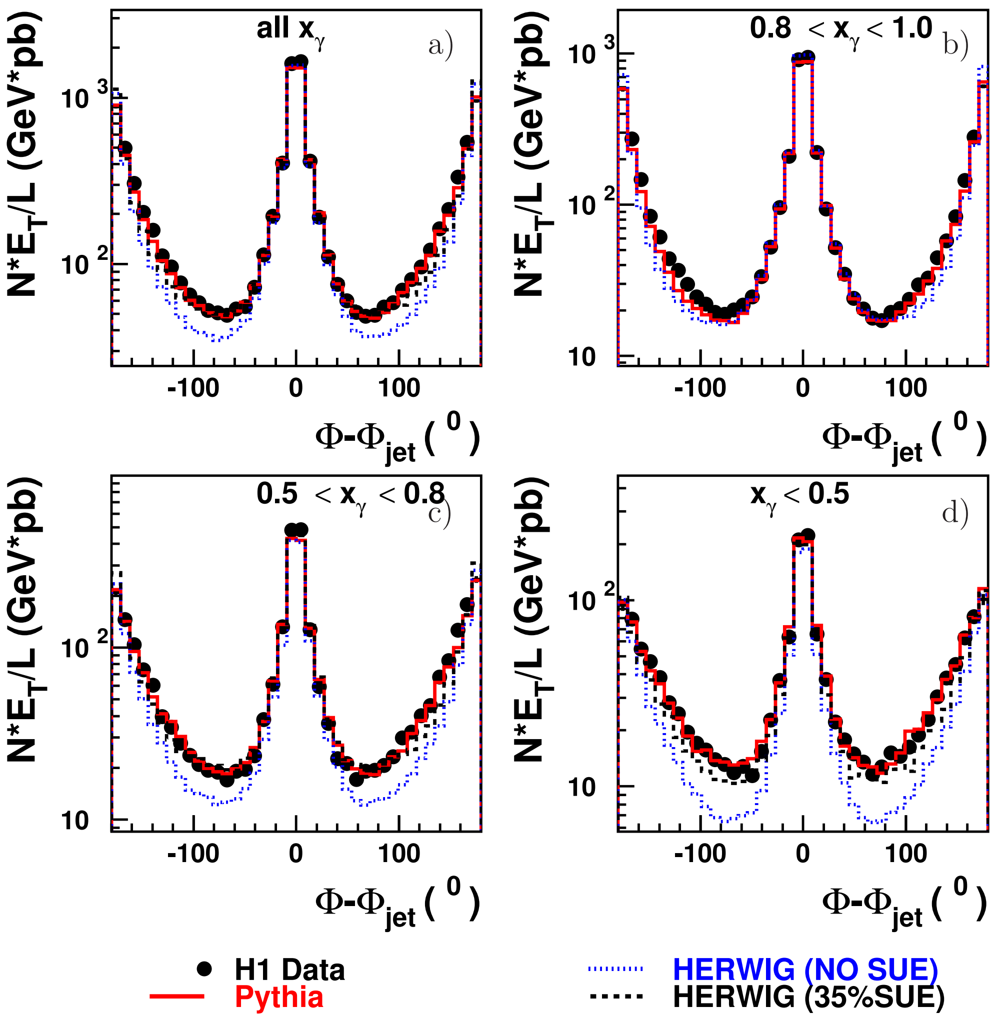

Figure 3.31: *The transverse energy flow around the jet axis normalized to the luminosity as a function of the distance to the jet axis in azimuthal angles $\phi - \phi_{jet}$ normalized to the luminosity. Figure a) shows the distribution for the full data sample, Figure b) for $0.8 < x_\gamma < 1$, Figure c) for $0.5 < x_\gamma < 0.8$ and Figure d) for $x_\gamma < 0.5$. The dijet data are compared to PYTHIA, HERWIG and HERWIG without soft underlying events.*

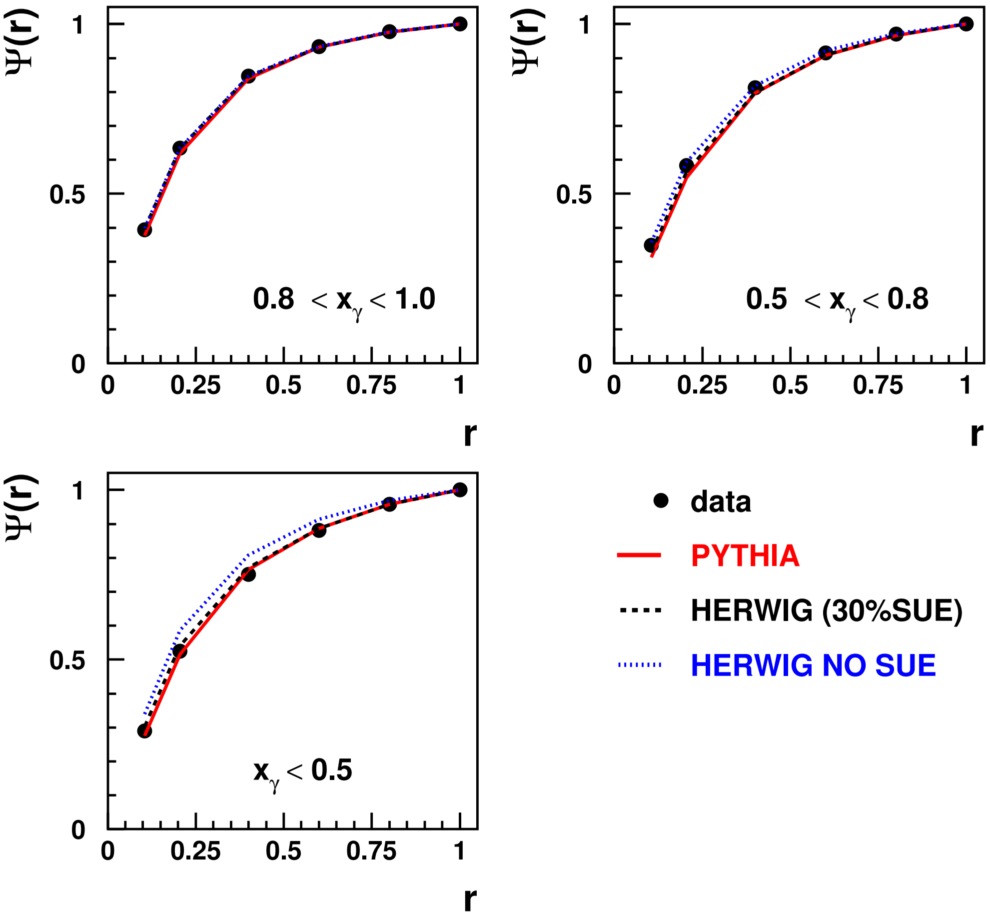

Figure 3.32: *The measured jet shapes $\Psi(r)$ as a function of r in different x_γ regions. The dijet data are compared to PYTHIA, HERWIG and HERWIG without soft underlying events.*

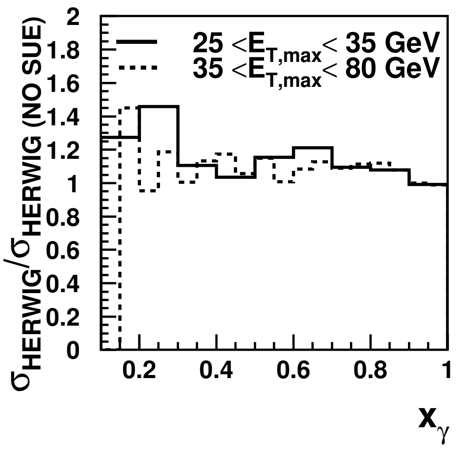

Figure 3.33: *The ratio of the HERWIG dijet cross section $d\sigma/dx_\gamma$ to HERWIG without SUE as a function of x_γ for a $E_{T,max} > 25$ GeV (full line) and $E_{T,max} > 35$ GeV (dashed line).*

The jet shape $\Psi(r)$ is defined as:

$$\Psi(r) = \frac{1}{N_i} \sum_i \frac{E_{T,jet}(r)}{E_{T,r=1}} \quad . \tag{3.6}$$

In this equation is $E_{T,jet}(r)$ the sum of all transverse energies in a cylinder of radius $r = \sqrt{(\phi_i - \phi_{jet})^2 + (\eta_i - \eta_{jet})^2}$ to the jet axis. The sum runs over all events in the sample and N_i is the total number of events.

The dependence of the jet shape on the radius r is presented in Figure 3.32 for different regions in x_γ. The jet shape increases faster with r for events with larger x_γ. Both PYTHIA and the default HERWIG prediction (including 35 % of SUE) describe the data for all regions in x_γ. Again HERWIG without SUE has slight problems in describing the jet shape for $x_\gamma < 0.5$.

The result that multiple interaction models are needed to describe jet shapes in photoproduction was first found in [92] for jets with $E_T > 14$ GeV.

Next the impact of the soft underlying event on the measured cross sections is studied. For that the predicted HERWIG cross sections with and without 35% of soft underlying events as a function of all measured observables has been compared (not shown). The largest difference is found in the dijet cross sections $d\sigma/dx_\gamma$ as a function of x_γ. The ratio of the HERWIG cross sections with and without SUE is shown in Figure 3.33.

The difference of the calculated HERWIG cross sections with and without 35% of soft underlying events is in average 10% for x_γ between $0.3 - 0.8$ and about 20% for

$x_\gamma < 0.3$ [3]. For $x_\gamma > 0.8$ the difference is negligible.
The question arises if one should correct the data for these effects.
The whole concept of multiple interactions is very controversial [57]. Maybe in higher order calculations no additional models are necessary to describe the underlying event. However, a comparison to NLO QCD calculations is not possible since no full event generation — including parton showering and fragmentation — is available within the present NLO QCD programs.
Therefore and due to the fact that the observed differences are small, no correction neither for these effects nor for the underlying event energies of the jets have been applied.

3.5 Unfolding the Data

It has been shown in the last sections that the simulations give a reasonable description of the data. In this section the correction procedure will be described. For a meaningful comparison of the data to theoretical calculations on the parton level, the data has to be corrected for all detector effects. These are limited resolution, mismeasurement and ineffiencies. The data are corrected to the level of hadrons (see section 2.8). All final cross sections refer to jets defined on stable hadrons.
A hadron level phase space has to be defined, which should somehow match the detector level cuts. The phase space should not contain regions where because of acceptance nothing can be measured. This probably leads to large systematic errors. The phase space defining the hadron level cross sections is discussed in section 2 and presented in Table 2.1. The kinematic variables defining this phase space , such as y and Q^2 are the generated variables.
The bin sizes of all distributions will be chosen to match the resolution and to give a good bin efficiency and purity. Then the data can be corrected with the models for detector effects.
The correction was done using the so called bin-to-bin method.
If the correlation between bins is not large, correction factors can be defined in a simple way by calculating the ratio of the cross section for a certain bin after the detector simulation with observables defined on detector objects (detector level) and before the detector simulation (hadron level) with the generated observables. To determine these correction factors the HERWIG and PYTHIA Monte Carlo samples are used. The correction function depend on the Monte Carlo used for correction [4]

[3] The differences calculated with $P' = 30\%$ are slightly lower.

[4] In principle the reconstructed observable is correlated with the generated observable via a 2 dimensional transfer matrix. The off-diagonal elements vanish if the bins are uncorrelated. The

(if there are correlations between bins). Since both Monte Carlos give a reasonable predictions of the data the mean values of the two Monte Carlo generators are taken for the correction. The scale factors are not relevant for the unfolding, because the correction factors are ratios of cross sections.
Half of the difference between the correction factors calculated with HERWIG and PYTHIA is taken as the uncertainty in the detector correction.
To match the bin sizes to the resolution and to see if observables are measured systematically to low or high in some phase space regions the resolution of the observables and the systematic shifts are studied.

3.5.1 Resolution and Systematic Shifts

In this section the reconstructed observables, calculated with detector objects are compared to the generated observables. For all comparisons of reconstructed and generated observables only events are used which fulfil all cuts on both detector and hadron level.
Note that the jet energy resolution in the data is well reproduced by the detector simulation (see Appendix D).
Jets are matched between the detector and hadron level, which means that the distance ΔR in the plane of azimuthal angle and pseudorapidity between hadron level jet axis and detector level jet axis should be less than 1. As a result the permutation of jets is significantly reduced, i.e. the jets of a dijet event are not mixed up between detector and hadron level.
Figure 3.34 illustrates the reconstruction of the transverse energy of the leading jet. It is reconstructed in average ≈ 4 % to high and has a resolution of ≈ 9 %. The ratio of reconstructed to generated $E_{T,max}$ is presented as a function of the generated $E_{T,max}$ and as a function of θ of the leading jet. The ratio is almost flat as a function of θ and $E_{T,max}$. This is an improvement in comparison to the default calibration. The error bars denote the standard deviation of the ratio.
The invariant dijet mass M_{JJ} is reconstructed in average at the generated value. The resolution is $\approx 10\%$ (Figure 3.35). But at $M_{JJ} > 80$ GeV the invariant dijet mass is reconstructed systematically 2% to low. This should be compared to Figure 3.36 where the ratio of reconstructed M_{JJ} to generated M_{JJ} is shown without applying the final jet recalibration. Here the reconstructed M_{JJ} is about 5% to low.

---

result is then the simple bin-to-bin method[94]. However the bin-to-bin method can also be used if the correlations between bins are small. Then two conditions have to be fulfilled [95, 96]:
- the bin sizes should be matched to the resolutions and migrations between the bins should be small
- the Monte Carlo models should give a good description of the data

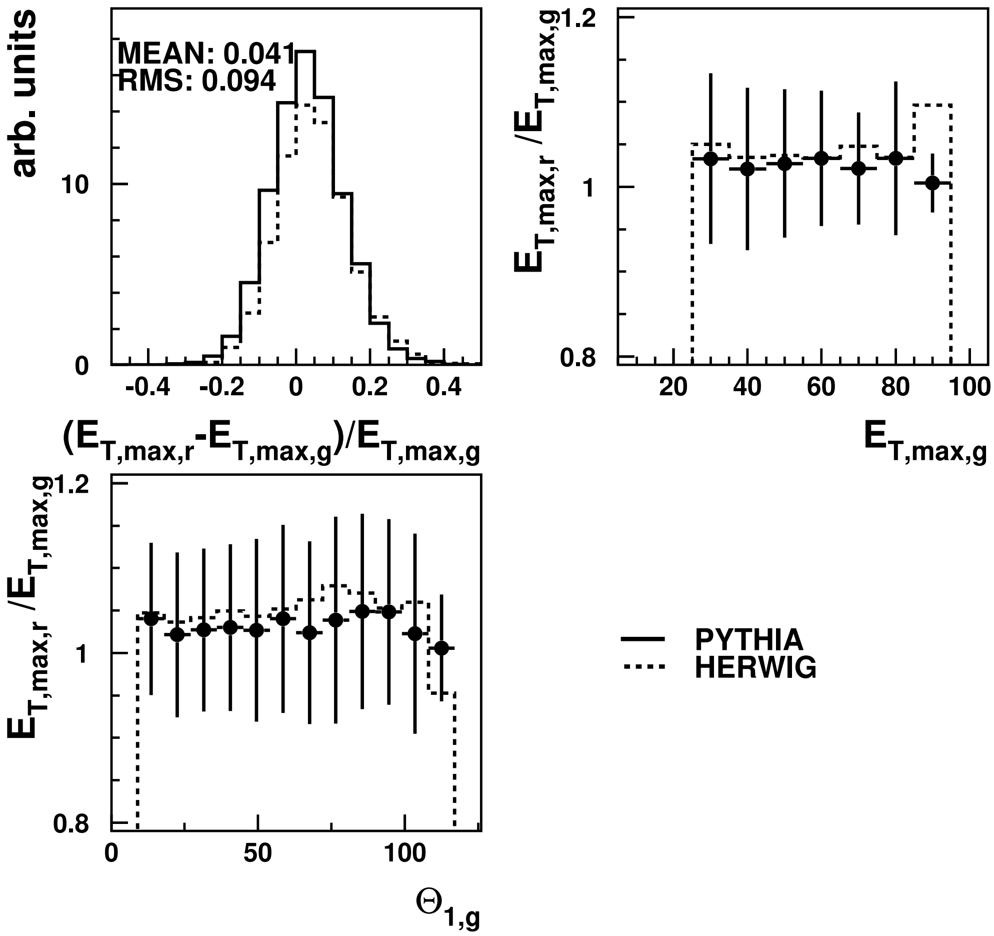

Figure 3.34: *The resolution of $E_{T,max}$ determined with PYTHIA (full line and points) and HERWIG (dotted line) and the ratio of reconstructed and generated $E_{T,max}$ as a function of the generated $E_{T,max}$ and of the generated θ of the leading jet. The resolution is shown as error bars.*

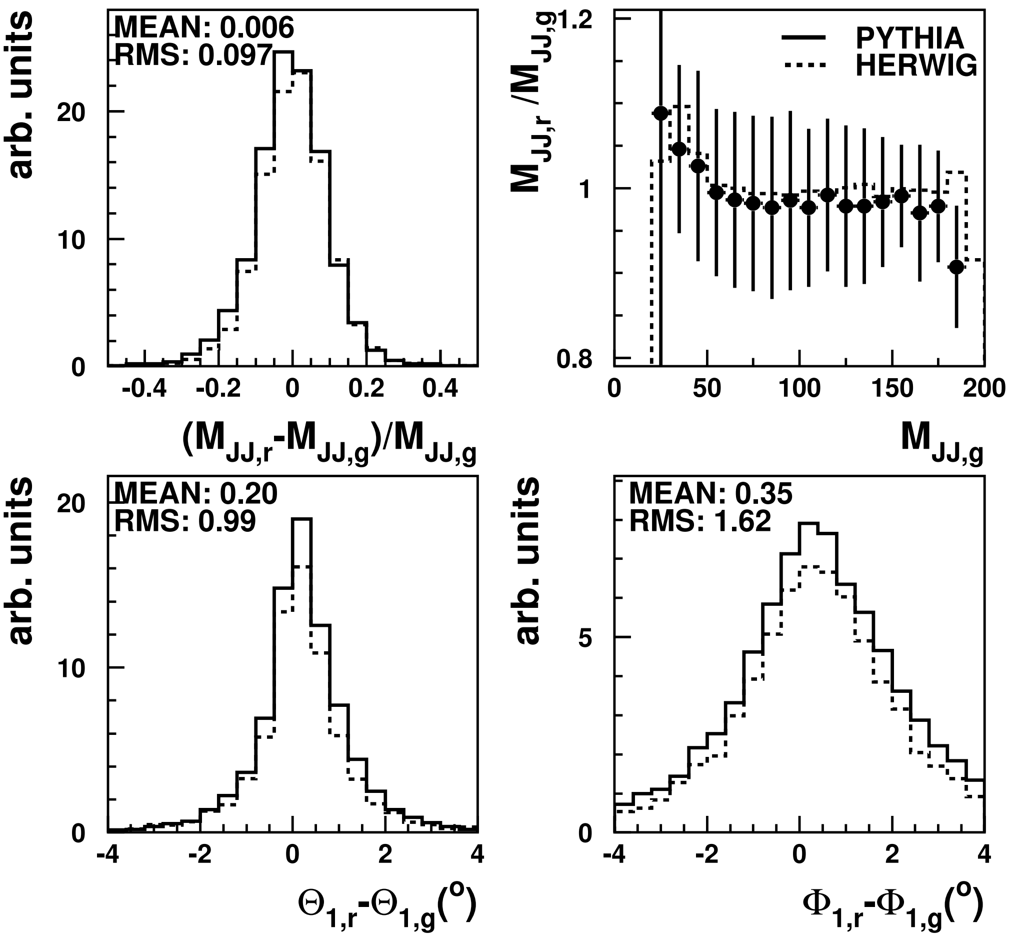

Figure 3.35: *The resolution of M_{JJ} determined with PYTHIA (full line and points) and HERWIG (dotted line) (Figure a) and the ratio of reconstructed and generated M_{JJ} as a function of the generated M_{JJ} (Figure b). The two lower figures show the resolution of θ and ϕ of the leading jet. The resolution is shown as error bars.*

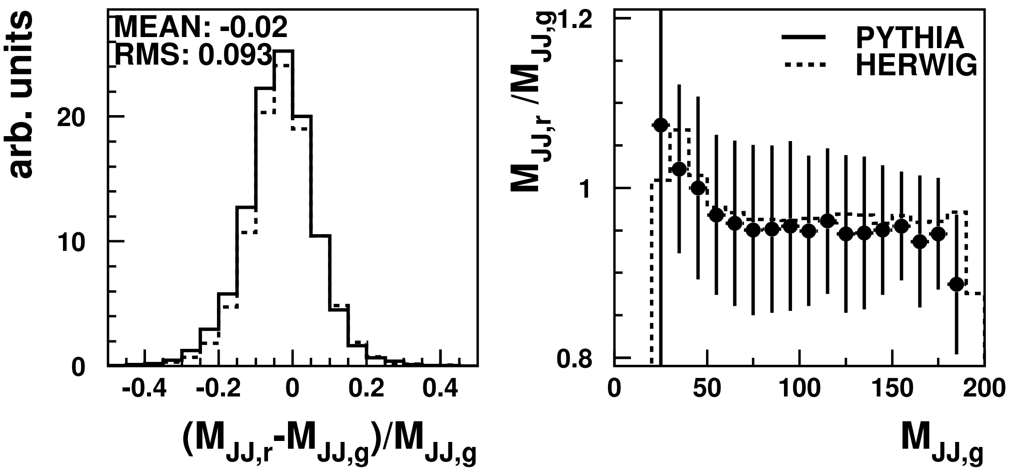

Figure 3.36: *The resolution of M_{JJ} determined with PYTHIA (full line and points) and HERWIG (dotted line) (Figure a) and the ratio of reconstructed and generated M_{JJ} as a function of the generated M_{JJ} (Figure b). The resolution is shown as error bars. No E_T and θ dependent calibration is used.*

Figure 3.35 shows in the resolution in θ and ϕ. The θ angle can be measured with a resolution of $\approx 1^o$, while the ϕ resolution is 1.6^o. The resolution of the pseudorapidity η_{jet} is not shown. It is 0.04 units in pseudorapidity. No substantial shifts have been observed in the angular variables.
Finally the ability to reconstruct x_γ and x_P is investigated in Figure 3.37. The energy fraction x_γ is reconstructed in average 3% to high with a resolution of $\approx$ 10 %. A strong shift to higher values than the values found on the hadron level is observed at low x_γ, e.g. for $x_\gamma < 0.3$ it is reconstructed about 30% to high. An explanation for this might be the decrease of resolution with decreasing x_γ.
The bin sizes of the measured cross sections will be chosen appropriately.
The energy fraction x_P is measured with a resolution of 10 % and only at very high x_P a systematic shift is observed.
Similar resolutions and shifts are found for the 3-jet sample. As an example the resolution of the 3-jet invariant mass M_{JJJ} is pictured in Figure 3.38. While the resolution is found to be around 8 %, again no shift is observed.

3.5.2 Detector Correction

In this section it is explained how the corrected hadron level cross sections are obtained. As a first step the bins have to be defined. It is required that the bin sizes are

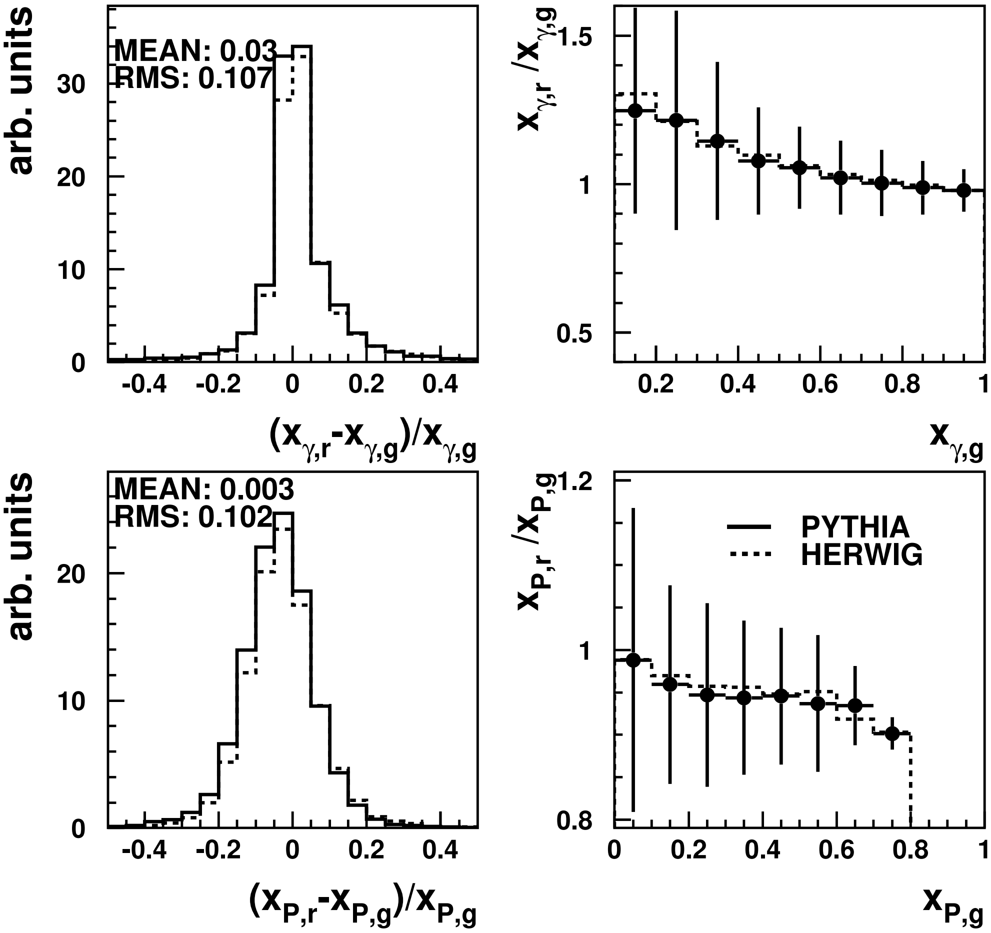

Figure 3.37: *The resolution of x_γ and x_P (Figure a) and c)) determined with PYTHIA (full line and points) and HERWIG (dotted line) and the ratio of reconstructed and generated x_γ and x_P a function of the generated x_γ and x_P respectively in Figure b) and d). The resolution is shown as error bars.*

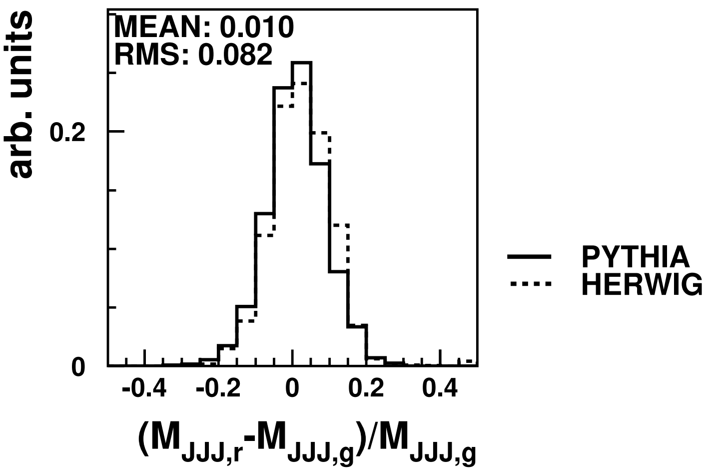

Figure 3.38: *The resolution of M_{JJJ} determined with PYTHIA (full line) and HERWIG (dotted line).*

significant larger than the obtained resolutions. Furthermore all bins should contain a reasonable number of events and both the efficiency and purity have to be above $\approx 30\%$. Although bins are shown in the following Figures with lower efficiency or purity, cross sections are only determined for bins which fulfill these requirements. The bin sizes are chosen such that efficiencies and purities are typically 50 percent for the single differential cross sections and 40 percent for the double differential cross sections.

The efficiency and purity are defined as the fraction of events generated in a given bin i and measured back in the same bin after detector simulation and reconstruction $N_{\mathrm{det.\,and\,had.}}$, divided by all events found in this bin after simulation and reconstruction N_{det} (purity) or divided by the events generated in this bin N_{had} (efficiency):

$$\mathrm{Purity}(i) = \frac{N_{\mathrm{det.\,and\,had.}}(i)}{N_{\mathrm{det.}}(i)} \tag{3.7}$$

$$\mathrm{Efficiency}(i) = \frac{N_{\mathrm{det.\,and\,had.}}(i)}{N_{\mathrm{had.}}(i)} \tag{3.8}$$

The correction functions $C(i)$ are calculated from the ratio of the cross sections with jets reconstructed from hadrons (hadron level) to the cross sections with jets reconstructed from detector objects (detector level) in each bin, where each sample was subject to the selection criteria:

$$C(i) = \frac{\sigma_{\text{had.}}(i)}{\sigma_{\text{det.}}(i)} \tag{3.9}$$

The selection criteria for the detector level are summarised in Table 3.1. Likewise selection criteria for the hadron level are summarised in Table 2.1.
Both the detector level cross section $\sigma_{\text{det.}}$ and the hadron level cross section $\sigma_{\text{had.}}$ are calculated with the Monte Carlo generated events.
All purities, efficiencies and correction factors are displayed in the Figures 3.39-3.47. The dijet correction functions of HERWIG and PYTHIA are in good agreement and differ on average by 5 % and at most by 20 %. The 3-jet correction functions differ in average by 10 % and at most by $\approx 90\%$. But the data cross sections in this bin at high $E_{T,sum}$ contains only 3 events.
The mean values of the two Monte Carlo generators are taken for the correction. The resulting correction factors typically have values between 0.8 and 1.2.
Before the data is corrected for detector effects the backgrounds due to NC DIS events are subtracted statistically. Thus the fully corrected cross sections σ_{ep} are obtained by:

$$\sigma_{ep}(i) = (\sigma_{\text{measured}}(i) - \sigma_{\text{backgr.}}(i))\ C(i) \tag{3.10}$$

The measured data cross section before correction is σ_{measured}, the NC DIS background cross section is $\sigma_{\text{backgr.}}$.

3.6 Systematic Uncertainties

For the jet cross sections the following sources of systematic error are considered:

- A 2% uncertainty in the LAr energy scale results in an uncertainty of typically 10%.
- A 8% uncertainty in the hadronic Spacal energy scale results in an uncertainty of 1 %.
- In addition to the variations of the calorimeter energy scales a shift of 1% on y is considered. This variation results in an uncertainty of 3%.
- Half of the difference between the correction factors calculated with HERWIG and with PYTHIA is taken as the uncertainty in the detector correction. For the dijet cross sections the resulting uncertainty is less than 10%. The minimum uncertainty is set to 2%. For the 3-jet cross sections the resulting uncertainty is $5 - 50\%$. The minimum uncertainty is set to 4%.

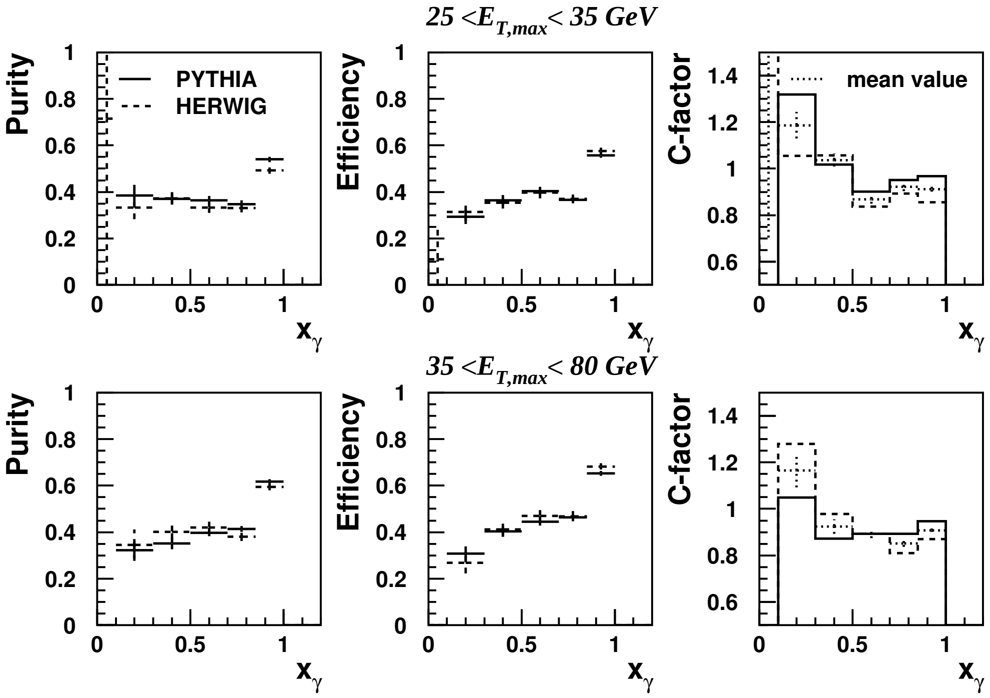

Figure 3.39: *The purities, efficiencies and correction factors for the detector correction determined with PYTHIA (full line) and HERWIG (dashed line) for the chosen bins in x_γ in two regions of $E_{T,max}$. The dotted line shows the mean correction factor.*

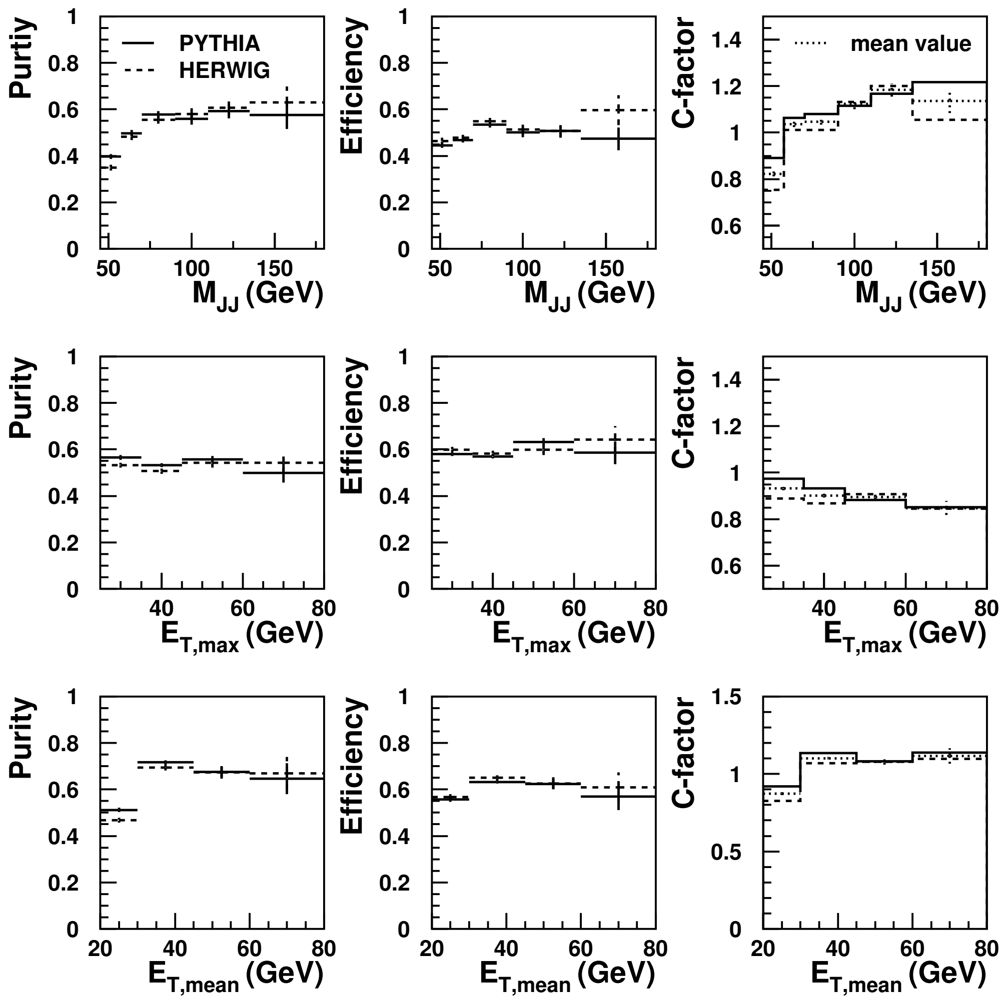

Figure 3.40: *The purities, efficiencies and correction factors for the detector correction determined with PYTHIA (full line) and HERWIG (dashed line) for the chosen bins in M_{JJ}, $E_{T,max}$ and $E_{T,mean}$. The dotted line shows the mean correction factor.*

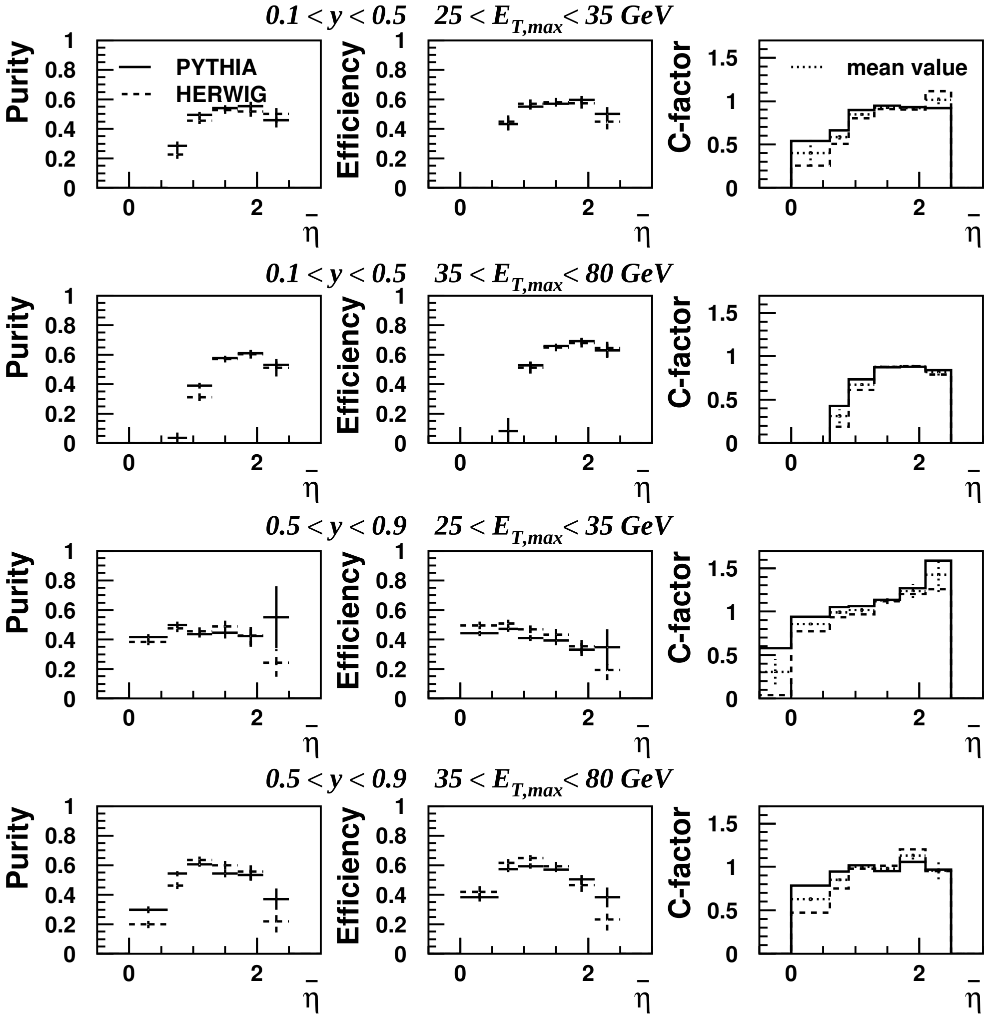

Figure 3.41: *The purities, efficiencies and correction factors for the detector correction determined with PYTHIA (full line) and HERWIG (dashed line) for the chosen bins in $\overline{\eta}$ for different $E_{T,max}$ and y regions. The dotted line shows the mean correction factor.*

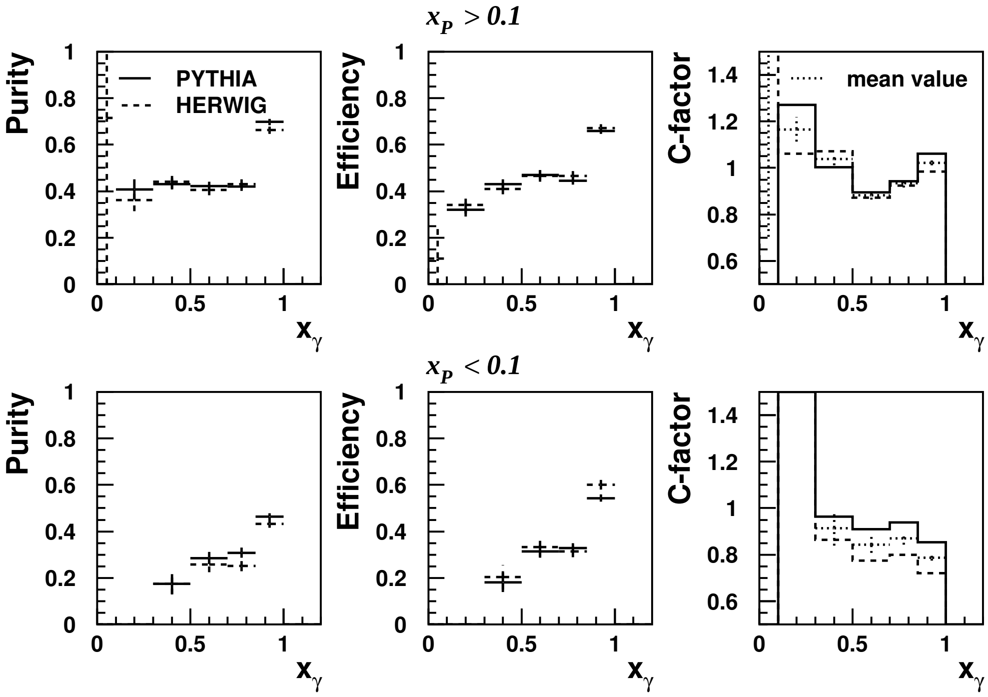

Figure 3.42: *The purities, efficiencies and correction factors for the detector correction determined with PYTHIA (full line) and HERWIG (dashed line) for the chosen bins in x_γ for different x_P regions. The dotted line shows the mean correction factor.*

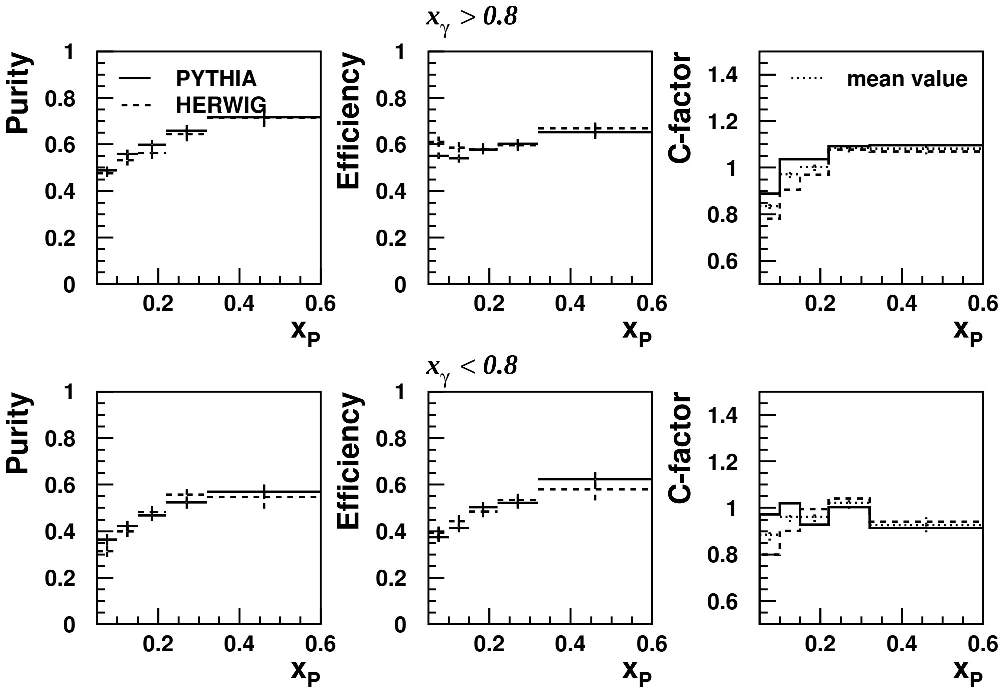

Figure 3.43: *The purities, efficiencies and correction factors for the detector correction determined with PYTHIA (full line) and HERWIG (dashed line) for the chosen bins in x_P for different x_γ regions. The dotted line shows the mean correction factor.*

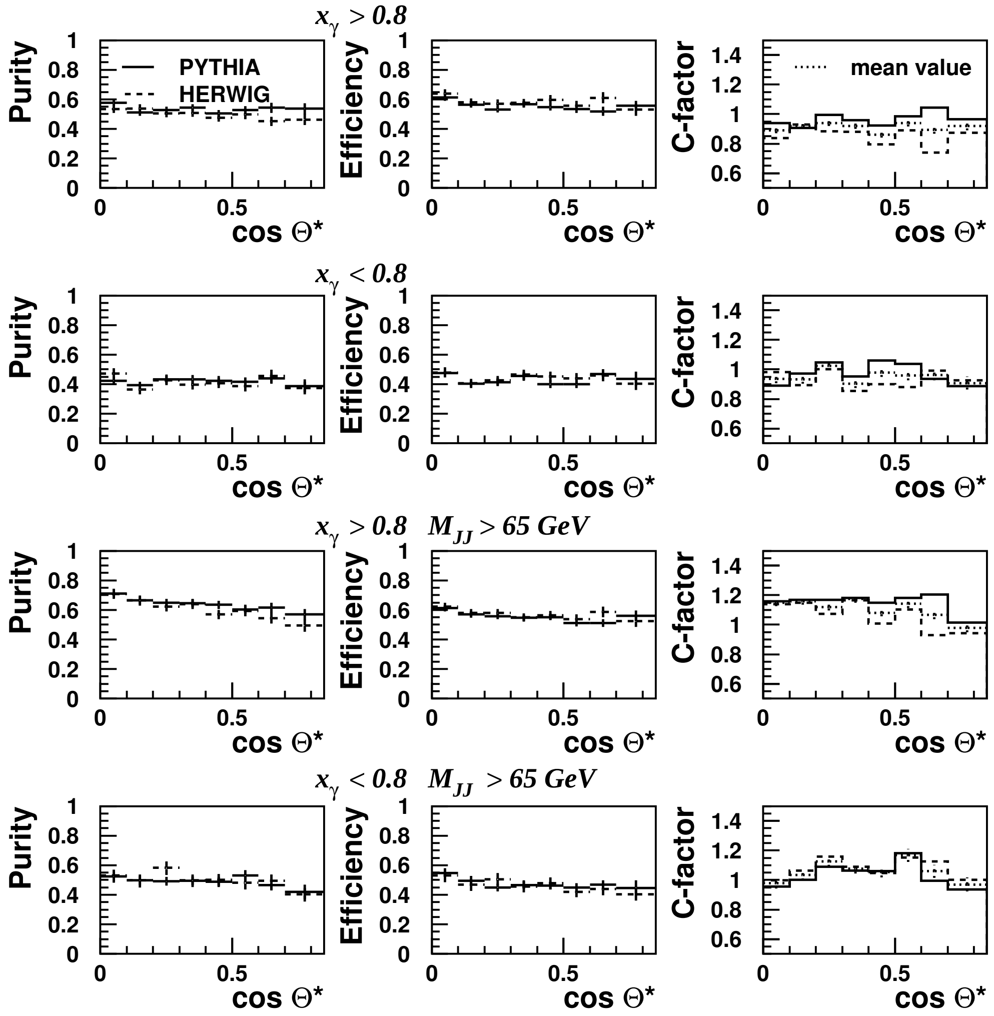

Figure 3.44: *The purities, efficiencies and correction factors for the detector correction determined with PYTHIA (full line) and HERWIG (dashed line) for the chosen bins in $\cos\theta^*$ for different x_γ regions and for an additional cut in M_{JJ}. The dotted line shows the mean correction factor.*

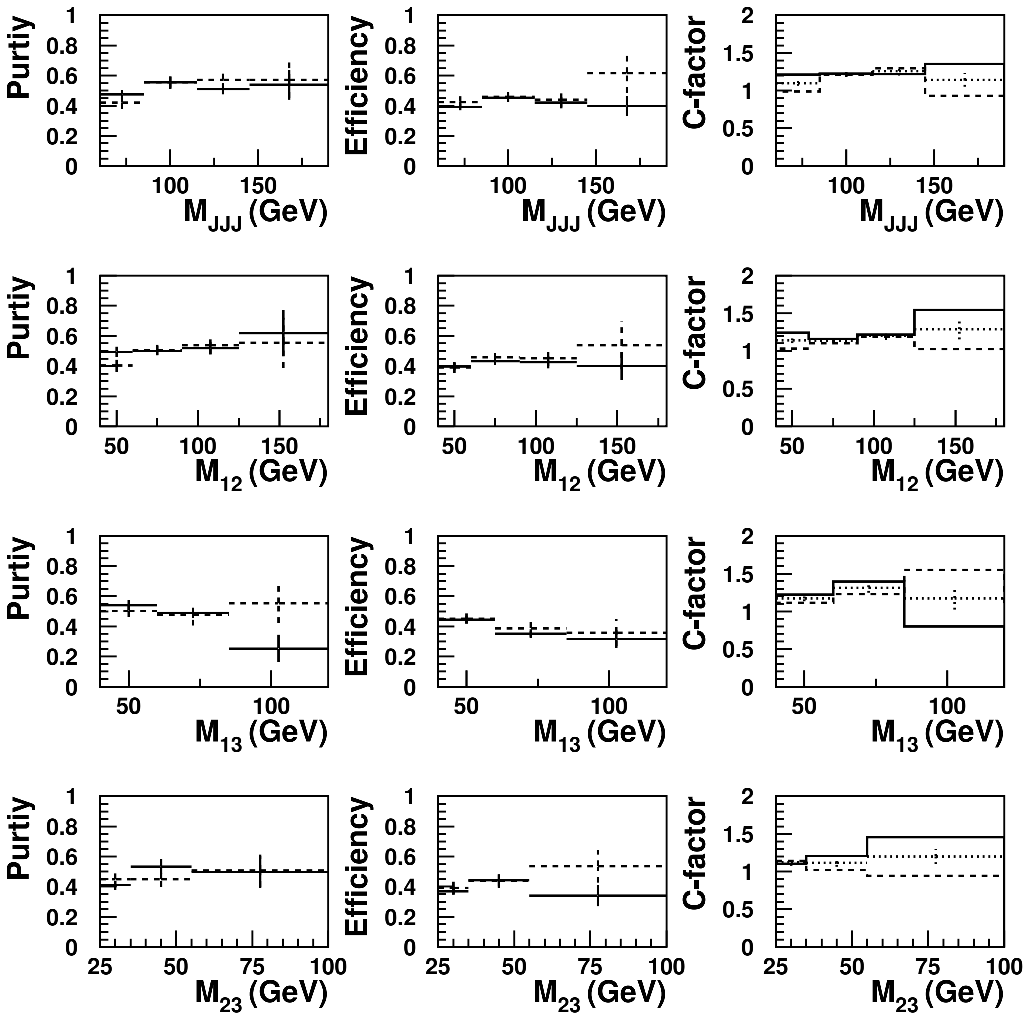

Figure 3.45: *The purities, efficiencies and correction factors for the detector correction determined with PYTHIA (full line) and HERWIG (dashed line) for the chosen bins in M_{JJJ}, M_{12}, M_{13} and M_{23}. The dotted line shows the mean correction factor.*

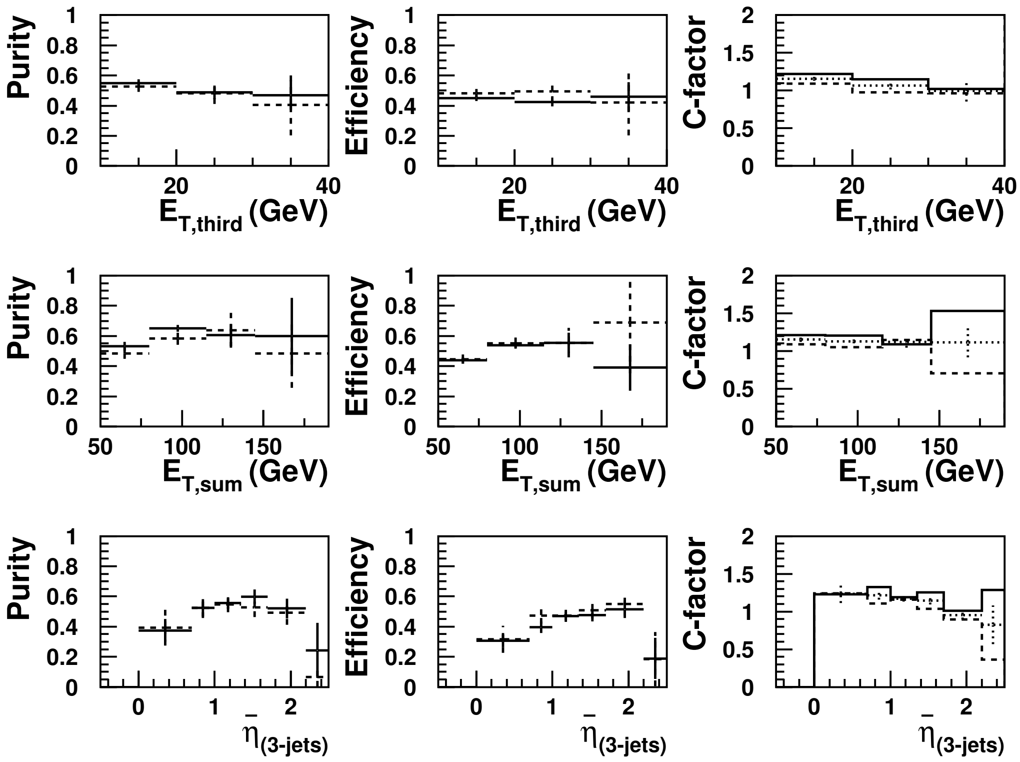

Figure 3.46: *The purities, efficiencies and correction factors for the detector correction determined with PYTHIA (full line) and HERWIG (dashed line) for the chosen bins in $E_{T,third}$, $E_{T,sum}$ and $\overline{eta}$. The dotted line shows the mean correction factor.*

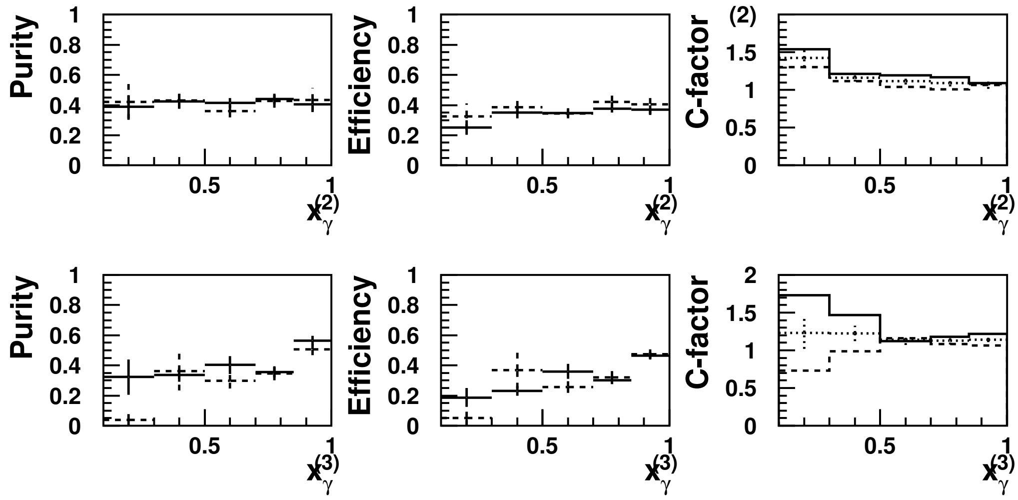

Figure 3.47: *The purities, efficiencies and correction factors for the detector correction determined with PYTHIA (full line) and HERWIG (dashed line) for the chosen bins in $x_\gamma^{(2)}$ and $x_\gamma^{(3)}$. The dotted line shows the mean correction factor.*

- The uncertainty in the trigger efficiency results in an error of $\sim 3\%$.
- The uncertainty in the background subtraction results in an error of $\sim 2\%$ for the dijet cross sections and in an error of $\sim 5\%$ for the 3-jet cross sections.
- The uncertainty in the integrated luminosity results in an overall normalisation error of 1.5%.

The statistical and all systematic errors are added in quadrature. The resulting total uncertainty ranges from 10 to 30% dijet cross sections and from 20 to 80% for the 3-jet cross sections. The systematic contribution is dominated by uncertainties in the calorimeter energy scales and in the correction to the hadron level [5].

[5]Additional systematic errors due to threshold effects at the cut boundaries are also studied. Therefore the cuts in the E_T of the jets are varied at the detector level by about 1 σ of the energy resolution (i.e. 10% for $E_T = 25\text{GeV}$). Unfolding these data back to the proper phase space negligible changes of the cross section as function of E_T, and values always smaller than the model uncertainty for the x_γ distribution are found. It is concluded that these uncertainties are already taken into account into the various other systematic errors.

4
Results

4.1 Measurement of dijet Cross Sections

The measured cross sections for inclusive dijet production in the reaction $ep \rightarrow e\,\mathrm{jet}\,\mathrm{jet}\,X$ are given as single differential cross sections in all cases. The data are corrected for detector effects and are presented at the level of stable hadrons for the phase space region defined in Table 2.1. The inner error bars of the data points in the figures denote the statistical, the outer error bars the total uncertainty. The data are also presented in Tables A.1-A.6. All results are compared to next-to-leading order (NLO) QCD predictions obtained with the standard setting described in section 2.7 if not otherwise quoted. The predictions of NLO QCD corrected for hadronization effects NLO$(1 + \delta_{hadr})$ are also shown.
In Figure 4.1 the dijet cross section is shown as a function of the invariant mass M_{JJ} of the dijet system. The data are presented for M_{JJ} values between 45 and 180 GeV. The measured cross section falls by about 3 orders of magnitude over this range. NLO QCD describes the measured cross sections for the whole mass range. Hadronization corrections are less than 5% for all bins. The calculation using LO matrix elements fails to describe the low M_{JJ} region. This is partly due to the fact that the low M_{JJ} region is populated by events which are influenced by the asymmetric cuts on the jet transverse energies. Events in which the second jet has a transverse energy below 25 GeV contribute mainly in this region. In dijet calculations they only appear beyond leading order. The scale uncertainties in the QCD predictions are largest at low M_{JJ} values.
A similar statement on the large scale uncertainties and the difference between data and the LO calculation holds for small transverse momenta. In Figure 4.2a) the dijet cross section $d\sigma/dE_{T,mean}$ is shown. Here the scale uncertainties decrease from $\pm 20\%$ for the first bins to less than $\pm 5\%$ for $E_{T,mean} > 30$ GeV. The data are well described by the NLO calculation. The dijet cross section as a function of the transverse energy of the highest transverse energy jet $E_{T,max}$ is shown in Figure 4.2b). The distribution

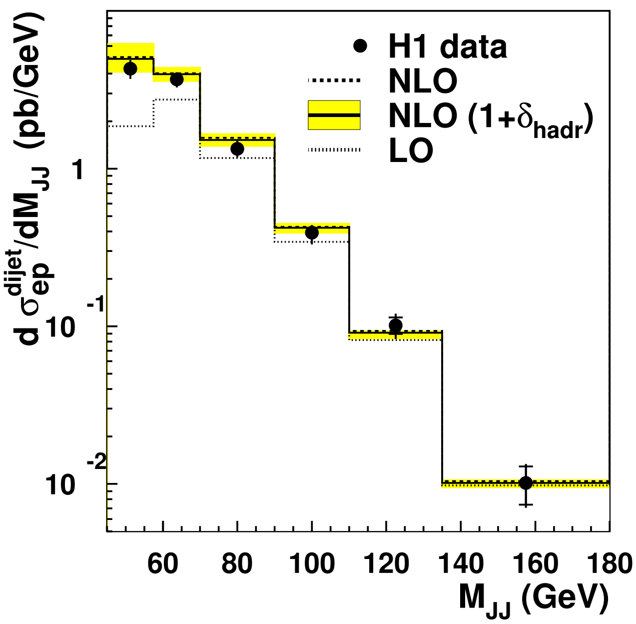

Figure 4.1: *Differential ep cross section for dijet production ($Q^2 < 1\mathrm{GeV}^2$) as a function of the invariant dijet mass M_{JJ} of the two highest E_T jets. Here, as well as in the following figures unless explicitly stated otherwise, the inner error bars denote the statistical error, the outer error bars the total uncertainties of the data. The LO predictions using CTEQ5M pdfs for the proton and GRV-HO pdfs for the photon are shown as a dotted line. NLO predictions with the same pdfs are shown as a dashed line. The full line shows the NLO predictions, including hadronization corrections and the grey band indicates the renormalization and factorization scale uncertainties of the NLO prediction.*

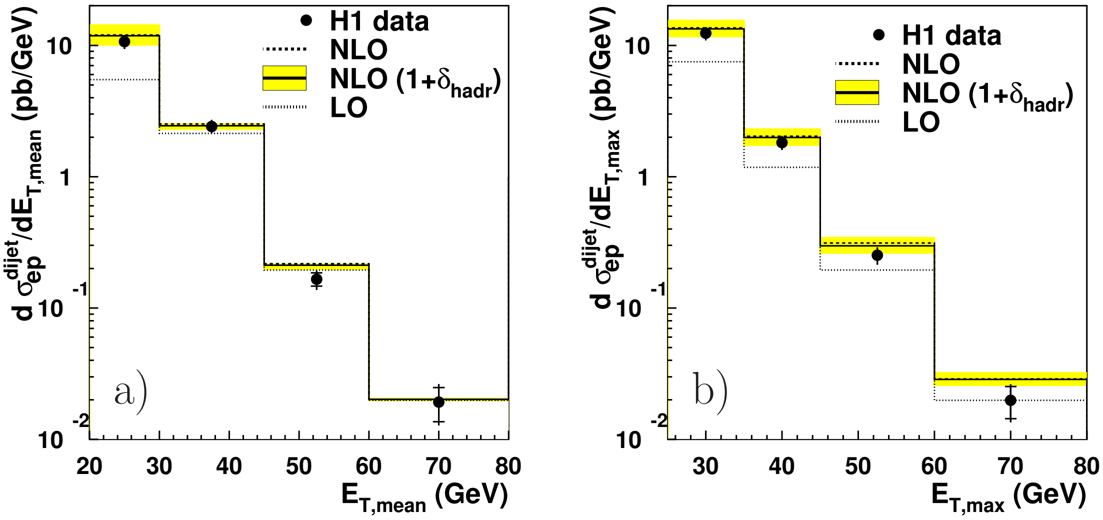

Figure 4.2: *Differential ep cross sections for dijet production ($Q^2 < 1\mathrm{GeV}^2$) as a function of a) $E_{T,mean}$, the mean and b) $E_{T,max}$, the maximum E_T of the two highest E_T jets. The LO predictions using CTEQ5M pdfs for the proton and GRV-HO pdfs for the photon are shown as a dotted line. NLO predictions with the same pdfs are shown as a dashed line. The full line shows the NLO predictions, including hadronization corrections and the grey band indicates the renormalization and factorization scale uncertainties of the NLO prediction.*

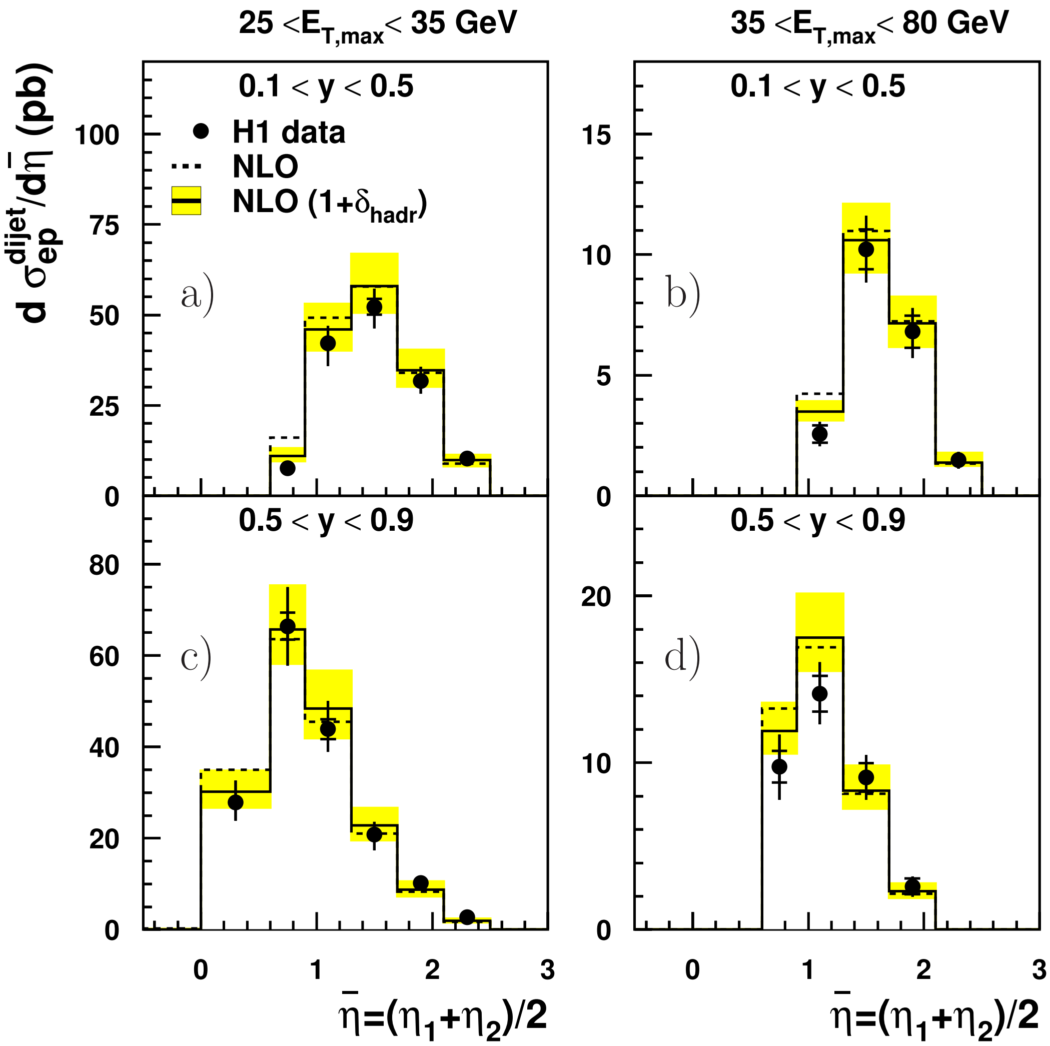

Figure 4.3: *Differential ep cross sections for dijet production ($Q^2 < 1\mathrm{GeV}^2$) as a function of the $\overline{\eta}$ of the two highest E_T jets. The regions of low y, a) and b) and high y, c) and d) are shown for two ranges of $E_{T,max}$. NLO predictions using CTEQ5M pdfs for the proton and GRV-HO pdfs for the photon are shown as a dashed line. The full line shows the NLO predictions, including hadronization corrections and the grey band indicates the renormalization and factorization scale uncertainties of the NLO prediction.*

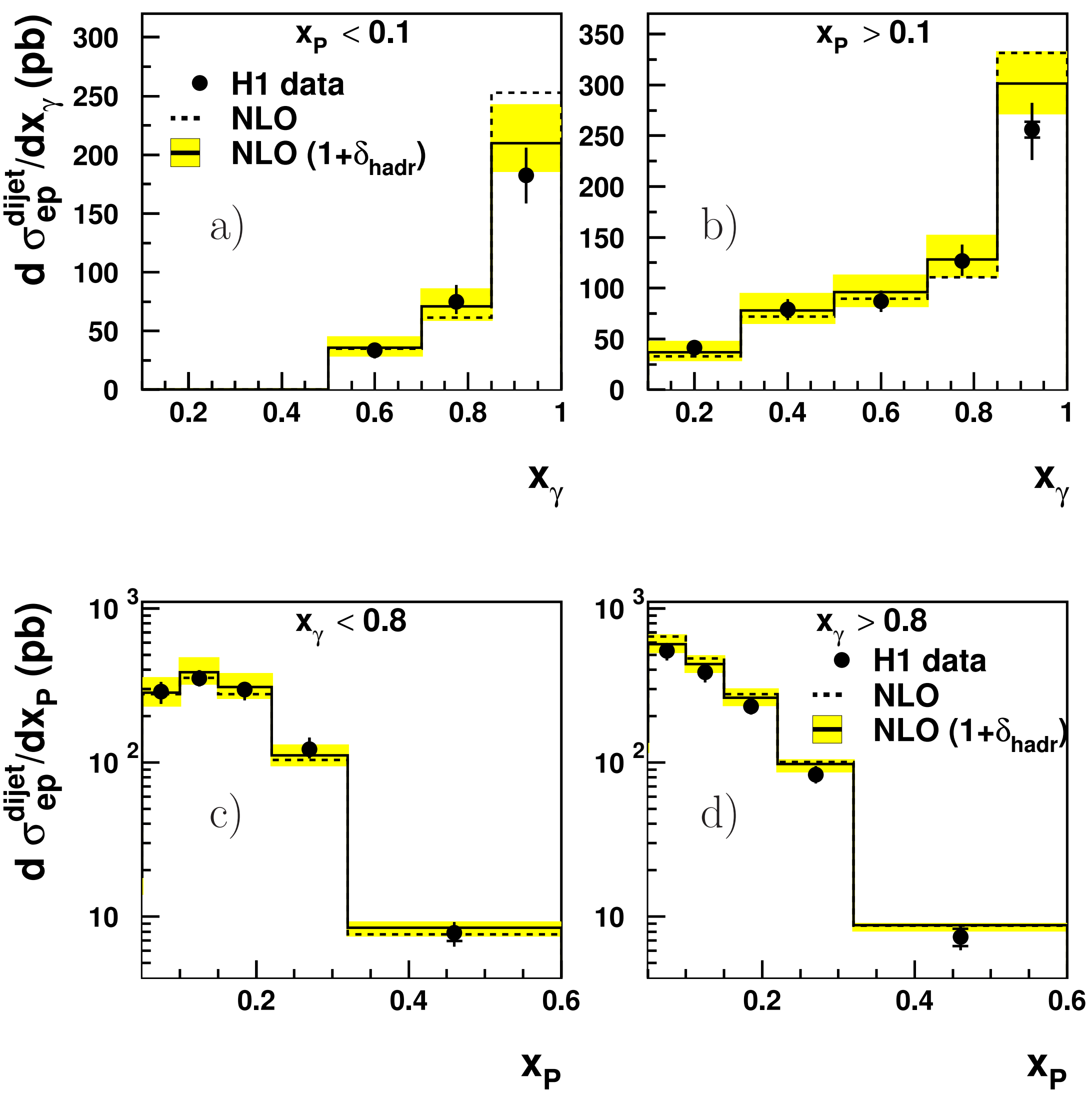

Figure 4.4: *Differential ep cross sections for dijet production ($Q^2 < 1\mathrm{GeV}^2$) as a function of x_γ a) and b) and x_p c) and d). Figures a) and b) distinguish regions of small and large x_p and figures c) and d) corresponding regions in x_γ. NLO predictions using CTEQ5M pdfs for the proton and GRV-HO pdfs for the photon are shown as a dashed line. The full line shows the NLO predictions, including hadronization corrections and the grey band indicates the renormalization and factorization scale uncertainties of the NLO prediction.*

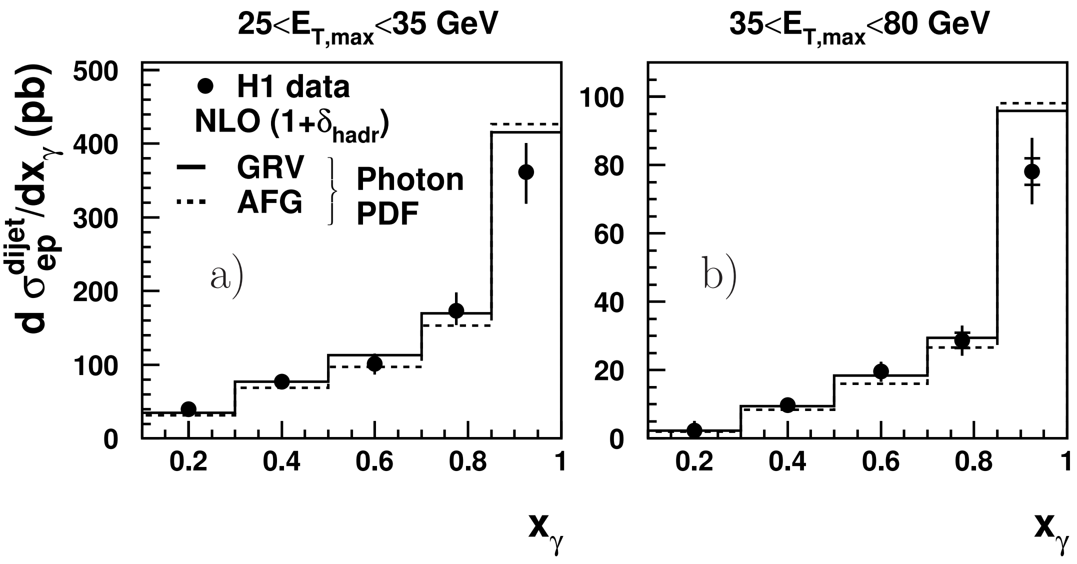

Figure 4.5: *Differential ep cross sections for dijet production ($Q^2 < 1 GeV^2$) as a function of x_γ for a) low $E_{T,max}$ and b) high $E_{T,max}$. The NLO predictions using CTEQ5M pdfs for the proton and GRV-HO pdfs for the photon and including hadronization corrections are shown as a full line. NLO predictions using AFG-HO parametrizations of the photon pdfs and including hadronization corrections are shown as the dashed line.*

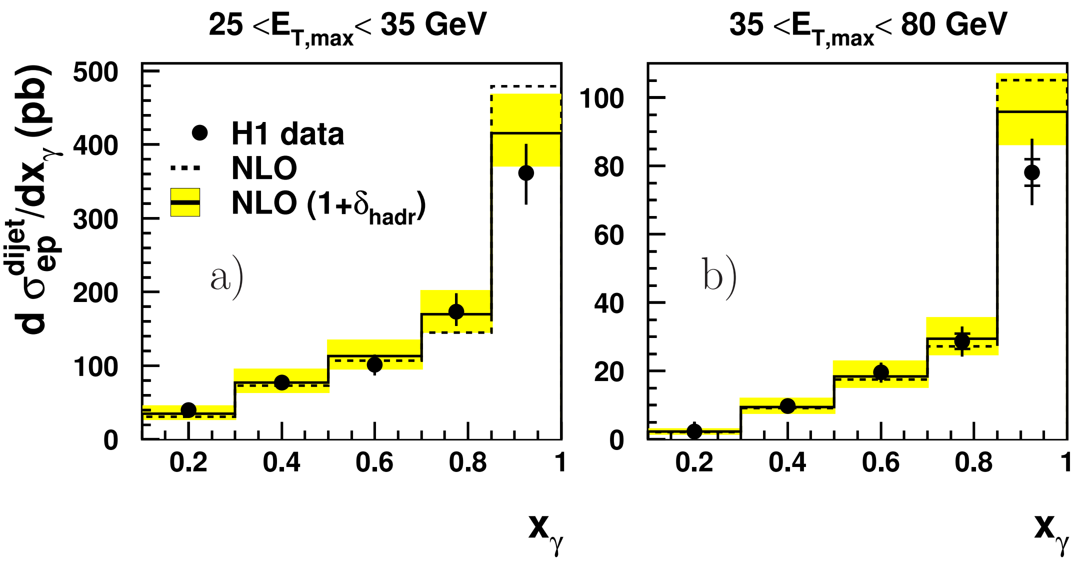

Figure 4.6: *Differential ep cross sections for dijet production ($Q^2 < 1 GeV^2$) as a function of x_γ for a) low $E_{T,max}$ and b) high $E_{T,max}$. NLO predictions using CTEQ5M pdfs for the proton and GRV-HO pdfs for the photon are shown as a dashed line. The full line shows the NLO predictions, including hadronization corrections and the grey band indicates the renormalization and factorization scale uncertainties of the NLO prediction.*

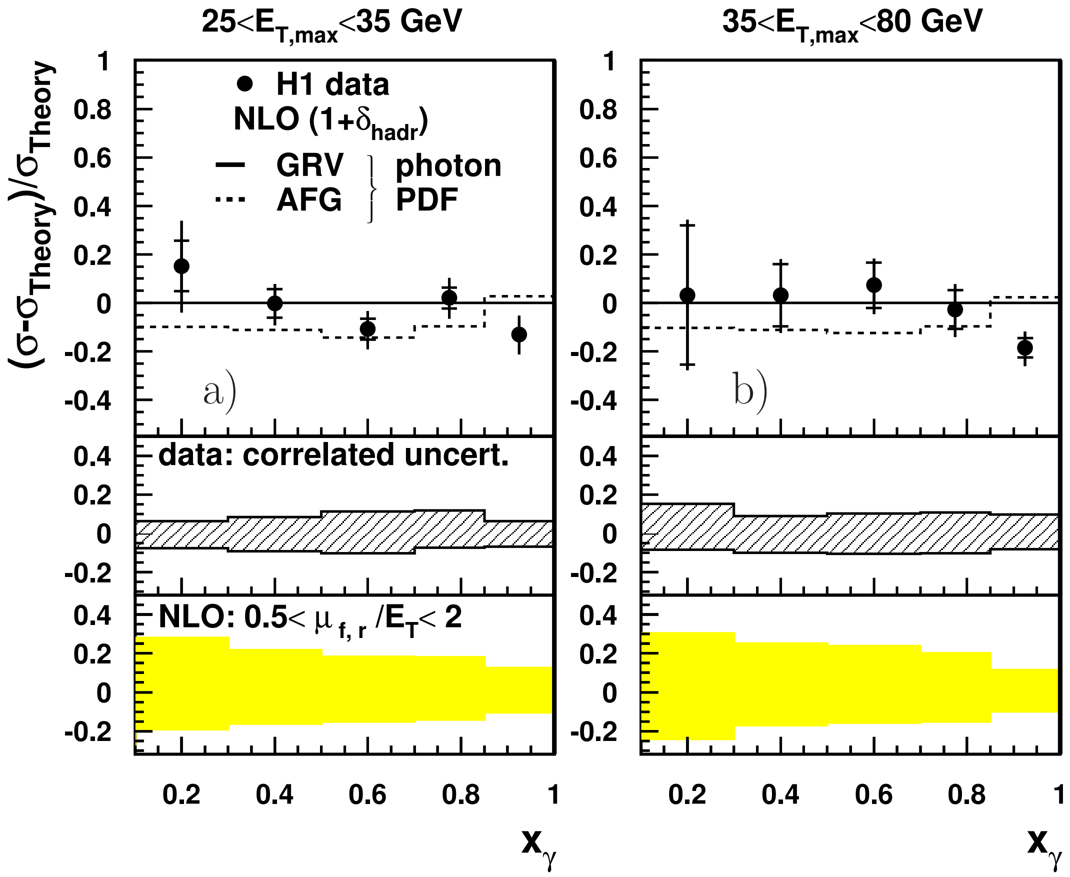

Figure 4.7: *The x_γ dependence of the relative difference of the measured dijet cross sections ($Q^2 < 1GeV^2$) from the NLO prediction, with hadronization corrections applied using CTEQ5M pdfs for the proton and GRV-HO pdfs for the photon (here σ_{Theory}). The symbol σ stands for $d\sigma/dx_\gamma$. Shown is the relative difference of the data (points) and the NLO predictions using the AFG-HO pdf (dashed line) with hadronization corrections applied. Figures a) and b) show the relative difference for the lower $E_{T,max}$ and higher $E_{T,max}$ regions respectively. The inner error bars denote the statistical error, the outer error bars denote all statistical and uncorrelated systematic errors of the data added in quadrature. The correlated systematic errors are shown in the middle plots as a shaded band. The grey band (lower plots) shows the renormalization and factorization scale uncertainties of this NLO prediction.*

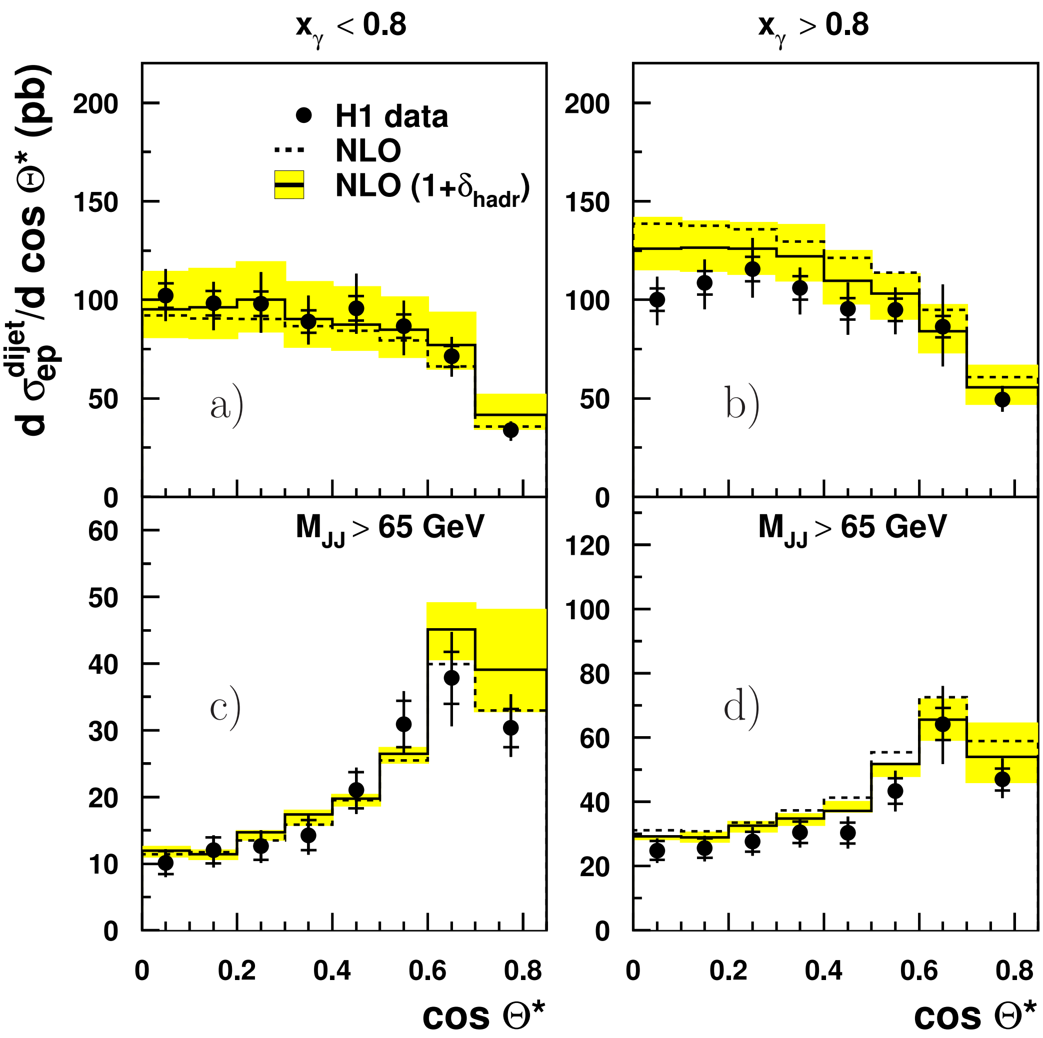

Figure 4.8: *Differential ep cross sections for dijet production ($Q^2 < 1\mathrm{GeV}^2$) as a function of $\cos\theta^*$ distinguished for small x_γ a) and c) and large x_γ b) and d). Figures c) and d) show the cross sections for large invariant masses of the dijet system. NLO predictions using CTEQ5M pdfs for the proton and GRV-HO pdfs for the photon are shown as a dashed line. The full line shows the NLO predictions, including hadronization corrections and the grey band indicates the renormalization and factorization scale uncertainties of the NLO prediction.*

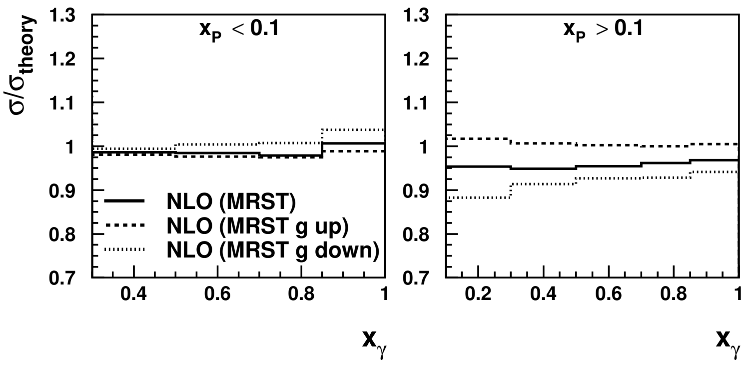

Figure 4.9: *Ratio of the NLO ep cross section for dijet production obtained with different MRST proton pdfs to the NLO cross section obtained with the standard setting as described in section 2.7 (here σ_{theory}) as a function of x_γ.*

again demonstrates that the data are described by NLO QCD up to the highest $E_{T,max}$ values within errors. The NLO scale uncertainty is not reduced significantly with increasing $E_{T,max}$. The cross sections differential in transverse energy are hardly altered by hadronization corrections which are around 5% for all bins. The NLO QCD calculation with hadronization corrections predicts the measured cross sections up to the highest masses and transverse energies, although the photon and proton pdfs have been extracted from quite different processes and mostly at lower scales.

To further explore the photon and proton structure the differential cross section $d\sigma/d\overline{\eta}$ is displayed in Figure 4.3 for two ranges of $E_{T,max}$ subdivided into two y regions. While the former implies a variation of the scale the latter corresponds to different centre-of-mass energies in the photon-proton system. Again, good agreement between data and NLO QCD is observed taking into account the uncertainties in the calculations and in the data points. The predictions tend to lie above the data at low $\overline{\eta}$, where direct interactions dominate and hadronization corrections are largest. At high $\overline{\eta}$, where in contrast resolved interactions dominate and hadronization corrections are small, the NLO QCD predictions agree well with the measured data.

Figures 4.4a) and b) show the dijet cross section $d\sigma/dx_\gamma$ as a function of x_γ for two different x_p regions. The calculations exceed the data, while remaining within the given uncertainties, only for $x_\gamma > 0.85$, where the largest hadronization correction occur. Using the MRST99 1-3 proton pdfs (with a large variation of the high x_p gluon density) instead of CTEQ5M results in differences of less than 5% for the predicted cross section for $x_p < 0.1$ and up to 15% for $x_p > 0.1$ (see Figure 4.9 and 4.10). This is smaller than the scale uncertainties for $x_p < 0.1$ and of the same order for $x_p > 0.1$. These findings are corroborated in Figures 4.4c) and d) where the cross section $d\sigma/dx_p$

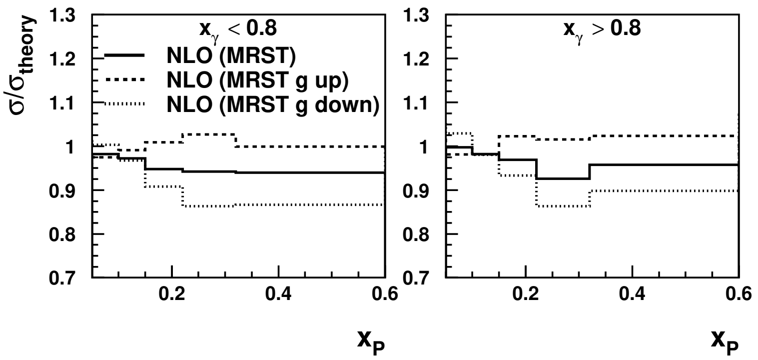

Figure 4.10: *Ratio of the NLO ep cross section for dijet production obtained with different MRST proton pdfs to the NLO cross section obtained with the standard setting as described in section 2.7 (here σ_{theory}) as a function of x_p.*

is shown as a function of x_p for two different x_γ regions. Even at the highest x_p the measured cross sections are seen to agree well with the QCD predictions, which in this part of the phase space attribute about 40% of the cross section to processes induced by gluons in the proton. The constraints on the pdfs used in the QCD calculations here come dominantly from deeply inelastic scattering at lower scales where the gluon fraction is smaller. The concept of universal pdfs in hard processes in QCD is thus observed to describe measurements with rather different experimental conditions.

Figure 4.5 displays the dijet cross sections $d\sigma/dx_\gamma$ as a function of x_γ for two regions of $E_{T,max}$, representing different factorization scales for the photon and proton pdfs. The data are compared to NLO calculations corrected for hadronization effects with two different parameterizations of the photon structure. The predictions describe the data well and vary only slightly with the photon pdfs used. In contrast the NLO scale uncertainties produce a significant effect as can be inferred from Figure 4.6, which repeats the data of Figure 4.5 with a comparison of the GRV-HO pdfs of the photon. For high values of x_γ the hadronization corrections are sizeable and improve the agreement with the data. A more detailed comparison between data and theory is obtained by plotting their relative difference as shown in Figure 4.7. NLO predictions including hadronization corrections are shown for both sets of photon pdfs. At variance to the previous plots the error bars of the data contain only the uncorrelated systematic errors, while the correlated errors due to the uncertainty in the calorimeter energy scales are shown as a hatched band. Figure 4.7 shows that the assumed NLO scale uncertainties are the dominant source of uncertainties in the comparison of data and theory. The expectation exceeds the data only for the high x_γ and high $E_{T,max}$ regions. Within these uncertainties the picture of an universal

photon structure is thus corroborated.
Finally, the dijet cross section $d\sigma/d\cos\theta^*$ is plotted in Figures 4.8a) and b) for $x_\gamma < 0.8$ and $x_\gamma > 0.8$ respectively. The cross section decreases with increasing $\cos\theta^*$ mainly because of the cuts in E_T. Again, the data are well described by NLO QCD for low x_γ, whereas at higher x_γ the predictions overshoot the data for small values of $\cos\theta^*$. These cross sections are also shown with a cut on the invariant mass M_{JJ} of the dijet system in Figures 4.8c) and d), essentially excluding the first bin of Figure 4.1. The cut reduces the restriction of the phase space due to the correlation with the E_T requirements and changes the shape of the distribution towards that expected from the QCD matrix elements. The QCD calculations reproduce this transition nicely in both x_γ regions where resolved and direct photon induced processes contribute with different weights.

4.2 Measurement of three-jet Cross Sections

Likewise the measured cross sections for inclusive 3-jet production in the reaction $ep \to e\,\mathrm{jet\,jet\,jet}\,X$ are corrected for detector effects and are presented at the level of stable hadrons for the phase space region defined in Table 2.1.
Since next-to-leading order 3-jet cross sections have not been calculated yet, the data is compared to LO QCD predictions. They are obtained with the standard setting described in section 2.7, which especially means that a NLO photon and proton pdf (GRV-HO and CTEQ5M) is used and α_s is evolved according to the 2-loop solution. In addition the prediction of this LO calculation corrected for hadronization effects LO$(1+\delta_{hadr})$ and PYTHIA are also shown. Note, that in PYTHIA the third jet is produced by parton showers.
Leading order predictions lead to large renormalization and factorization scale uncertainties. The scale uncertainty is estimated as before by varying all factorization and renormalization scales by 2 and 0.5 times the default scale. The scale uncertainties are found to be about $+40/-30$ % and increase with decreasing x_γ^3. This confirms the finding in the dijet analysis that the scale uncertainties are higher for low x_γ.
Figure 4.11 shows the 3-jet cross section as a function of the invariant 3-jet mass M_{JJJ}. The data covers M_{JJJ} values up to 170 GeV for the last bin center and the total uncertainty in the data ranges from $15-50$ %.
While PYTHIA is able to describe these cross sections for all M_{JJJ} regions, the LO calculation underestimates the cross sections at low M_{JJJ} values by ≈ 40 %. This difference can not be explained by hadronization corrections, which are found to be ≈ 10 %. Nevertheless the data are at the upper edge of the derived scale uncertainties. These results are supported by the 3-jet cross sections as a function of the invariant

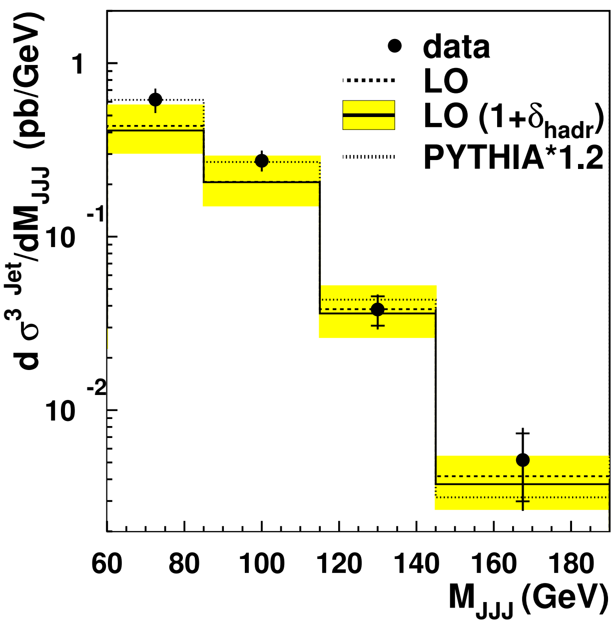

Figure 4.11: *Differential ep cross section for 3-jet production ($Q^2 < 1\mathrm{GeV}^2$) as a function of the invariant 3-jet mass M_{JJJ} of the three highest E_T jets. Here, as well as in the following figures unless explicitly stated otherwise, the inner error bars denote the statistical error, the outer error bars the total uncertainties of the data. The LO predictions using CTEQ5M pdfs for the proton and GRV-HO pdfs for the photon are shown as a dashed line. The full line shows the LO predictions, including hadronization corrections and the grey band indicates the renormalization and factorization scale uncertainties of the LO prediction.*

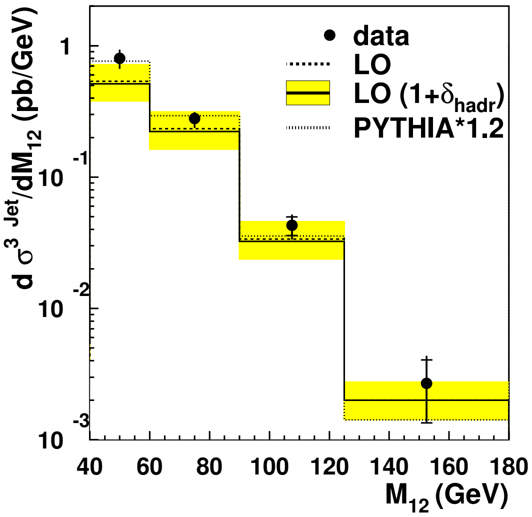

Figure 4.12: *Differential ep cross section for 3-jet production ($Q^2 < 1 GeV^2$) as a function of the invariant mass of the first and second jet M_{12}. The LO predictions using CTEQ5M pdfs for the proton and GRV-HO pdfs for the photon are shown as a dashed line. The full line shows the LO predictions, including hadronization corrections and the grey band indicates the renormalization and factorization scale uncertainties of the LO prediction.*

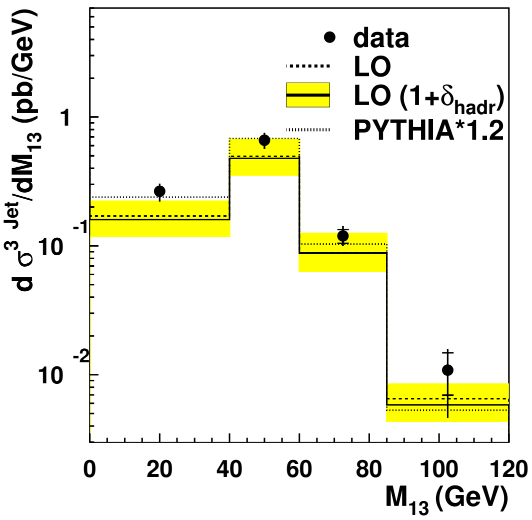

Figure 4.13: *Differential ep cross section for 3-jet production ($Q^2 < 1 GeV^2$) as a function of the invariant mass of the first and third jet M_{13}. The LO predictions using CTEQ5M pdfs for the proton and GRV-HO pdfs for the photon are shown as a dashed line. The full line shows the LO predictions, including hadronization corrections and the grey band indicates the renormalization and factorization scale uncertainties of the LO prediction.*

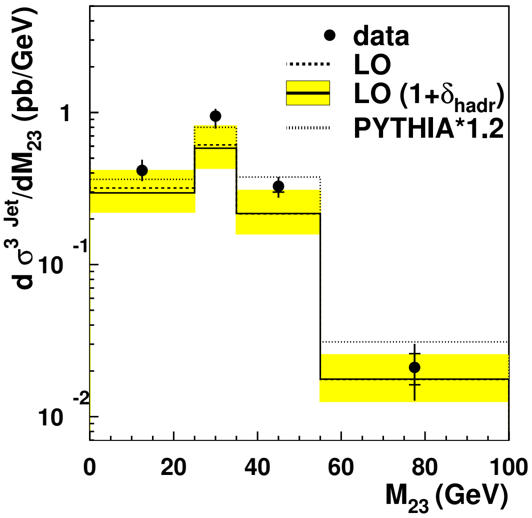

Figure 4.14: *Differential ep cross section for 3-jet production ($Q^2 < 1GeV^2$) as a function of the invariant mass of the second and third jet M_{23}. The LO predictions using CTEQ5M pdfs for the proton and GRV-HO pdfs for the photon are shown as a dashed line. The full line shows the LO predictions, including hadronization corrections and the grey band indicates the renormalization and factorization scale uncertainties of the LO prediction.*

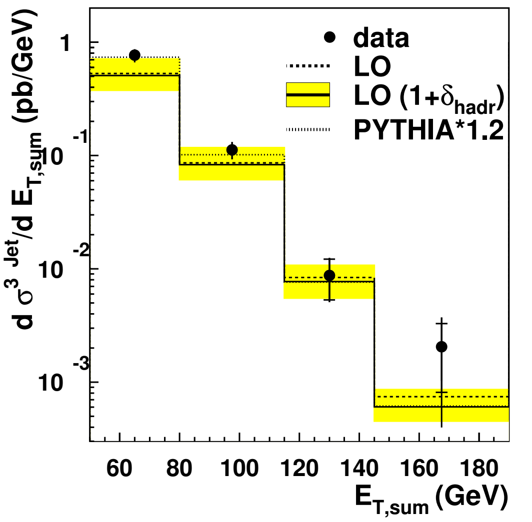

Figure 4.15: *Differential ep cross section for 3-jet production ($Q^2 < 1GeV^2$) as a function of the sum of the transverse energies of the three jets $E_{T,sum}$. The LO predictions using CTEQ5M pdfs for the proton and GRV-HO pdfs for the photon are shown as a dashed line. The full line shows the LO predictions, including hadronization corrections and the grey band indicates the renormalization and factorization scale uncertainties of the LO prediction.*

mass of the first and second jet M_{12} (Figure 4.12), of the first and third jet M_{13} (Figure 4.13) and the second and third jet M_{23} (Figure 4.14). Especially at low invariant mass the LO predictions undershoots the data, while PYTHIA better describes the shape of the data. The data cross sections as functions of these observables have uncertainties of $15-60$ % and increase with increasing masses. The LO predictions are again hardly altered by hadronization corrections.

These cross sections are also important as a possible background to various new physics signals. A new massive particle (e.g. a top quark), which could explain the deviations reported in section 2.8.2, would correspond to a 3-jet event with a high invariant mass configuration. No deviations of the data to the predictions are observed in one of the mass distributions.

Furthermore the 3-jet cross section as a function of the sum of the transverse energies of the three jets $E_{T,sum}$ is measured as shown in Figure 4.15. Up to $E_{T,sum} \approx 170$ GeV the data is compatible with the predictions taking into account uncertainties.

To test the power of the predictions for the third jet, the 3-jet cross section as a function of the transverse energy of the third jet $E_{T,third}$ is measured. Figure 4.16 shows that the third jet reaches E_T values up to ≈ 35 GeV and that the data is again higher than the LO prediction, but described within errors.

The observed 3-jet cross section as a function of $d\sigma/d\overline{\eta}$ is shown in Figure 4.17. As in the dijet case the low $\overline{\eta}$ region is dominated by direct events. However, in the high $\overline{\eta}$ region resolved and direct events enter with similar weights. The LO QCD calculation describes the data at low $\overline{\eta}$. For $\overline{\eta} > 1$ the data is a factor of ≈ 1.7 higher than the LO calculation. At high $\overline{\eta}$ hadronization corrections are very small.

The disagreement of the data with the LO calculation at low invariant mass and high $\overline{\eta}$ is likely due to a disagreement of the resolved part between data and theory.

To explore the resolved region the 3-jet cross section is presented as a function of $x_\gamma^{(2)}$ in Figure 4.18 and $x_\gamma^{(3)}$ in Figure 4.19.

As explained in section 2.3 the 3-jet cross section as a function of $x_\gamma^{(2)}$ tests the rate of low x_γ dijet events, which have a third high E_T jet. Comparing Figure 4.18 and Figure 4.6 about 40 % of the dijet events with $x_\gamma < 0.3$ and 30 % with $x_\gamma < 0.7$ contain a third high E_T jet. At $x_\gamma > 0.85$ this fraction is ≈ 5 %.

The LO calculation is not able to describe the data, while the prediction of this LO calculation corrected for hadronization is satisfactory at high x_γ. Hadronization corrections are largest in this region. For low x_γ the data is always higher than the LO prediction.

These arguments hold for the 3-jet cross section as a function of $x_\gamma^{(3)}$. While at high $x_\gamma^{(3)}$ agreement within errors between data and the LO calculation is found, the LO calculation is not able to describe the data at low $x_\gamma^{(3)}$ values. For $x_\gamma^{(3)} < 0.85$ the

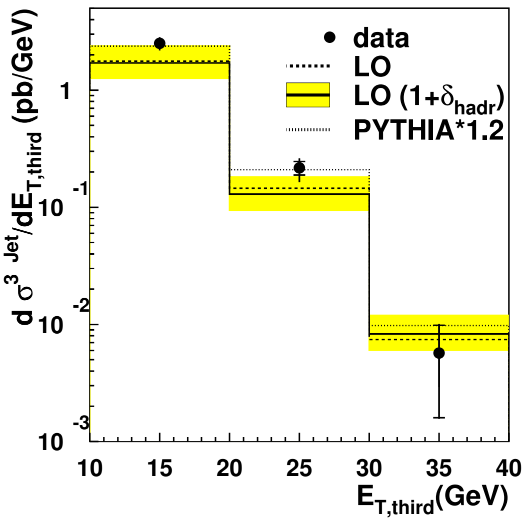

Figure 4.16: *Differential ep cross section for 3-jet production ($Q^2 < 1GeV^2$) as a function of the transverse energy of the third jet $E_{T,third}$. The LO predictions using CTEQ5M pdfs for the proton and GRV-HO pdfs for the photon are shown as a dashed line. The full line shows the LO predictions, including hadronization corrections and the grey band indicates the renormalization and factorization scale uncertainties of the LO prediction.*

measured cross sections are a factor of $2-3$ higher than the LO calculation. Here hadronization corrections are found to be small ($10-15\%$).
The Pythia model gives an adequate description of the shape of all tested 3-jet observables (similar is found for the HERWIG model as presented in chapter 3).

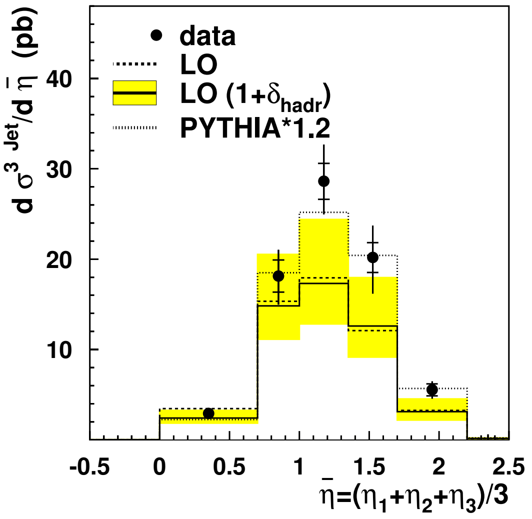

Figure 4.17: *Differential ep cross section for 3-jet production ($Q^2 < 1 GeV^2$) as a function of the mean pseudorapidity of the three jets $\overline{\eta}$. The LO predictions using CTEQ5M pdfs for the proton and GRV-HO pdfs for the photon are shown as a dashed line. The full line shows the LO predictions, including hadronization corrections and the grey band indicates the renormalization and factorization scale uncertainties of the LO prediction.*

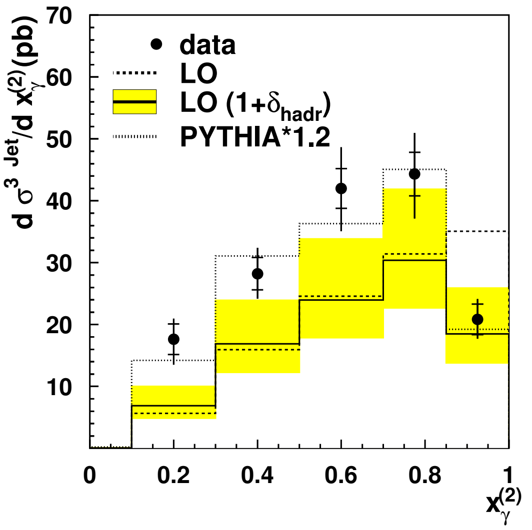

Figure 4.18: *Differential ep cross section for 3-jet production ($Q^2 < 1 GeV^2$) as a function of the sum of $x_\gamma^{(2)}$. The LO predictions using CTEQ5M pdfs for the proton and GRV-HO pdfs for the photon are shown as a dashed line. The full line shows the LO predictions, including hadronization corrections and the grey band indicates the renormalization and factorization scale uncertainties of the LO prediction.*

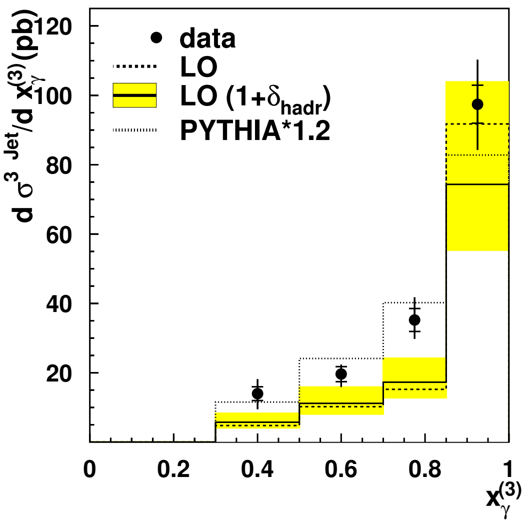

Figure 4.19: *Differential ep cross section for 3-jet production ($Q^2 < 1\mathrm{GeV}^2$) as a function of the sum of $x_\gamma^{(3)}$. The LO predictions using CTEQ5M pdfs for the proton and GRV-HO pdfs for the photon are shown as a dashed line. The full line shows the LO predictions, including hadronization corrections and the grey band indicates the renormalization and factorization scale uncertainties of the LO prediction.*

5

Conclusions and Outlook

New measurements of dijet and 3-jet cross sections in photoproduction at high transverse energies are presented for various jet kinematic observables. Furthermore a decrease of systematic errors and a detailed comparison to reliable leading and next-to-leading order calculations was achieved. This significantly improves the understanding of jet physics in photoproduction.

Dijet Measurements

The dijet measurements cover invariant dijet masses up to 160 GeV and transverse energies up to 80 GeV, reaching x_p and x_γ values where the experimental information was previously limited. In this kinematic domain non-perturbative effects like multiple interactions and hadronization are found to be small, which allows a direct comparison of NLO QCD calculations with the data to be made. The results demonstrate the power of perturbative QCD in predicting the measured cross sections in a wide kinematical range. Even though the photon pdfs have been obtained from measurements at lower scales, their QCD evolution correctly reproduces the data at high scales. The data do not require significant changes in the parameterizations of the pdfs but are certainly useful to further constrain the existing ones. Likewise our understanding of the proton structure in the high x_p, high scale region can be improved with the help of these data.

Three-jet Measurements

The 3-jet measurements cover invariant 3-jet masses up to 175 GeV and transverse energies of the third jet up to 40 GeV. The parton shower model in PYTHIA gave a satisfactory description of all tested 3-jet observables. HERWIG was not able to describe all quantities sensitive to multijet production, e.g. the rate of 3-jet to dijet events, but gave for most observables an adequate description.

Leading order calculations were found to be too low to describe the data at low invariant masses, high $\overline{\eta}$ and low x_γ. The difference between data and the LO calculations could not be explained by the high scale uncertainties or hadronization effects.

Outlook

A future stronger constraint of parton densities requires a reduction of both the theoretical scale uncertainties and the systematic uncertainties in the data.
The large luminosity expected after the HERA luminosity upgrade will allow a reduction of the data uncertainties. Furthermore the increase of the proton beam energy allows the study of jets up to transverse energies of 100 GeV. This will be especially helpful to constrain the proton pdfs in the high x_P regime.
A particularly suitable choice of cuts on the jet transverse momenta may reduce theoretical uncertainties. This can be suggested by the small uncertainties found at high $E_{T,mean}$.
Next-to-leading order calculations for 3-jet observables would significantly improve the interpretation of these events.

A
Data Tables

M_{JJ} (GeV)	$\frac{d\sigma^{dijets}}{dM_{JJ}}$ (pb/GeV)	$\delta_{stat}(\%)$	$+\delta_{tot}(\%)$	$-\delta_{tot}(\%)$	$+\delta_E(\%)$	$-\delta_E(\%)$
45.-57.5	4.30	2.5	13	14	8	8
57.5-70.	3.69	2.9	11	11	9	8
70.-90.	1.33	3.7	13	11	11	8
90.-110.	0.39	6.9	12	16	8	12
110.-135.	0.101	12.	19	18	13	11
135.-180.	0.0102	27.1	32	30	14	9
$E_{T,mean}$ (GeV)	$\frac{d\sigma^{dijets}}{dE_{T,mean}}$ (pb/GeV)	$\delta_{stat}(\%)$	$+\delta_{tot}(\%)$	$-\delta_{tot}(\%)$	$+\delta_E(\%)$	$-\delta_E(\%)$
20.-30.	10.65	1.8	12	12	9	8
30.-45.	2.41	3.1	12	11	10	8
45.-60.	0.166	11.6	16	17	10	11
60.-80	0.0192	29.2	37	34	22	16
$E_{T,max}$ (GeV)	$\frac{d\sigma^{dijets}}{dE_{T,max}}$ (pb/GeV)	$\delta_{stat}(\%)$	$+\delta_{tot}(\%)$	$-\delta_{tot}(\%)$	$+\delta_E(\%)$	$-\delta_E(\%)$
25.-35.	12.36	1.8	11	12	9	8
35.-45.	1.82	3.9	12	12	9	9
45.-60.	0.252	8.4	15	15	11	11
60.-80.	0.0198	27.4	33	32	17	15

Table A.1: *Differential ep cross sections for dijet production as a function of the invariant dijet mass M_{JJ} (upper table), as a function of $E_{T,mean}$ (middle table) and as a function of $E_{T,max}$ (lower table) with statistical and total upper and lower uncertainties (cf. Figures 4.1 and 4.2). Seperatly listed is the error δ_E due to the energy scale uncertainty of the LAr calorimeter.*

$\overline{\eta}$	$\frac{d\sigma^{dijets}}{d\overline{\eta}}$ (pb)	$\delta_{stat}(\%)$	$+\delta_{tot}(\%)$	$-\delta_{tot}(\%)$	$+\delta_E(\%)$	$-\delta_E(\%)$
	$0.1 < y < 0.5$ and $25 < E_{T,max} < 35$ GeV					
0.6-0.9	7.55	10.0	20	22	7	11
0.9-1.3	42.2	4.4	11	15	7	12
1.3-1.7	52.2	4.2	10	11	7	8
1.7-2.1	31.8	5.4	12	11	10	7
2.1-2.5	10.3	10.1	17	18	10	10
	$0.1 < y < 0.5$ and $35 < E_{T,max} < 80$ GeV					
0.9-1.3	2.57	14.0	20	20	8	9
1.3-1.7	10.2	8.0	14	13	10	8
1.7-2.1	6.80	9.9	14	16	9	11
2.1-2.5	1.47	21.0	24	24	9	10
	$0.5 < y < 0.9$ and $25 < E_{T,max} < 35$ GeV					
0.0-0.6	27.9	4.7	17	14	11	6
0.6-0.9	66.4	4.5	13	13	9	8
0.9-1.3	43.9	4.9	14	11	11	6
1.3-1.7	20.8	7.4	13	16	10	13
1.7-2.1	10.2	11.7	14	14	6	4
2.1-2.5	2.75	24.8	30	29	9	3
	$0.5 < y < 0.9$ and $35 < E_{T,max} < 80$ GeV					
0.6-0.9	9.77	9.7	20	20	10	11
0.9-1.3	14.14	7.5	13	13	10	8
1.3-1.7	9.12	9.3	15	15	10	9
1.7-2.1	2.59	18.1	24	24	13	13

Table A.2: *Differential ep cross sections for dijet production as a function of $\overline{\eta}$ with statistical and total upper and lower uncertainties (cf. Figure 4.3). Seperatly listed is the error δ_E due to the energy scale uncertainty of the LAr calorimeter.*

x_γ	$\frac{d\sigma^{dijets}}{dx_\gamma}$ (pb)	$\delta_{stat}(\%)$	$+\delta_{tot}(\%)$	$-\delta_{tot}(\%)$	$+\delta_E(\%)$	$-\delta_E(\%)$
	$x_p < 0.1$					
0.5-0.7	33.5	7.5	20	20	15	15
0.7-0.85	75.0	5.8	19	14	15	7
0.85-1.	182.7	3.3	13	13	7	6
	$x_p > 0.1$					
0.1-0.3	41.4	8.0	15	16	7	8
0.3-0.5	78.9	5.1	13	13	10	10
0.5-0.7	87.2	4.5	12	12	10	9
0.7-0.85	126.8	4.3	12	12	10	8
0.85-1	256.1	3.0	10	12	8	8

Table A.3: *Differential ep cross sections for dijet production as a function of x_γ with statistical and total upper and lower uncertainties (cf. Figure 4.4). Seperatly listed is the error δ_E due to the energy scale uncertainty of the LAr calorimeter.*

x_p	$\frac{d\sigma^{dijets}}{dx_p}$ (pb)	$\delta_{stat}(\%)$	$+\delta_{tot}(\%)$	$-\delta_{tot}(\%)$	$+\delta_E(\%)$	$-\delta_E(\%)$
	$x_\gamma < 0.8$					
0.05-0.1	288.0	5.3	15	17	8	10
0.1-0.15	352.1	4.8	13	11	9	5
0.15-0.22	298.6	4.4	9	15	5	12
0.22-0.32	121.8	5.6	19	12	17	9
0.32-0.6	7.86	11.8	17	19	11	13
	$x_\gamma > 0.8$					
0.05-0.1	530.0	3.5	12	14	7	9
0.1-0.15	384.4	4.3	12	14	8	9
0.15-0.22	232.1	4.7	11	12	8	8
0.22-0.32	83.7	6.5	13	13	10	9
0.32-0.6	7.4	12.7	19	18	12	11

Table A.4: *Differential ep cross sections for dijet production as a function of x_p with statistical and total upper and lower uncertainties (cf. Figure 4.4). Seperatly listed is the error δ_E due to the energy scale uncertainty of the LAr calorimeter.*

x_γ	$\frac{d\sigma^{dijets}}{dx_\gamma}$ (pb)	$\delta_{stat}(\%)$	$+\delta_{tot}(\%)$	$-\delta_{tot}(\%)$	$+\delta_E(\%)$	$-\delta_E(\%)$
	$25 < E_{T,max} < 35$ GeV					
0.1-0.3	40.1	8.4	17	18	7	8
0.3-0.5	77.3	5.3	11	13	8	9
0.5-0.7	101.1	4.3	14	14	11	11
0.7-0.85	173.6	3.9	14	11	12	8
0.85-1.	361.7	2.5	11	12	7	7
	$35 < E_{T,max} < 80$ GeV					
0.1-0.3	2.34	27.5	34	31	16	9
0.3-0.5	9.83	12.1	17	18	9	10
0.5-0.7	19.7	8.5	14	15	10	11
0.7-0.85	28.7	8.0	15	16	11	10
0.85-1.	78.1	4.9	13	12	10	8

Table A.5: *Differential ep cross sections for dijet production as a function of x_γ with statistical and total upper and lower uncertainties (cf. Figures 4.5, 4.6 and 4.7). Seperatly listed is the error δ_E due to the energy scale uncertainty of the LAr calorimeter.*

$\cos\theta^*$	$\frac{d\sigma^{dijets}}{d\cos\theta^*}$ (pb)	$\delta_{stat}(\%)$	$+\delta_{tot}(\%)$	$-\delta_{tot}(\%)$	$+\delta_E(\%)$	$-\delta_E(\%)$
	$x_\gamma < 0.8$					
0.0-0.1	102.0	6.1	13	13	10	8
0.1-0.2	98.3	6.3	11	14	6	10
0.2-0.3	98.0	6.4	16	15	14	12
0.3-0.4	89.0	6.4	15	13	11	8
0.4-0.5	95.6	6.5	18	14	14	5
0.5-0.6	86.6	6.8	15	17	9	11
0.6-0.7	71.3	7.5	14	14	10	10
0.7-0.85	33.8	8.8	14	16	9	11
	$x_\gamma > 0.8$					
0.0-0.1	100.1	5.6	12	13	7	8
0.1-0.2	108.6	5.5	11	12	8	9
0.2-0.3	115.6	5.4	14	13	10	7
0.3-0.4	106.1	5.5	10	13	5	8
0.4-0.5	95.7	5.7	14	14	9	7
0.5-0.6	95.0	5.9	12	13	7	8
0.6-0.7	86.3	6.3	25	23	12	7
0.7-0.85	49.5	7.0	14	13	10	7
	$x_\gamma < 0.8$ and $M_{JJ} > 65$ GeV					
0.0-0.1	10.1	17.0	21	21	10	10
0.1-0.2	12.0	16.4	19	21	7	11
0.2-0.3	12.6	16.3	19	20	7	9
0.3-0.4	14.3	15.9	22	21	13	11
0.4-0.5	21.0	12.8	16	17	8	9
0.5-0.6	30.9	11.3	16	14	10	5
0.6-0.7	37.9	10.3	18	19	13	14
0.7-0.85	30.4	9.4	17	14	12	8
	$x_\gamma > 0.8$ and $M_{JJ} > 65$ GeV					
0.0-0.1	24.9	11.7	15	16	7	8
0.1-0.2	25.6	11.9	15	16	7	8
0.2-0.3	27.6	11.3	16	16	10	8
0.3-0.4	30.5	11.0	15	16	8	9
0.4-0.5	30.3	10.9	17	16	10	7
0.5-0.6	43.4	9.2	15	15	9	9
0.6-0.7	64.2	7.7	19	19	6	7
0.7-0.85	47.0	7.4	14	13	10	7

Table A.6: *Differential ep cross sections for dijet production as a function of* $\cos\theta^*$ *with statistical and total upper and lower uncertainties (cf. Figure 4.8). Seperatly listed is the error* δ_E *due to the energy scale uncertainty of the LAr calorimeter.*

B

Hadronization Correction

Hadronization correction functions are defined as the ratio of the cross sections with jets reconstructed from hadrons and from partons before hadronization. These functions give an estimate of the size of the non-perturbative contributions to the cross sections. The contributions are derived using PYTHIA and HERWIG. Until now only models can be considered in which the LO matrix element and the leading logarithmic parton showers are matched with the hadronization model. A consistent treatment for NLO calculations is until now not available.
The correction functions $C_{\text{had}}(i)$ are calculated from the ratio of the cross sections with jets reconstructed from partons after parton showering (parton level) , $\sigma_{\text{par.}}$, to the cross sections with jets reconstructed from hadrons (hadron level), $\sigma_{\text{had.}}$, in each bin, where each sample was subject to the selection criteria:

$$C_{\text{had}}(i) = \frac{\sigma_{\text{par.}}(i)}{\sigma_{\text{had.}}(i)} \quad . \tag{B.1}$$

The mean value of the PYTHIA and HERWIG prediction is used for corrections:

$$C_{had} = (C_{\text{Pythia,had}} + C_{\text{Herwig,had}})/2 \quad . \tag{B.2}$$

The predictions of NLO QCD are corrected for hadronization effects via

$$\sigma_{NLO(1+\delta_{\text{hadr}})} = \sigma_{NLO}/C_{had} \quad . \tag{B.3}$$

The factors C_{had} and half the difference of the two models $\Delta C_{had} = (C_{\text{Pythia,had}} - C_{\text{herwig,had}})/2$ are presented for all dijet cross sections in the Tables B.1, B.2, B.3, B.4, B.5 and B.6.

M_{JJ} (GeV)	C_{had}	ΔC_{had}
45.-57.5	1.03	0.05
57.5-70.	1.01	-0.001
70.-90.	1.03	-0.002
90.-110.	1.01	0.02
110.-135.	1.03	0.03
135.-180.	1.03	0.01
$E_{T,mean}$ (GeV)	C_{had}	ΔC_{had}
20.-30.	1.01	0.03
30.-45.	1.03	-0.0005
45.-60.	1.02	0.01
60.-80	1.00	0.03
$E_{T,max}$ (GeV)	C_{had}	ΔC_{had}
25.-35.	1.02	0.02
35.-45.	1.02	0.02
45.-60.	1.05	0.03
60.-80.	1.01	0.03

Table B.1: *Hadronization correction C_{had} and model difference ΔC_{had} for dijet production for the analysis bins in the invariant dijet mass M_{JJ} (upper table), in $E_{T,mean}$ (middle table) and in $E_{T,max}$ (lower table).*

$\overline{\eta}$	C_{had}	ΔC_{had}
	$0.1 < y < 0.5$ and $25 < E_{T,max} < 35$ GeV	
0.6-0.9	1.47	-0.07
0.9-1.3	1.07	0.02
1.3-1.7	1.00	0.04
1.7-2.1	0.98	0.05
2.1-2.5	0.90	0.04
	$0.1 < y < 0.5$ and $35 < E_{T,max} < 80$ GeV	
0.9-1.3	1.21	-0.03
1.3-1.7	1.04	0.03
1.7-2.1	1.01	0.02
2.1-2.5	0.96	0.03
	$0.5 < y < 0.9$ and $25 < E_{T,max} < 35$ GeV	
0.0-0.6	1.16	-0.02
0.6-0.9	0.97	0.01
0.9-1.3	0.94	0.05
1.3-1.7	0.92	0.02
1.7-2.1	0.95	0.05
2.1-2.5	0.92	0.02
	$0.5 < y < 0.9$ and $35 < E_{T,max} < 80$ GeV	
0.6-0.9	1.11	-0.03
0.9-1.3	0.97	0.04
1.3-1.7	0.98	0.02
1.7-2.1	0.93	0.04

Table B.2: *Hadronization correction C_{had} and model difference ΔC_{had} for dijet production for the analysis bins in in $\overline{\eta}$.*

x_γ	C_{had}	ΔC_{had}
	$x_p < 0.1$	
0.5-0.7	0.98	0.07
0.7-0.85	0.87	0.08
0.85-1.	1.20	-0.02
	$x_p > 0.1$	
0.1-0.3	0.90	0.03
0.3-0.5	0.92	0.04
0.5-0.7	0.93	0.04
0.7-0.85	0.86	0.04
0.85-1	1.09	0.004

Table B.3: *Hadronization correction C_{had} and model difference ΔC_{had} for dijet production for the analysis bins in x_γ.*

x_p	C_{had}	ΔC_{had}
	$x_\gamma < 0.8$	
0.05-0.1	0.98	0.10
0.1-0.15	0.92	0.03
0.15-0.22	0.90	0.06
0.22-0.32	0.94	0.04
0.32-0.6	0.90	0.05
	$x_\gamma > 0.8$	
0.05-0.1	1.12	-0.006
0.1-0.15	1.09	-0.03
0.15-0.22	1.05	0.02
0.22-0.32	1.03	0.003
0.32-0.6	0.99	0.02

Table B.4: *Hadronization correction C_{had} and model difference ΔC_{had} for dijet production for the analysis bins in x_p.*

x_γ	C_{had}	ΔC_{had}
	$25 < E_{T,max} < 35$ GeV	
0.1-0.3	0.89	0.03
0.3-0.5	0.94	0.06
0.5-0.7	0.94	0.05
0.7-0.85	0.85	0.05
0.85-1.	1.15	-0.01
	$35 < E_{T,max} < 80$ GeV	
0.1-0.3	0.96	0.07
0.3-0.5	0.97	0.03
0.5-0.7	0.95	0.05
0.7-0.85	0.92	0.04
0.85-1.	1.10	0.005

Table B.5: *Hadronization correction C_{had} and model difference ΔC_{had} for dijet production for the analysis bins in in x_γ.*

$\cos\theta^*$	C_{had}	ΔC_{had}
	$x_\gamma < 0.8$	
0.0-0.1	0.97	0.07
0.1-0.2	0.94	0.10
0.2-0.3	0.90	0.03
0.3-0.4	0.96	0.05
0.4-0.5	0.96	0.05
0.5-0.6	0.94	0.05
0.6-0.7	0.86	0.06
0.7-0.85	0.86	0.06
	$x_\gamma > 0.8$	
0.0-0.1	1.10	-0.02
0.1-0.2	1.09	0.01
0.2-0.3	1.08	-0.01
0.3-0.4	1.06	0.02
0.4-0.5	1.10	0.002
0.5-0.6	1.10	-0.004
0.6-0.7	1.13	-0.02
0.7-0.85	1.09	-0.03
	$x_\gamma < 0.8$ and $M_{JJ} > 65$ GeV	
0.0-0.1	0.95	0.04
0.1-0.2	1.03	0.01
0.2-0.3	0.92	0.04
0.3-0.4	0.91	0.03
0.4-0.5	0.99	0.04
0.5-0.6	0.96	-0.02
0.6-0.7	0.88	0.04
0.7-0.85	0.84	0.08
	$x_\gamma > 0.8$ and $M_{JJ} > 65$ GeV	
0.0-0.1	1.07	-0.010
0.1-0.2	1.06	-0.005
0.2-0.3	1.03	-0.019
0.3-0.4	1.07	0.006
0.4-0.5	1.11	-0.02
0.5-0.6	1.07	-0.02
0.6-0.7	1.11	-0.02
0.7-0.85	1.09	-0.02

Table B.6: *Hadronization correction C_{had} and model difference ΔC_{had} for dijet production for the analysis bins in $\cos\theta^*$.*

C

Variation of the cut on $E_{T,second}$

Figure C.1 illustrates how the ratio of the measured cross sections to the theoretical prediction depends on a variation of the cut in $E_{T,second}$ starting at $E_{T,second}$ of 10 GeV for different regions in x_γ. Hadronization corrections are applied to the data. The size of the hadronization correction is small and almost independent of $E_{T,second}$.
With an increasing cut on $E_{T,second}$ the cross section decreases and this decrease is well modelled by PYTHIA for all regions in x_γ. The NLO calculation shows a slightly different slope compared to the data at $x_\gamma < 0.8$. One reason might be the increasing ratio of 3-jet events to 2-jet events with a decreasing cut on $E_{T,second}$ at low x_γ. Events containing a third high E_T jet mostly populate the low x_γ region (see Figure 4.18). Since a dijet NLO calculation is only LO for 3-jet production it is concluded that higher order effects become more and more important with lowering the cut on $E_{T,second}$.
However the ratio of the measured cross sections to the theoretical prediction varies only by up to $\pm 10\%$ for $x_\gamma < 0.8$ and by up to $\pm 3\%$ for $x_\gamma > 0.8$. This difference is smaller than the NLO scale uncertainties.

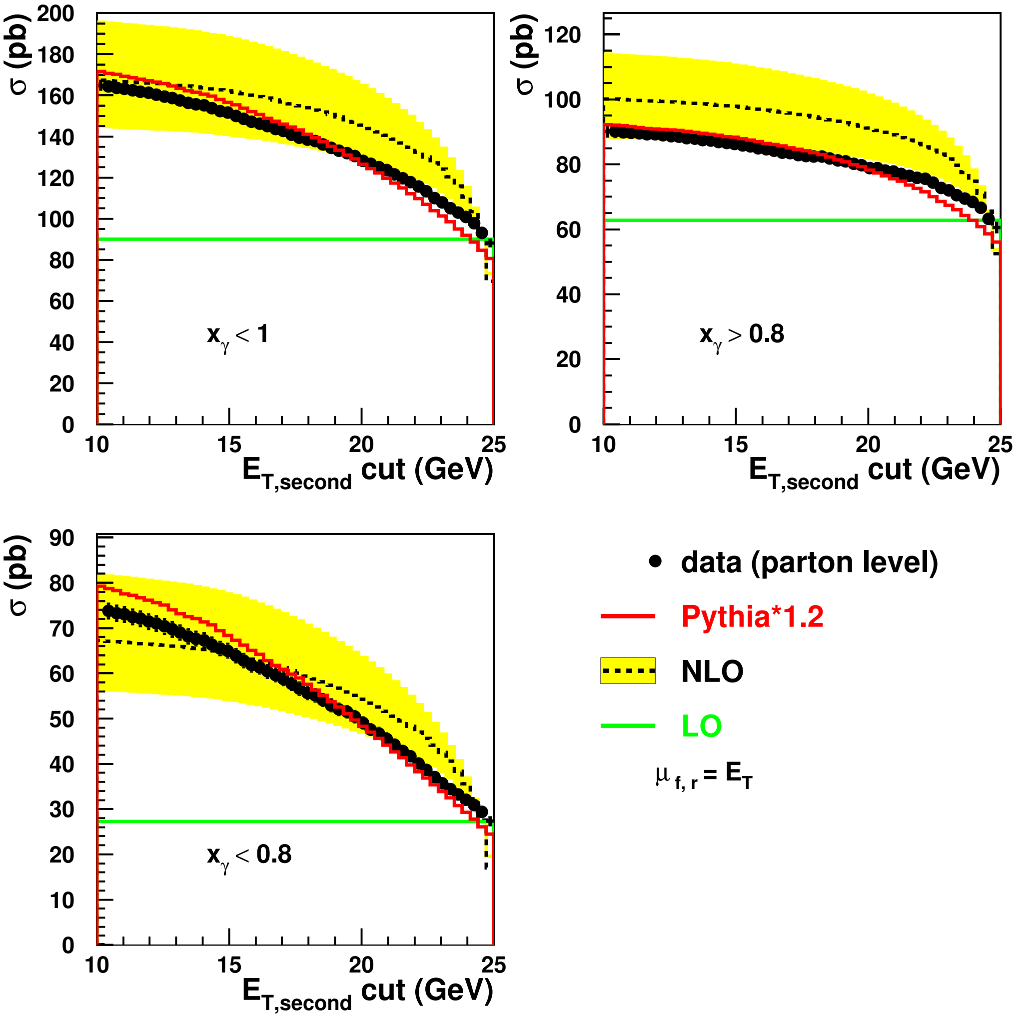

Figure C.1: *The ep cross section for dijet production ($Q^2 < 1GeV^2$) as a function of the cut on the E_T of the second jet $E_{T,second}$cut. The data is corrected for hadronization effects. The LO predictions using CTEQ5M pdfs for the proton and GRV-HO pdfs for the photon are shown as a light grey line. The dotted line shows the NLO predictions and the grey band indicates the renormalization and factorization scale uncertainties of the NLO prediction. The dark grey line shows the PYTHIA prediction.*

D

Check of the jet resolution

It is verified that the jet E_T resolution, as implemented with the detector simulation in PYTHIA and HERWIG, is able to reproduce the width of the E_T balance distributions. This is proven as a function of the pseudorapidity of the leading jet η_{jet1} as illustrated in Figure D.1. It is found that the jet energy resolution in the data is well reproduced by the detector simulation.

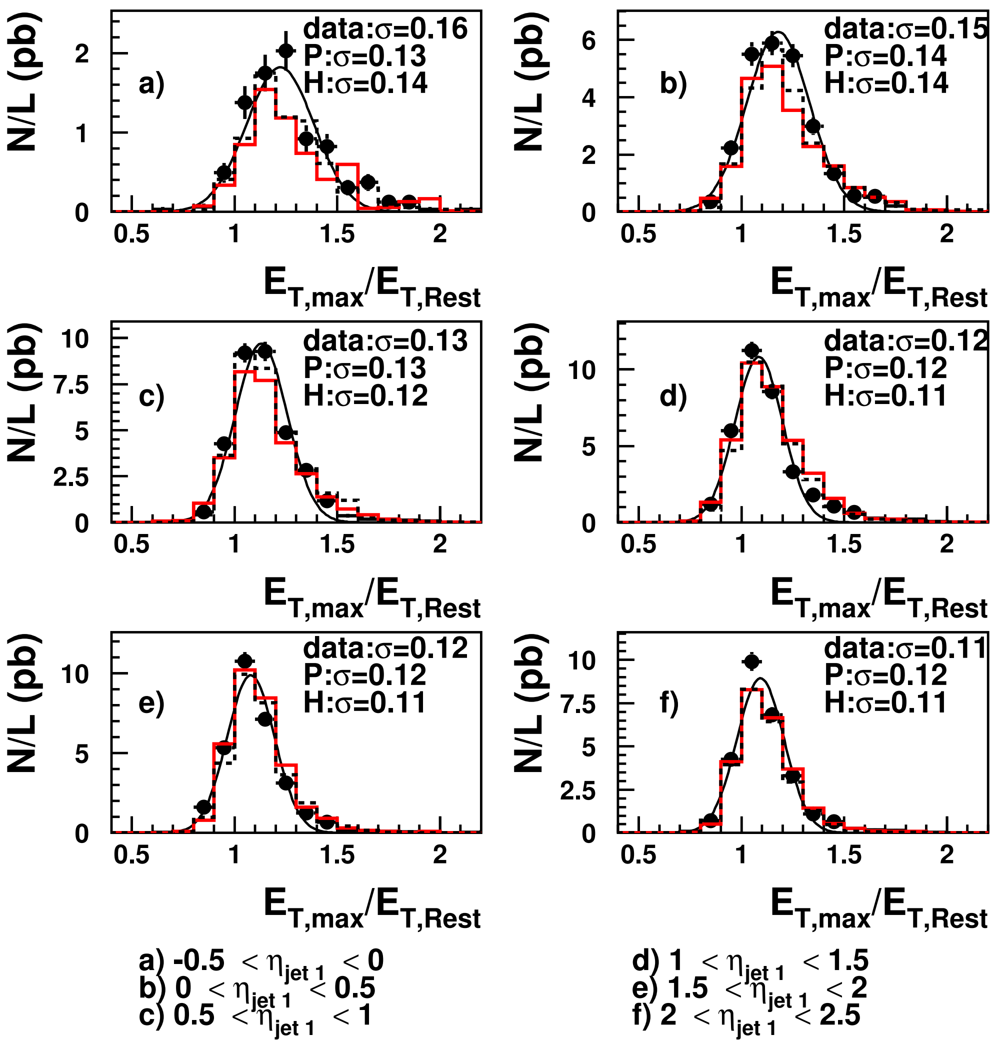

Figure D.1: E_T jet-rest balance distributions for data, PYTHIA and HERWIG for different regions in η_{jet1}. The resolution σ of the data, PYTHIA (P) and HERWIG (H) are indicated.

Bibliography

[1] S. Caron, "Three-jet production in deep-inelastic scattering and photoproduction at HERA", *Contributed to 8th International Workshop on Deep Inelastic Scattering and QCD (DIS 2000), Liverpool, England, 25-30 Apr 2000.*

[2] S. Caron, "Jets and QCD in photon-proton reactions", Contributed to HEP 2001, Budapest, PRHEP-hep2001/016

[3] H1 Collaboration, " Measurements of 2-Jet and 3-Jet Cross Sections at High Transverse Momentum in Photoproduction", converence paper presented at ICHEP 2000, Osaka

[4] C. Adloff *et al.* [H1 Collaboration], "Measurement of dijet cross sections in photoproduction at HERA", DESY-01-225, submitted to Eur.Phys.J.C, arXiv:hep-ex/0201006.

[5] S. Chekanov *et al.* [ZEUS Collaboration], DESY 01-220, arXiv:hep-ex/0112029.

[6] T. Ahmed *et al.* [H1 Collaboration], "Hard scattering in gamma p interactions", Phys. Lett. B **297** (1992) 205.

[7] C. Adloff *et al.* [H1 Collaboration], "Measurement of the inclusive di-jet cross section in photoproduction and determination of an effective parton distribution in the photon", Eur. Phys. J. C **1** (1998) 97 [arXiv:hep-ex/9709004].

[8] C. Adloff *et al.* [H1 Collaboration], "Measurement of di-jet cross-sections in photoproduction and photon structure", Phys. Lett. B **483** (2000) 36 [arXiv:hep-ex/0003011].

[9] J. Breitweg *et al.* [ZEUS Collaboration], "Dijet cross sections in photoproduction at HERA", Eur. Phys. J. C **1** (1998) 109 [arXiv:hep-ex/9710018].

[10] J. Breitweg *et al.* [ZEUS Collaboration], "Measurement of dijet photoproduction at high transverse energies at HERA", Eur. Phys. J. C **11** (1999) 35 [arXiv:hep-ex/9905046].

[11] T. Affolder *et al.* [CDF Collaboration], "Measurement of the two-jet differential cross section in proton antiproton collisions at s**(1/2) = 1800-GeV", Phys. Rev. D **64** (2001) 012001 [arXiv:hep-ex/0012013].

[12] V. M. Abazov *et al.* [D0 Collaboration], "The inclusive jet cross-section in p anti-p collisions at s**(1/2) = 1.8-TeV using the k(T) algorithm", arXiv:hep-ex/0109041.

[13] [ZEUS Collaboration], "High-mass dijet cross sections in photoproduction, Osaka paper", converence paper presented at ICHEP 2000, Osaka

[14] C. Adloff *et al.* [H1 Collaboration], "Three-jet production in deep-inelastic scattering at HERA", Phys. Lett. B **515** (2001) 17 [arXiv:hep-ex/0106078].

[15] J. Breitweg *et al.* [ZEUS Collaboration], "Measurement of three-jet distributions in photoproduction at HERA," Phys. Lett. B **443** (1998) 394 [arXiv:hep-ex/9810046].

[16] F. Abe *et al.* [CDF Collaboration], "Further Properties of High-Mass Multijet Events at the Fermilab Proton-Antiproton Collider", Phys. Rev. D **54** (1996) 4221 [arXiv:hep-ex/9605004].

[17] B. Abbott *et al.* [D0 Collaboration], "Ratios of multijet cross sections in p anti-p collisions at s**(1/2) = 1.8-TeV", Phys. Rev. Lett. **86** (2001) 1955 [arXiv:hep-ex/0009012].

[18] K. Ackerstaff *et al.* [OPAL Collaboration], "Search for an excess in the production of four-jet events from e+ e- collisions at s**(1/2) = 130-GeV to 184-GeV", Phys. Lett. B **429** (1998) 399 [arXiv:hep-ex/9802015].

[19] M. Acciarri *et al.* [L3 Collaboration], "Search for anomalous four-jet events in e+ e- annihilation at s**(1/2) = 130-GeV to 172-GeV", Phys. Lett. B **411** (1997) 330.

[20] R. Barate *et al.* [ALEPH Collaboration], "Four-jet final state production in e+ e- collisions at centre-of-mass energies ranging from 130-GeV to 184-GeV", Phys. Lett. B **420** (1998) 196.

[21] S. Chekanov *et al.* [ZEUS Collaboration], "High-mass dijet cross sections in photoproduction at HERA", arXiv:hep-ex/0112030.

[22] J. Breitweg *et al.* [ZEUS Collaboration], "W production and the search for events with an isolated high-energy lepton and missing transverse momentum at HERA", Phys. Lett. B **471** (2000) 411 [arXiv:hep-ex/9907023].

[23] C. Adloff *et al.* [H1 Collaboration], "Observation of events with an isolated high energy lepton and missing transverse momentum at HERA", Eur. Phys. J. C **5** (1998) 575 [arXiv:hep-ex/9806009].

[24] G. Frising, "Eine Likelihood-Analyse der H1 Jet-Daten", (in German), Dipl. Thesis, RWTH-Aachen (2000)

[25] H. Fritzsch and D. Holtmannspotter, "The production of single t-quarks at LEP and HERA", Phys. Lett. B **457** (1999) 186 [arXiv:hep-ph/9901411].

[26] A. Aktas, "Untersuchung von Endzuständen mit hohem Transversalimpuls in der Elektron-Proton-Streuung", Dipl. Thesis, RWTH-Aachen (2001).

[27] H1 Collaboration, "Search for Single Top Production in *ep* collisions at HERA", converence paper presented at EPS 2001.

[28] Ch. Berger, "Teilchenphysik: Von den Grundlagen zu den modernen Experimenten", (in German), *Berlin, Germany: Springer (2002)*

[29] F. Halzen and A.D. Martin, "Quarks and Leptons", John Wiley & Sons (1984).

[30] I.J.R. Atchison and A.J.G. Hey, "Gauge Theories in Particle Physics", Adam Hilger (1996).

[31] R.K. Ellis, W.J. Stirling, B.R. Webber, "QCD and Collider Physics", Cambridge University Press (1995).

[32] M.E. Peskin, D.V. Schroeder, "An Introduction to Quantum Field Theory", Perseus Books (1995).

[33] R. P. Feynman, "Photon-hadron interactions", Frontiers in physics (1972)

[34] V. N. Gribov and L. N. Lipatov, "Deep Inelastic E P Scattering In Perturbation Theory," Yad. Fiz. **15** (1972) 781 [Sov. J. Nucl. Phys. **15** (1972) 438].

[35] Y. L. Dokshitzer, "Calculation Of The Structure Functions For Deep Inelastic Scattering And E+ E- Annihilation By Perturbation Theory In Quantum Chromodynamics.", (In Russian), Sov. Phys. JETP **46** (1977) 641 [Zh. Eksp. Teor. Fiz. **73** (1977) 1216].

[36] G. Altarelli and G. Parisi, "Asymptotic Freedom In Parton Language", Nucl. Phys. B **126** (1977) 298.

[37] R. Nisius, "The photon structure from deep inelastic electron photon scattering", Phys. Rept. **332** (2000) 165 [arXiv:hep-ex/9912049].

[38] G. Abbiendi *et al.* [OPAL Collaboration], "Measurement of the hadronic photon structure function F2(gamma) at LEP2", arXiv:hep-ex/0202035.

[39] E. Witten, "Anomalous Cross-Section For Photon - Photon Scattering In Gauge Theories", Nucl. Phys. B **120** (1977) 189.

[40] J. Huston, S. Kuhlmann, H. L. Lai, F. I. Olness, J. F. Owens, D. E. Soper and W. K. Tung, "Study of the uncertainty of the gluon distribution", Phys. Rev. D **58** (1998) 114034 [arXiv:hep-ph/9801444].

[41] P. Kessler, Il Nuovo Cimento **17** (1960) 809.

[42] V. M. Budnev, I. F. Ginzburg, G. V. Meledin and V. G. Serbo, "The Two Photon Particle Production Mechanism. Physical Problems. Applications. Equivalent Photon Approximation", Phys. Rept. **15** (1974) 181.

[43] S. Frixione, M. L. Mangano, P. Nason and G. Ridolfi, "Improving the Weizsacker-Williams approximation in electron - proton collisions", Phys. Lett. B **319** (1993) 339 [arXiv:hep-ph/9310350].

[44] S. Frixione and G. Ridolfi, "Jet photoproduction at HERA", Nucl. Phys. B **507** (1997) 315 [arXiv:hep-ph/9707345].

[45] Z. Kunszt and D. E. Soper, "Calculation of jet cross-sections in hadron collisions at order alpha-s**3," Phys. Rev. D **46** (1992) 192.

[46] M. Wobisch, " Measurement and QCD Analysis of Jet Cross Sections in Deep-Inelastic Positron-Proton Collisions at sqrt(s)=300 GeV", Ph.D. Thesis, RWTH Aachen (1999), DESY-THESIS-2000-049.

[47] S. Caron, "Vergleichende Untersuchung hadronischer Endzustände in inelastischer Elektron Proton Streuung", (in German), Diploma Thesis, RWTH Aachen 1998

[48] M. H. Seymour, "Jet phenomenology," arXiv:hep-ph/9707349.

[49] M. Klasen and G. Kramer, "Inclusive two-jet production at HERA: Direct and resolved cross sections in next-to-leading order QCD", Z. Phys. C **76** (1997) 67 [arXiv:hep-ph/9611450].

[50] M. Klasen, G. Kramer and B. Pötter, "Inclusive jet production with virtual photons in next-to-leading order QCD", Eur. Phys. J. C **1** (1998) 261 [arXiv:hep-ph/9703302].

[51] B. W. Harris and J. F. Owens, "Photoproduction of jets at HERA in next-to-leading order QCD", Phys. Rev. D **56** (1997) 4007 [arXiv:hep-ph/9704324].

[52] P. Aurenche, L. Bourhis, M. Fontannaz and J. P. Guillet, "NLO Monte Carlo approach in 1 or 2 jets photoproduction", Eur. Phys. J. C **17** (2000) 413 [arXiv:hep-ph/0006011].

[53] U. Baur, J. A. Vermaseren and D. Zeppenfeld, "Electroweak vector boson production in high-energy e p collisions", Nucl. Phys. B **375** (1992) 3.

[54] S. D. Ellis and D. E. Soper, "Successive combination jet algorithm for hadron collisions", Phys. Rev. D **48** (1993) 3160 [arXiv:hep-ph/9305266].

[55] S. Catani, Y. L. Dokshitzer, M. H. Seymour and B. R. Webber, "Longitudinally invariant K(t) clustering algorithms for hadron-hadron collisions", Nucl. Phys. B **406** (1993) 187.

[56] C. Adloff *et al.* [H1 Collaboration], "Measurement and QCD analysis of jet cross sections in deep-inelastic positron proton collisions at s**(1/2) of 300-GeV", Eur. Phys. J. C **19** (2001) 289 [arXiv:hep-ex/0010054].

[57] T. Sjostrand, "High-energy physics event generation with PYTHIA 5.7 and JETSET 7.4", Comput. Phys. Commun. **82** (1994) 74.

[58] I. Abt, "Manual to IJRAY, Monte Carlo generator shell to produce eP events for H1", H1 internal note-290 (1993).

[59] G. Marchesini, B. R. Webber, G. Abbiendi, I. G. Knowles, M. H. Seymour and L. Stanco, "HERWIG: A Monte Carlo event generator for simulating hadron emission reactions with interfering gluons. Version 5.1 - April 1991", Comput. Phys. Commun. **67** (1992) 465.

[60] R. Brun, F. Bruyant, M. Maire, A. C. McPherson and P. Zanarini, "Geant3," CERN-DD/EE/84-1.

[61] M. Gluck, E. Reya and A. Vogt, "Dynamical parton distributions of the proton and small x physics", Z. Phys. C **67** (1995) 433.

[62] M. Gluck, E. Reya and A. Vogt, "Photonic parton distributions", Phys. Rev. D **46** (1992) 1973.

[63] S. Frixione, "A general approach to jet cross sections in QCD", Nucl. Phys. B **507** (1997) 295 [arXiv:hep-ph/9706545].

[64] H. L. Lai *et al.* [CTEQ Collaboration], "Global QCD analysis of parton structure of the nucleon: CTEQ5 parton distributions", Eur. Phys. J. C **12** (2000) 375 [arXiv:hep-ph/9903282].

[65] A. D. Martin, R. G. Roberts, W. J. Stirling and R. S. Thorne, "Parton distributions and the LHC: W and Z production", Eur. Phys. J. C **14** (2000) 133 [arXiv:hep-ph/9907231].

[66] M. Gluck, E. Reya and A. Vogt, "Parton structure of the photon beyond the leading order", Phys. Rev. D **45** (1992) 3986.

[67] P. Aurenche, J. P. Guillet and M. Fontannaz, "Parton distributions in the photon", Z. Phys. C **64** (1994) 621 [arXiv:hep-ph/9406382].

[68] L. E. Gordon and J. K. Storrow, "New parton distribution functions for the photon", Nucl. Phys. B **489** (1997) 405 [arXiv:hep-ph/9607370].

[69] A. Vogt, "The parton structure of real photons", arXiv:hep-ph/9709345.

[70] I. Abt *et al.* [H1 Collaboration], "The H1 Detector At Hera", Nucl. Instrum. Meth. A **386** (1997) 310.

[71] I. Abt *et al.* [H1 Collaboration], "The Tracking, calorimeter and muon detectors of the H1 experiment at HERA ," Nucl. Instrum. Meth. A **386** (1997) 348.

[72] B. Andrieu *et al.* [H1 Calorimeter Group Collaboration], "The H1 liquid argon calorimeter system", Nucl. Instrum. Meth. A **336** (1993) 460.

[73] R. D. Appuhn *et al.* [H1 SPACAL Group Collaboration], "The H1 lead/scintillating-fibre calorimeter", Nucl. Instrum. Meth. A **386** (1997) 397.

[74] C. Adloff *et al.* [H1 Collaboration], "Diffraction dissociation in photoproduction at HERA", Z. Phys. C **74** (1997) 221 [arXiv:hep-ex/9702003].

[75] T. Carli et al., "Performance of the H1 Lar Trigger in 1994", H1 internal note-445 (1995).

[76] The method is described in:
http://www-h1.desy.de/iwork/iescale/hfs/hfs.html .

[77] The algorithm is described in:
http://www-h1.desy.de/iwork/iescale/qescat/qescat.html .

[78] P. Bruel, Ph.D. thesis, Orsay (1998).

[79] A. Blondel and F. Jacquet, Proceedings of the Study of an *ep* Facility for Europe ed. U. Amaldi, DESY 79/48 (1979) 391.

[80] QBGFMAR: "An updated PHAN package for cosmic and halo muon topological rejection in high p_T physics analysis", H1 internal note-556 (1998).

[81] W. T. Giele, E. W. Glover and D. A. Kosower, "Jet investigations using the radial moment", Phys. Rev. D **57** (1998) 1878 [arXiv:hep-ph/9706210].

[82] T. R. Merz, "Messung der Proton-Strukturfunktion F2 bei hohen Impulsueber-traegen mit dem H1-Detektor", Ph.D. thesis, Univ. Hamburg (1994).

[83] L. Lonnblad, "ARIADNE version 4: A Program for simulation of QCD cascades implementing the color dipole model," Comput. Phys. Commun. **71** (1992) 15.

[84] K. Charchula, G. A. Schuler and H. Spiesberger, "Combined QED and QCD radiative effects in deep inelastic lepton - proton scattering: The Monte Carlo generator DJANGO6", Comput. Phys. Commun. **81** (1994) 381.

[85] P. Bate , "High Transverse Momentum 2-Jet and 3-Jet Cross Section Measure-ments in Photoproduction", Ph.D. thesis, Univ. of Manchester (1999).

[86] B. Heinemann, " Measurement of Charged Current and Neutral Current Cross Sections in Positron-Proton Collisions at sqrt(s)=300 GeV", Ph.D. thesis, Univ. HH (1999).

[87] J. Scheins, "Suche nach Kontakt-Wechselwirkungen und Gravitoneffekten in der tief-inelastischen Streuung bei HERA", Ph.D. thesis, RWTH Aachen (2001).

[88] C. Adloff *et al.* [H1 Collaboration], "Measurement of neutral and charged current cross-sections in positron proton collisions at large momentum transfer", Eur. Phys. J. C **13** (2000) 609 [arXiv:hep-ex/9908059].

[89] T. Ahmed *et al.* [H1 Collaboration], "Inclusive parton cross-sections in photoproduction and photon structure", Nucl. Phys. B **445** (1995) 195 [arXiv:hep-ex/9504004].

[90] S. Aid *et al.* [H1 Collaboration], "Jets and Energy Flow in Photon-Proton Collisions at HERA", Z. Phys. C **70** (1996) 17 [arXiv:hep-ex/9511012].

[91] M. Erdmann, "The partonic structure of the photon: Photoproduction at the lepton proton collider HERA", DESY-96-090.

[92] J. Breitweg *et al.* [ZEUS Collaboration], "Measurement of jet shapes in photoproduction at HERA," Eur. Phys. J. C **2** (1998) 61 [arXiv:hep-ex/9710002].

[93] F. Abe *et al.* [CDF Collaboration], "Measurement of double parton scattering in anti-p p collisions at s**(1/2) = 1.8-TeV," Phys. Rev. Lett. **79** (1997) 584.

[94] V. Blobel, E. Lohrmann, "Statische und numerische Methoden der Datenanalyse" Teubner (1998).

[95] V. B. Anikeev, A. A. Spiridonov and V. P. Zhigunov, "Correcting factors method as one of unfolding technique", Nucl. Instrum. Meth. A **322** (1992) 280.

[96] G. Zech, "Comparing statistical data to Monte Carlo simulation: Parameter fitting and unfolding", DESY-95-113.

Acknowledgment

I would like to thank my supervisor Prof. Dr. Christoph Berger for his support, advice and interest. I am thankful to Prof. Dr. Günter Flügge for accepting to be my second referee, Gilles Frising, Boris Leissner, Hans-Ulrich Martyn and Jürgen Scheins for helpful discussion during my time in Hamburg and proofreading. I am grateful to all my colleagues and former colleagues from the DESY-Aachen group, Adil Aktas, Anja Vest, Carsten Schmitz, Carlo Duprel, Klaus Rabbertz, Linus Lindfeld, Markus Wobisch, Markus Stoye, Martin Wessel, Peer-Oliver Meyer and Thomas Hadig. For running H1 and all their help I thank all my colleagues from the H1 experiment. Sorry that I can't write all the names. I wish to thank Stephano Frixione and Björn Pötter for many helpful discussions on theoretical questions and for making their NLO code public available. I owe thanks to Simone Göde for all her support and for a beautiful time. Finally I have to thank my parents, this work would not be possible without their support during 28 years.